Working Session

Innovative Design and Structural Materials

Papers and Posters

Leere Seite

Blank page

Page vide

Seismic Responses of Variable Stiffness Semi-Active Control System

Xinghua YAN
Prof.
Beijing Inst. of Civil Eng. and Arch.
Beijing, China

Yan Xinghua, born 1945, received his engineering degree from Qinghua Univ. in 1968 and MA in 1981. He is currently professor of structural eng. at Beijing Inst. of Civil Eng. and Arch.

Summary

This paper presents one type of new structural system with the variable stiffness semi-active control.The system for reducing earthquake response is composed of the control devices and the energy dissipation devices jointed to diagonal braces.According to the feedback structural information, the control devices open or close the energy dissipation devices.When the energy dissipation devices are closed,the braces work as the structural members have certain stiffness and absorb the seismic energy; When the energy dissipation devices are opened,the braces stiffness becomes zero and the absorbed seismic energy is dropped.Usually the semi-active control system uses the structural displacement as control information.The basic theory,the mathematical model,the seismic analysis of the structures,one example of the frame-shear wall structure and some conclusions are given in this paper.

1. Introduction

In the basic equation of motion of strucrures,the mass,damper and stiffness are three basic influence parameters for structural seismic responses.If any one is changed,the structural responses will be changed.Various structural control approaches including passive control,active control,seimi-active control and hybrid control can modify these dynamic parameters in a desirable manner ,all kinds of control devices have been successfully applied in many engineering structures to reduce earthquake responses.

Variable stiffness control is able to switch dynamically the stiffness of some components in a structure from a certain constant to zero,thereby modify the natural period of the structure to avoid the main seismic period,moreover,the controlled variable stiffness components can generate the hysteresis loops under earthquake,thus,a lot of seismic energy is dissipated and the seismic responses of controlled structure is reduced greatly.Semi-active control devices that typically have extremely low power requirements can achieve the variable stiffness control.

In this paper ,a new type of variable stiffness semi-active control technique is presented.The system of seismic response reduction is composed of control devices and energy dissipation devices. According to the feedback information of structural displacement the control devices switch off or switch on the control valve of the energy dissipation devices jointed to diagonal braces and main structure.When the structure reaches the maximum displacement position and begins moving to the oppose direction , the energy dissipation devices are opened by the control devices and the stiffness of braces becomes zero.The absorbed seismic energy by the braces is dropped into the energy dissipation devices , otherwise the energy dissipation devices are closed, and the braces as structural components provide the certain stiffness and absorb the seismic energy.Because the structure goes through return point two time in one period,thus,the structure is able to modify vibration property and drops seismic energy two times in every period.

2.The basic theory and mathematical model

The schematic of energy dissipation system is shown in Fig.1. The variable stiffness semi-active control system of reducing seismic response is fitted on the structural interstory as shown in Fig.2.
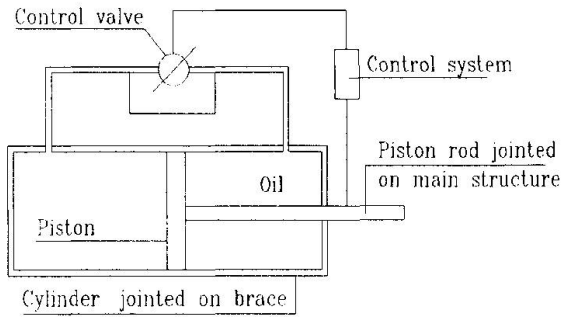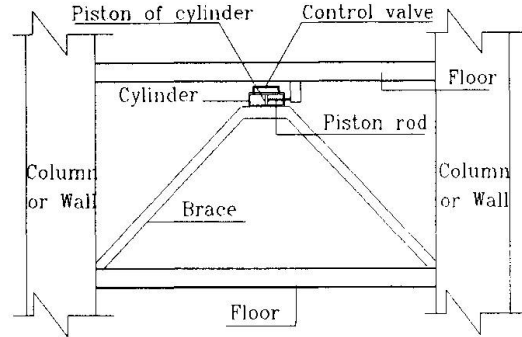
Fig.1.Schematic of energy
    dissipation system

Fig.2.Scheme of structural system with
    variable stiffness semi-active control

The energy dissipation system is composed of the cylinder and the relative oil -way with the control valve that is controlled by the control system to close or open.The cylinder body is rigidly connected to the upper end of the braces which bottom is jointed on the floor,the piston rod of the cylinder is rigidly connected to the upper floor.When the control valve is closed,there is not the relative movement between the piston and the cylinder body.The braces go through same interstory displacement as the main structure,and provide certain lateral stiffness and restoring force absorb the seismic energy. When the control valve is opened, the relative movement between the piston and the cylinder body will be generated and the braces whose structural lateral stiffness becomes zero return to the original position.The seismic energy absorbed by the braces is dropped by the cylinder.

The control system is composed of a computer and relative information transmitters.Based on the information of the structural incremental displacement or velocity,the control devices can discern the structural point of return at which the sign of velocity or incremental displacement is changed,and open the control valve if the floor is at the point of return or close the control valve if the floor is not at the point of return.

The restoring force model of controlled braces is shown in Fig.3.The points A and C are the point of return,the lines OA and BC are the process of energy absorption of the braces in which the braces remain original lateral stiffness being equal to the rate of line,the lines AB and CD are the state of energy dissipation of the braces at which the lateral stiffness of the braces is changed to zero.

As stated above,the restoring force of the controlled braces is:

$$\begin{cases} \Delta x_i \cdot \Delta x_{i+1} < 0, & F = 0 \\ \Delta x_i \cdot \Delta x_{i+1} \geq 0, & F = K_d(x_i - x_0) \end{cases} \tag{1}$$

where, Δx_i, Δx_{i+1} are respectively the incremental displacement relative to the ground at the i th and $(i+1)$th time moment, x_i, x_0 are respectively the relative displacement at the i th time moment and at the previous time moment at which the structure is at the point of return, k_d is the original lateral stiffness of braces, F is the restoring force of controlled braces.
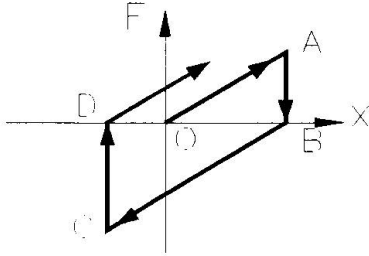
Fig.3.Restoring force model
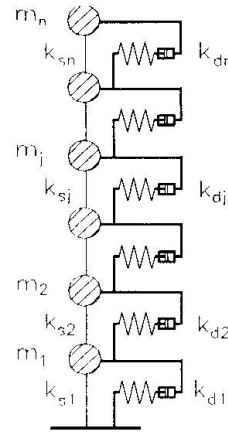of controlled brace

Fig.4.Calculation schematic
of the controlled structure

3.Structural seismic analysis

The Calculation schematic used for seismic analysis of a multiple-story structure system with the variable stiffness semi-active control is shown in Fig.4. The springs with the energy dissipation device connected on interstory are the modelling of controllable reducing response system and can cooperate with the main structure under earthquake.

The basic equation of motion of the controlled structural system is:

$$\begin{cases} [M]\{X''\}+[C]\{X'\}+[K_s]\{X\}+\{F_d\}=-[M]\{I\}x_g'' \\ \{F_d\}=[K_d]\{X\} \end{cases} \tag{2}$$

In which,$[M]$ is the mass matrix, $[C]$ is the damper matrix and $[C]=\alpha[M]+\beta[K],[K_s]$ is the lateral stiffness matrix of the main structure,$[K_d]$ and $\{F_d\}$ are respectively the lateral stiffness matrix and the generated force vector of the reducing response devices,$\{X\},\{X'\},\{X''\}$ is respectively the relative displacement vector, the relative velocity vector,the relative acceleration vector,x_g'' is the acceleration of the earthquake ground motion.

It is convenient for finding solution by using numerical analysis method to change Eq.(2) into the half incremental equation,as follows:

$$\begin{cases} [M]\{X''\}_i+[C]\{X'\}_i+[K_s]\{\Delta X\}_i+\{F_s\}_{i-1}+\{F_d\}_i=-[M]\{I\}x_{g,i}'' \\ \{F_d\}_i=\{F_d\}_{i-1}+[K_d]_i\{\Delta X\}_i \end{cases} \tag{3}$$

where i and (i -1) are the number of the time moment (Δt).The structural seismic responses at i time moment can be found by Eq.(3).Taking these responses as the initial data,the solution at next moment is able to obtain.

The control condition shown in Eq.(4) that must be checked at every moment,relevantly,the

stiffness matrixes,the story shear vectors and the restoring force vectors must be modified by the control condition.

$$\begin{cases} \Delta x_{i,j} \cdot \Delta x_{i+1,j} < 0, V_{i,d,j} = 0 \\ \Delta x_{i,j} \cdot \Delta x_{i+1,j} \geq 0, V_{i,d,j} = V_{i-1,d,j} + k_{d,j} \cdot \Delta x_{i,j} \end{cases} \tag{4}$$

where $\Delta x_{i,j}$, $\Delta x_{i+1,j}$ are incremental j th floor displacement relative to the ground at the i th and $(i+1)$th time moment respectively, $V_{i,d,j}$, $V_{i-1,d,j}$ are the shears of the reducing response devices at the i th and $(i-1)$th time moment in j th story respectively, $k_{d,j}$ is the j th story lateral stiffness of the reducing response devices.

4. Numerical Example

Taking a 16 story R.C. frame-shear wall structure with the variable stiffness semi-active control system for the numerical example,the structural plane and elevation are shown in Fig.5.,the main structural characteristic parameters are shown in table 1.

Fig.5.Structural plane and elevation
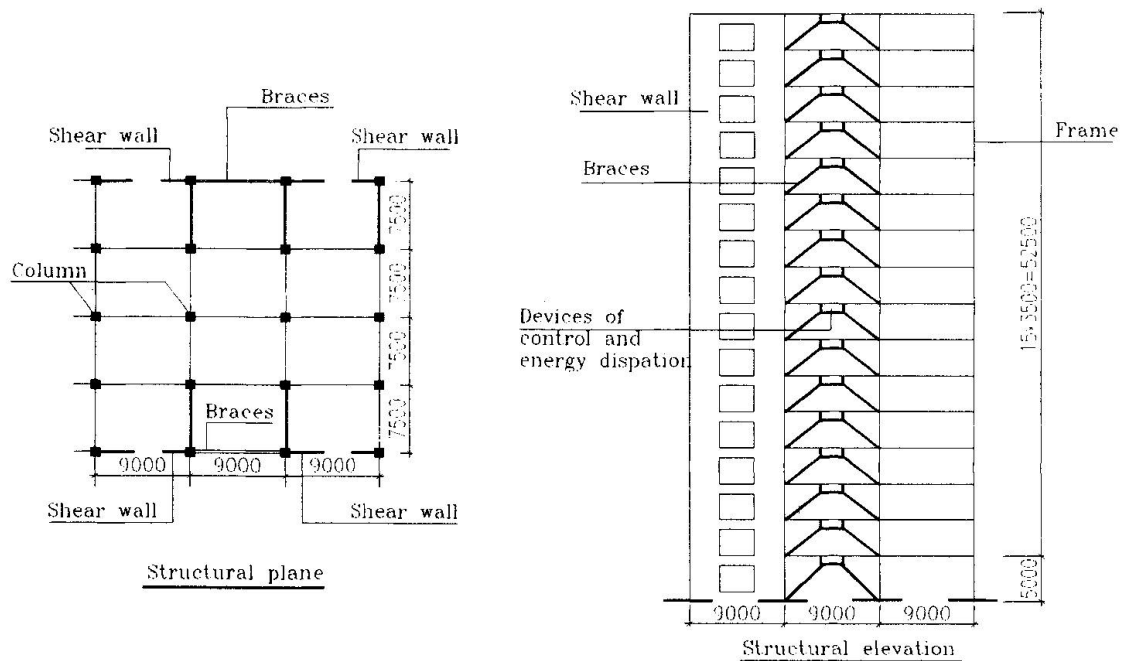
Table 1. main structural characteristic parameters

Floor No.	Column section(cm)	Wall thickness(cm)	Mass (t.sec.^{2}/m)	Elastic module of concrete(t/m^2)	Story height (m)
1	90×90	25	93.3	3250000	5
2-8	90×90	25	93.3	3250000	3.5
9-15	80×80	18	93.3	3250000	3.5
16	80×80	18	77.8	3250000	3.5

The horizontal seismic analysis is made in the transverse direction.The EL centro(in 1940,N-S) earthquake is used for the seismic ground motion whose peak acceleration is adjusted to 200gal and the time moment is 0.02sec..The lateral story stiffness of the controlled braces is r times the lateral story stiffness of the frames in main structure, r is called the rate of stiffness written as follows:

$$r = \frac{k_{d,j}}{k_{f,j}} \tag{5}$$

where, $k_{d,j}$ and $k_{f,j}$ are respectively the lateral stiffness of the braces and the frames, j is number of floors.The structure is considered to be linear-elastic in the analysis.

Based on the analysis results,the maximum interstory displacements and maximum story shears of the structure are respectively shown in Fig.6. and Fig.7. Four curves given in above Figs. indicate respectively the structural response results in no control (r=1) and control(r=0.5,1.0,1.5) state.
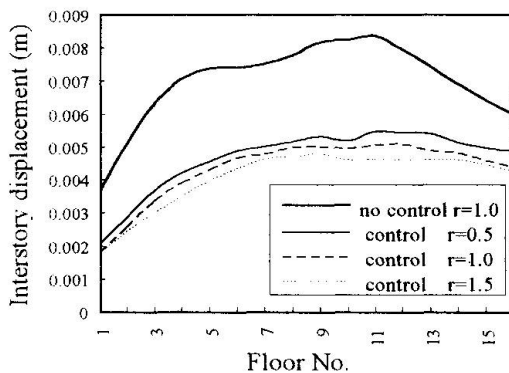
Fig.6.Maximum interstory displacement comparison
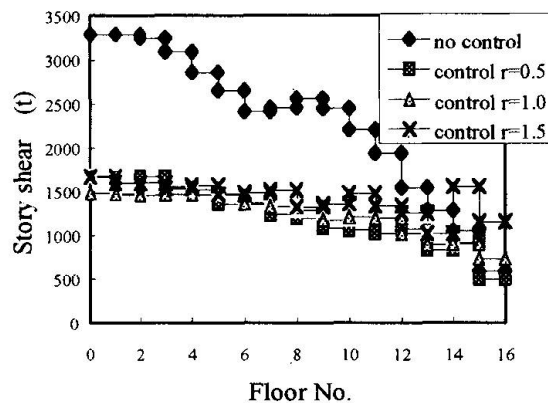
Fig.7.Maximum story shear comparison

From the Figs.,the efficiency of reducing seismic responses by means of the variable stiffness semi-active control system is obvious and is different with the different rate of stiffness(r),as a general rule,the reduction of response increases with increment of rate of stiffness.The maximum interstory displacement is reduced by 51% of the uncontrolled response,the maximum story shear is reduced by 60%. The maximum interstory displacement angle is about 1/700 and indicates that the controlled structure remains the elastic state.

To study effect of reducing response of such cases that the controlled braces are fitted on some stories and other stories have no braces,the main structure remains unchanged,but the braces (r=1.0) are only fitted on 1-3 story in case 1 and on 1,9,16 story in case 2.The seismic analysis is made for two cases,the analysis results about the maximum interstory displacements and maximum story shears are respectively shown in Fig.8 and Fig.9 in which the results of every story control (1-16) are given for comparison.

From Fig.8 and Fig.9, the difference of three cases is not big,particaly the difference of story shears is small,so the notional design including notional select of brace stiffness and notional select of stories in which the braces are fitted can get the better economical effect.
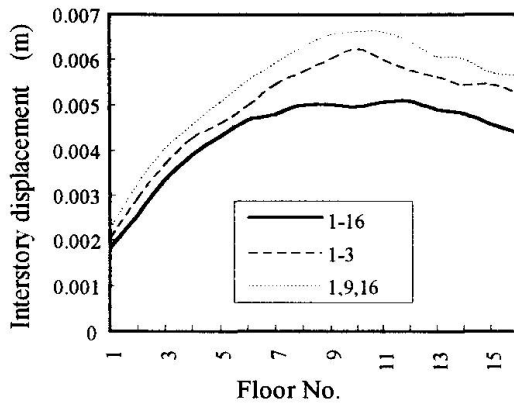
Fig.8.Maximum interstory displacement
comparison
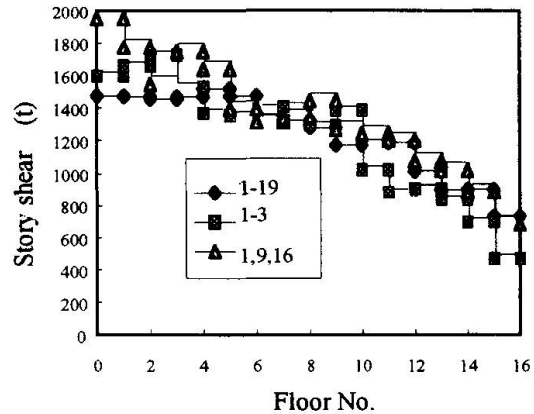
Fig.9.Maximum story shear
comparison

5.Conclusions

1.The variable stiffness semi-active control system is effective to reduce seismic response of controlled structures ,the controlled structures can remain elastic state under strong earthquake.

2.The lateral stiffness of the controlled braces has obvious influence on the effect of reducing seismic response,it is necessary in design to select notional rate of stiffness.

3. The effect of reducing response of such case that the controlled braces are fitted on some stories and other stories have no braces is satisfactory.

4.The restoring force model of controlled braces and the analysis procedure of controlled structure can be used for the seismic analysis of this kind of structures.

References

1.Kawashima,K. and S.Unjoh ： Variable Dampers and Variable Stiffness for Seismic Control of Bridges, Proc.of International Workshop on Structural Control,1993.

2.G.C.Lee, Z.Liang, and M.Tong ： Innervated Structures, NCEER Technical report ,1994.

3.Yan Xinghua:Study on the structural system with controllable energy dissipation devices,Proc. of third national symposium on structural control(in Chinese),1995.

4.Yan Xinghua:Basic theory of controllable energy dissipation and structural analysis for reducing earthquake response,Earthguake engineering and engineering vibration(in Chinese),1997.

Investigation on the Statical Characteristics
of Beam-to-Column Connections

Atsuo TANAKA
Prof.
Utsunomiya Univ.
Utsunomiya, Japan
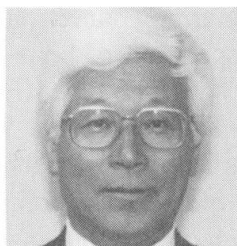
Atsu Tanaka, born 1937, received his engineering degree form Tokyo Univ. in 1967. He is currently professor of Faculty of Engineering at Utsunomiya Univ.

Hiroshi MASUDA
Research Assist.
Utsunomiya Univ.
Utsunomiya, Japan

Hiroshi Masuda, born 1963. He is currently research assistant of faculty of Engineering at Utsunomiya Univ..

Summary

The statical characteristics of WBFW (web bolted and flange welded) type beam-to-column connections were experimentally investigated. The specimens with H-shaped columns or RHS columns were tested. The main test parameters are the disposition of bolts at the bolted web connection and the section of column members. From this test, the basic statical characteristics, such as ultimate bending strength eMu, plastic deformation ability, failure mode, are obtained. The results are summarized that α value (=eMu$/$Mp Mp:full plastic moment of the connected beam) and deformability of specimens are influenced by the bending strength of bolted web connection and by wide-to-thickness ratio of column flange.

1. Introduction

In Japan beam-to-column connections of small or medium size steel building frames are fabricated at shop by welding. On the other hand WBFW type beam-to-column connections, which are executed at the building site, are commonly used at high rise building frames. Up to now, at the design of beam connections it is customly assumed that the flange connected parts carry the whole bending moment and the web connected part carries the whole shear force. But the depth of beams are getting large, web connected parts should be carry some bending moment in addition to shear force. But the stress transfer capability of the bolted web connections is not so large because such bolted connections are commonly single shear connections. In addition the section of columns are usually square hollow section, and in such case the bending stress transfer at the web connection is considerably restricted. From such view points a series of experimental study on the WBFW type beam-to-column connections were executed in order to investigate the effect of the bending strength of the bolted web connection on the overall performance of the beam-to-column connection.

2. Test Specimens and Test Setup

The objective of this test was mainly the investigation of the influence of the bending strength of the bolted web connections to the maximum bending strength and the deformation capacity of the whole beam-to-column connections. The main experimental parameters are cross sections of column and disposition of bolts at the web connected part. The specimens using H-shaped columns were cantilever type (H series). Horizontal cyclic loads were applied to the tip of the beam. The specimens using RHS columns were T-Shaped type (B series). The test setup of this test series is shown schematically in Fig.1. Horizontal cyclic loads were applied to the top of the RHS column. Those specimens were cyclically loaded under displacement $\pm 2c\delta p$, $\pm 4c\delta p$, $\pm 6c\delta p$ and $\pm 8c\delta p$, where $c\delta p$ is the calculated elastic displacement corresponding to the plastic moment at the end of the beam. A total of fifteen nearly 1/2 scale model specimens with different type of column, different cross-sections of beam, and different bolt disposition at the bolted web connection were prepared, as summarized in Table 1. The character p, g, e, n and m in Table.1 are corresponding to the length and so on shown in Fig.2. Bolts were F10T class high strength bolts and they were tightened by nut lotation method. The connection details of B series specimens are illustrated in Fig.3.
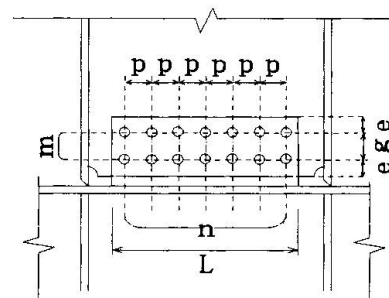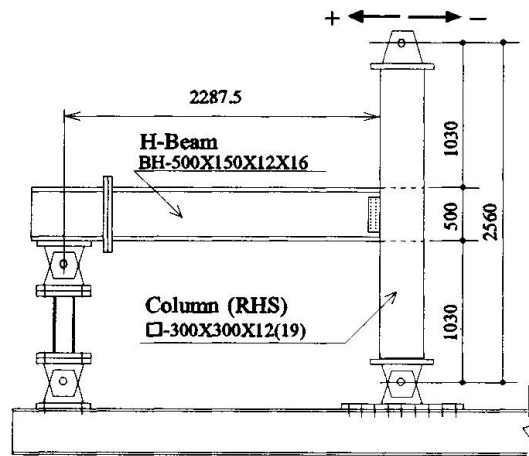
Fig.1 Test Setup (RHS Column)

Fig.2 bolted web connection details

Table 1 Test Specimens

Specimen	Column	Beam	Gasette Plate tg (mm)	Gasette Plate L (mm)	H.T.B (F10T)	p (mm)	g (mm)	e (mm)	n	m
H-1-1	BH-400×350×16×16	BH-500×150×12×16	19	375	M12	35	35	30	10	1
H-1-2	BH-400×350×16×16	BH-500×150×12×16	19	375	M12	35	35	30	10	2
H-1-3	BH-400×350×16×16	BH-500×150×12×16	19	375	M12	35	35	30	10	3
H-2-1	BH-400×350×16×16	BH-500×100×16×16	22	380	M16	50	50	40	7	1
H-2-2	BH-400×350×16×16	BH-500×100×16×16	22	380	M16	50	50	40	7	2
H-2-3	BH-400×350×16×16	BH-500×100×16×16	22	380	M16	50	50	40	7	3
H-3-1	BH-400×350×16×16	BH-500×100×12×12	19	360	M20	50	50	30	7	1
H-3-2	BH-400×350×16×16	BH-500×100×12×12	19	360	M20	50	50	30	7	2
B12-1-1	□-300×300×12	BH-500×150×12×16	19	375	M12	35	35	30	10	1
B12-1-2	□-300×300×12	BH-500×150×12×16	19	375	M12	35	35	30	10	2
B19-1-1	□-300×300×19	BH-500×150×12×16	19	375	M12	35	35	30	10	1
B19-1-2	□-300×300×19	BH-500×150×12×16	19	375	M12	35	35	30	10	2
B19-1-S1	□-300×300×19	BH-500×150×12×16	19	375	M12	35	35	30	10×1+4×1	
B19-1-S2	□-300×300×19	BH-500×150×12×16	19	375	M12	35	35	30	4	2
B19-1-0	□-300×300×19	BH-500×150×12×16	19	375	M12	35	35	30	—	—

B12-1-1, B19-1-1

B12-1-2, B19-1-2

B19-1-S1

B19-1-S2

B19-1-0
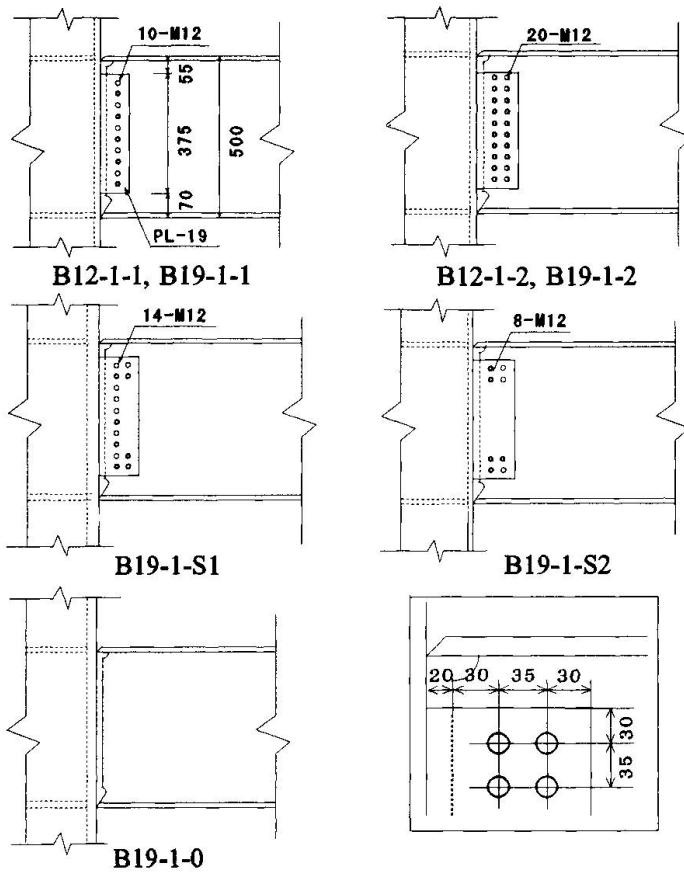
Fig.3 Connection Details (B series)
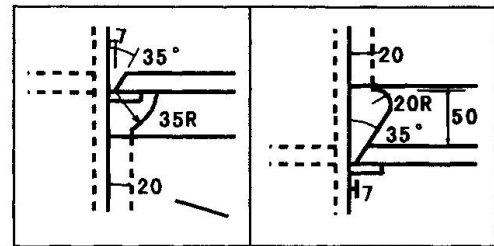
Fig.4 Weld Access Hole Details

Table 2 Mechanical Properties

Specimen		σy (t/cm²)	σu (t/cm²)	EL (%)
H series	PL-12	2.97	4.38	22
	PL-16	2.67	4.21	22
	PL-19	2.61	4.18	30
	PL-22	2.56	4.14	34
B series	PL-12	2.87	4.25	33
	PL-16	2.82	4.17	31
	CO-12	4.05	4.75	21
	CO-19	4.50	5.10	19

σy : Yeild Strength σu : Tensile Strength
EL : Elongation

Table 3 Test Results

Specimen	eMu (tcm)	Mp (tcm)	α	Failure mode	η	ηs
H-1-1	7121	5063	1.41	F.M.1	27.4	15.2
H-1-2	7426	5063	1.47	F.M.1	32.6	17.1
H-1-3	7661	5063	1.51	F.M.1	49.3	28.8
H-2-1	5217	4384	1.19	F.M.2	8.0	5.3
H-2-2	5664	4384	1.29	F.M.2	11.9	7.6
H-2-3	6181	4384	1.41	F.M.2	13.0	8.1
H-3-1	4230	3809	1.11	F.M.2	12.9	6.7
H-3-2	4606	3809	1.21	F.M.2	14.9	7.7
B12-1-1	6485	5162	1.26	F.M.1	12.6	7.1
B12-1-2	6673	5162	1.31	F.M.1	13.5	8.2
B19-1-1	6701	5162	1.30	F.M.1	15.3	8.8
B19-1-2	6989	5162	1.35	F.M.1	18.3	10.4
B19-1-0	6269	5162	1.21	F.M.2	5.8	3.2
B19-1-S1	7110	5162	1.38	F.M.3	20.1	10.4
B19-1-S2	6365	5162	1.23	F.M.3	12.8	6.8

eMu : maximum bending strength
Mp : plastic bending moment (caliculated value)
α : maximum strength ratio of bending strength (= eMu/Mp)
η : cumulative inelastic deformation ratio (based on M - θ curve)
ηs : cumulative inelastic deformation ratio (based on skeleton M - θ curve)

As for specimen B19-1-0, only the flanges were connected without web connection. Complete penetration groove welds were used to connect the beam flanges to the column flanges in all specimens. The detail of the weld access hole are shown in Fig.4. The material of all beams and H-shaped column were SS400 steel and material of all RHS columns were STKR 400 steel. The mechnical properties of the material of the members used in the specimens are summarized in Table 2.

3. Experimental Results

Each specimen was subjected to cyclically increasing displacements. Cyclic loading was continued until failure occurred at the connection. When all specimens reached the inelastic range, small cracks occurred at the flange of the beam near the weld access hole. At the ultimate stage the fracture of the beam flange, which started from the center of the flange, occurred and developed to overall the flange. Ultimately the local buckling was also observed at the compression side beam flange. The overall fracture of the beam flange at the specimens using the beam with usual cross-section, H-1-1, H-1-2, H-1-3, B12-1-1, B12-1-2, B19-1-1, B19-1-2, B19-1-S1 and B19-1-S2, occurred after sufficient plastic deformation (F.M.1). At the specime B19-1-S1 and B19-1-S2 web connecting bolts broke off simultaneously. At the H-2 type and H-3 type specimens brittle fracture occurred at the overall flange (F.M.2).

In Table 3 the maximum bending strength at the end of the beam eMu, which corresponds to the horizontal maximum load, the plastic bending moment Mp, maximum strength ratio α = eMu/Mp, failure mode, cumulative inelastic deformation ratio η which were computed from the normalized beam end moment (M/Mp) versus the normalized beam end lotation (θ/cθp) curves, cumulative inelastic deformation ratio ηs from the skeleton curves of M/Mp-θ/cθp relationships are summarized. The plastic lotation at the beam end cθp were calculated based on plastic displacement cδp. The skeleton curves of M/Mp-θ/cθp relationship are shown in Fig.6.

Fig.7 shows the maximum strength ratio α versus the number of web bolt lines m relationship of the specimens using beams with same cross section. As for the specimen without web connction, B19-1-0, the α value was plotted at the number of bolt line m=0.
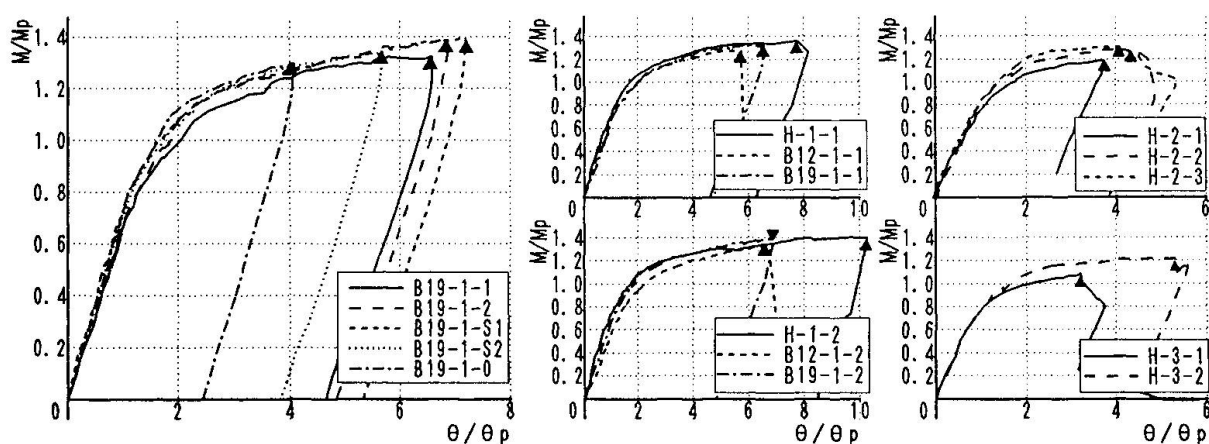

Fig.6 M/Mp - θ/θp

The maximum bending strength of the beam end connection increases with increasing of bolt line at the web connected part. The maximum strength ratio α versus the width-to-thickness ratio of the column flange D/t relationships are shown in Fig.8, where D and t are the width and the thickness of the column. As for the specimens using H-shaped columns the maximum strength ratio were plotted against D/t=0. It is observed that the maximum bending strength decreases with increasing of D/t.

The maximun strength ratio α versus the cumulative inelastic deformation ratio ηs relationship about H series specimens are shown in Fig.9. As above mentioned, the fracture of beam flanges of the H-2 and H-3 type specimens occurred in brittle manner, because the cross-section of the beam of those specimens were so special that the section module of the flange is extremely small in comparison with usual beam section. Therefore the value of ηs are very small, nevertheless number of bolt line at the web connected part increases. When the beams with usual cross-section such as that of the H-1 type specimen are used, ηs values are larger than 15 and it increases with increasing of bolt line. Fig.10 shows the α - η s relationship of B series specimens. It is clear that η s values of B series specimens were considerably small in comparison with those of H series specimens. The main reason of this fact is considered to be the difference of the cross section shape of the column. When the columns are RHS, web connected parts of the beam end connections do not work effectively to transfer the bending stress from web of the beam to column, because the out of plane stiffness of the web connected parts of the columns is very small. The tendency of this phenomenon appears more clearly, when D/t of the RHS column becomes large. From Fig.10 it becomes clear that the plastic deformation ability of the connected beams increases with incresing of the maximum bending strength of the beam end connections and that the maximum bending strength of the beam end connections increases with increasing of the maximum bending strength of the web connected parts. The bolts located near the flange work better than those located center of the web. But it is necessary to connect center part of the web at least one line to get better performance of the beam end connection.
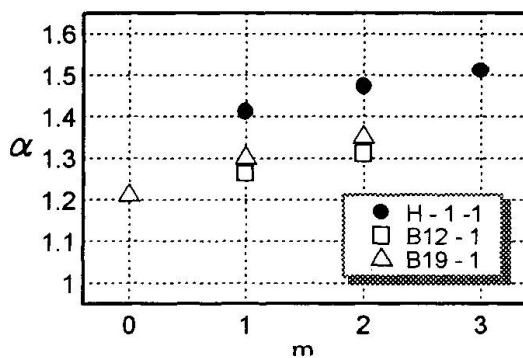
Fig.7 α - m Relationships
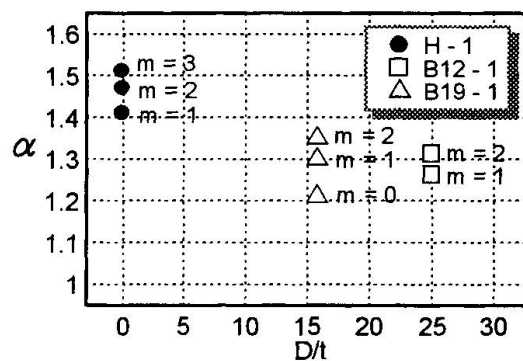
Fig.8 α - D/t Relationships
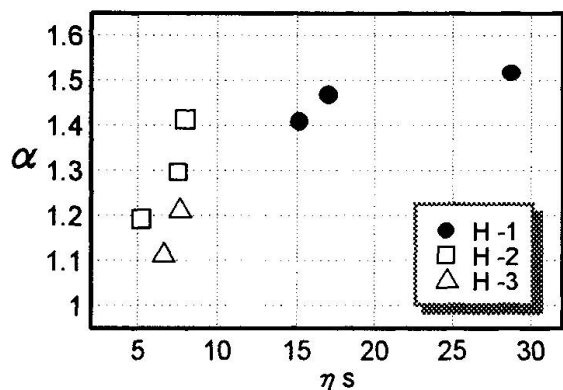
Fig.9 α - ηs *Relationships*
(H - series)
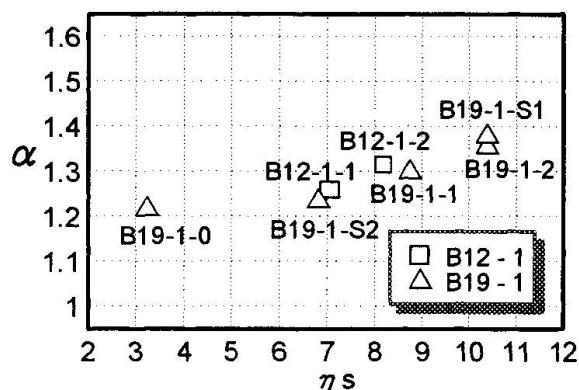
Fig.10 α - ηs *Relationships*
(B - series)

4. Conclusion

In order to investigate the statical characteristics of WBFW type beam-to-column connections, experimental study was carrid out. Main items obtained from this study are summarized as follows.

1) The shape of the section of column member has large influence upon the statical characteristics of the beam end connections. In case column members are RHS, the maximum bending strength of the beam end connections are smaller than the case of using H-shaped column.

2) The plastic deformation ability increases with increasing of the maximum bending strength of the beam end connections.

3) The maximun bending strength of the beam end connections increases with increasing of the bending strength of the bolted web connection.

4) At the bolted web connection the bolts located near the flange work better than those located center part of the web. But it is necessary to connect center part of the web.

5. References

Atsuo TANAKA, Ben KATO et al. : Seismic damage of steel beam-to-column connections -Evaluation from statical aspect- Proceeding of STESSA'97, pp 856-865.
Atsuo TANAKA, Hiroshi MASUDA et al. : Experimental study on the static characterristics of the WBFW type beam-to-column connections (In Japanese) Trans. of AIJ No.484, pp121-130. 1996 June

Ductile Performance of RC Columns in High-Rise Buildings

Yuping SUN
Assist. Prof.
Kyushu Univ.
Fukuoka, Japan

Yuping Sun, born 1961, received his
Ph.D. from Kyushuj Univ. in 1992. His
research interests include earthquake-
resistant design of reinforced concrete
structures, confinement of high-strength
concrete and nonlinear analysis of concrete
members.

Kenji SAKINO
Prof
Kyushu Univ.
Fukuoka, Japan

Kenji Sakino, born 1946, received his Ph.D.
from Kyushu Univ. in 1982. His research
interests include earthquake resistance of
reinforced concrete columns and shear walls,
confinement of high-strength concrete, and
inelastic behaviour of concrete-filled steel
tubular columns.

Summary

Confinement of concrete by transverse hoop or steel tube is effective in enhancing the ductility of
reinforced concrete columns, especially columns under high axial load. Six specimens were
tested under repeated lateral force to investigate seismic behavior of the confined columns. Test
results of these specimens verified effectiveness of confinement by steel tube or high-strength hoop
with rational configuration. The confined R/C columns exhibited very ductile performance even
under axial compression force so high as the axial load ratio was 0.67.

1. Introduction

In Japan design standard for reinforced concrete structures, the upper limit of axial load ratio is
recommended as 0.33 for column to ensure ductile seismic performance. However, columns at
the lower stories of high-rise buildings usually have to sustain higher compression force when hit
by a strong earthquake. It has been widely known that earthquake-resistant performance of the
reinforced concrete columns under high axial load is very poor. Therefore, to promote the use of
reinforced concrete structures in high-rise buildings located on seismic areas, a practical method is
desirable to make the columns subjected to high axial load more ductile.

Confining reinforced concrete column by transverse reinforcements is one of the effective methods
to enhance the earthquake-resistant capacity. This paper proposes two confining methods for
square concrete columns under high axial load. The proposed methods are: 1) use of steel tube in
lieu of conventional hoop or spiral, and 2) use of high-strength hoop, to confine columns. Using
steel tube or high-strength hoop as confining material was for applying stronger lateral restraint to
larger expansion of concrete in the column subjected to high axial force. Six specimens were
tested under earthquake-simulated loading to investigate effectiveness of the proposed methods.
This paper describes the experimental results of these tests.

2. Outlines of experiment

Six 250x250x1000 mm prismatic columns were fabricated. Longitudinal bars in each specimen
consisted of twelve 13 mm diameter (D13) deformed bars uniformly distributed along the core
perimeter. Among six specimens, four columns were confined by square steel tube, and the other
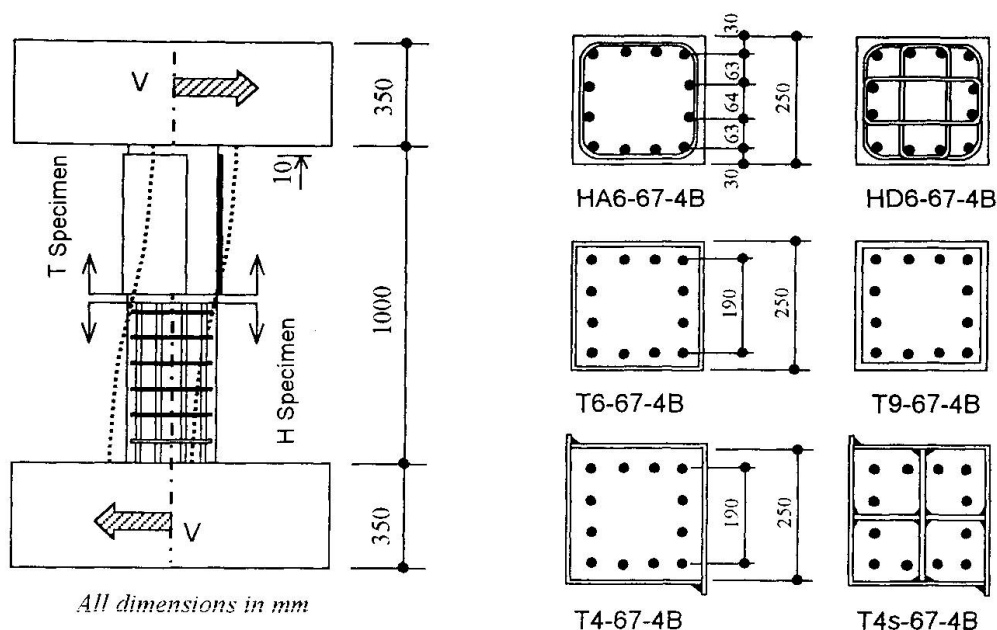
Fig. 1   Details of test specimens

twos confined by high-strength hoop having yield strength of 1026 MPa.   For specimens confined by steel tubes, spaces of 10 mm were provided between loading stubs and steel tube at both ends of the columns.   This was for ensuring that the steel tube provides a confining effect only, rather than a direct resistance to the axial stress due to the applied axial load and bending moment.   Fig. 1 and Table 1 show sectional details and properties of the specimens, respectively.

The variables among the four specimens confined by steel tube were wall thickness of tube as well as with or without inner stiffener.   Variable for the two specimens confined by hoop was configuration type of the hoop.   As shown in Fig. 1, hoop has two types of configuration.   One consisted of one perimeter hoop only, and the other was of square perimeter hoop with two rectangular overlapping hoops.   The level of applied axial load, expressed in terms of axial load ratio ($=N/A_gf_c$), was 0.67 for all specimens, which is twice the upper axial load ratio recommended in the AIJ standards [1] for reinforced concrete column.   Specimens T6-67-4B and T9-67-4B had little different axial load ratios, because the core sectional dimensions of them were different from the other specimens (see Table 1).

Two batches of ready-mixed concrete, with a slump of 180 mm and maximum aggregate size of 20 mm, were used to construct specimens.   The first batch was used for making specimens T6-67-4B and T9-67-4B, and the second for the others.   The target compressive strength of concrete was 41 MPa, and the concrete cylinder strengths at testing stage are given in Table 1.

All specimens were tested under reversed cyclic lateral load while subjected to constant axial load. After applying axial load with a 5 MN universal testing machine, cyclic lateral load was applied through one 500 kN hydraulic jack to deform specimen in a double curvature pattern.   Loading pattern for lateral load was displacement-controlled type with alternating drift reversals.   The peak drifts were increased stepwise from 0.005 rad to 0.03 rad with increment of 0.005 rad after three cycles at each drift level.   The maximum drift was 0.05rad for specimen T4-67-4B and T4s-67-4B with one cycle at each drift level after 0.02 rad.   For specimen HD6-67-4B, the first half cycle of loading in the positive (push) direction reached drift level of 0.01 rad due to miss of operation.   From the subsequent cycle, scheduled loading program was applied.   Applied lateral

Table 1 Properties of the test columns

| Specimen | f_c' (MPa) | Axial load | | Details of transverse reinforcement | | | | | | Type |
		N (kN)	$\dfrac{N}{A_g f_c'}$	ρ_h (%)	f_{yh} (MPa)	d_h (mm)	C (mm)	s (mm)	D_c (mm)	
T4-67-4B	51.1	2109	0.67	7.02	292	4.3	250	0	250	
T4s-67-4B	47.9	1971	0.67	10.5	292	4.3	125	0	250	Tube
T6-67-4B	40.5	1655	0.72	9.66	303	5.6	238	0	238	
T9-67-4B	40.5	1655	0.76	15.0	296	8.5	232	0	232	
HA6-67-4B	40.5	1655	0.67	2.21	1026	6.4	190	27	215	Hoop
HD6-67-4B	40.5	1655	0.67	2.21	1026	6.4	190	55	215	

Note: f_c' = strength of concrete cylinder, A_g = gross sectional

area ρ_h = volumetric ratio of hoop or steel tube f_{yh} = yield stress of transverse steel

d_h = nominal diameter or wall thickness of transverse steel s = hoop spacing

C = unsupported length of transverse steel D_c = dimension of confined core concrete

load was measured by calibrated load cell. Lateral deflection of column was recorded by two 100 mm displacement transducers.

3. Observed behavior and test results

Crack patterns of all specimens are shown in Fig. 2 along with hysteretic lateral load V – drift ratio R relationships. Crack patterns of the specimens confined by steel tubes were observed by cutting and removing steel tubes after the tests. The drift ratio R in Fig. 2 is defined as δ/H, where δ is the lateral deflection, and H is the clear height of column. The dashed line shown in the hysteresis loop of specimen HD6-67-4B represents the first half cycle of loading, which was out of the planned loading program.

Specimen T4-67-4B had the thinnest steel tube with width-to-wall thickness ratio B/t = 60 as its lateral confining material. The specimen showed rapid strength degradation during cycles of lateral loading at 0.015 rad drift level. During subsequent cycle of loading to the peak drift of 0.02 rad, axial shortening of the column due to high axial load became significant, and the steel tube touched the loading stubs and soon buckled. As the steel tube buckled, the specimen lost its axial and lateral load-carrying capacities. This result implies that steel tube with B/t = 60 cannot provide sufficient confinement to make the column ductile under high axial load.

Specimen T4s-67-4B was also confined by square steel tube having B/t = 60, but the steel tube was laterally strengthened by two crossed inner stiffeners provided along 250 mm end regions of the column (see Fig. 1). Having the same wall thickness as steel tube, inner stiffener greatly increased the lateral stiffness, hence confinement pressure, of the thin steel tube, and significant lateral expansion of the concrete was not observed. The specimen exhibited very ductile performance and sustained 90 percent of the peak load at large drift level up to 0.045 rad.

Specimen T6-67-4B had steel tube with B/t = 46 as its lateral confiner. The specimen showed relatively stable response until the drift ratio R = 0.02 rad. During the cycle of loading to the drift ratio of 0.025 rad, steel tube touched loading stub due to accumulation of the axial shortening. However, unlike specimen T4-67-4B, specimen T6-67-4B exhibited higher load-carrying capacity as shown by the dashed line in the V - R hysteresis loop after steel tube had touched the loading stub. Use of thicker steel tube apparently increased not only the confinement pressure, but the
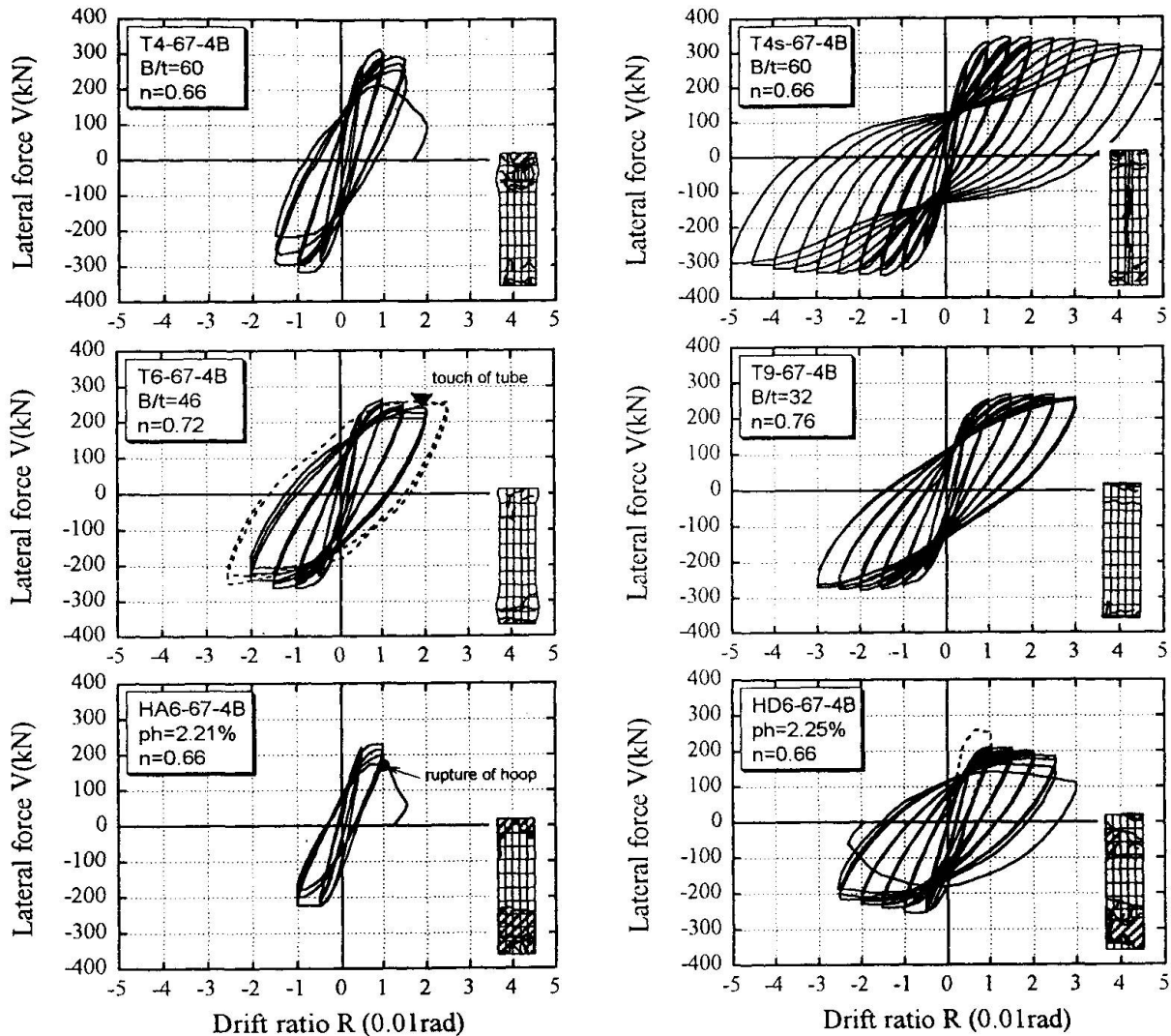
Fig. 2   Hysteretic response of specimens

axial buckling-resistant capacity of steel tube as well.

Specimen T9-67-4B was confined by the thickest steel tube with $B/t = 32$. The specimen showed very ductile behavior until end of test at drift ratio $R = 0.03$ rad. Damage was not observed, and the axial shortening was also very small.

Specimen HA6-67-4B was confined by high-strength conventional hoop. The amount of transverse hoop, expressed in terms of volumetric ratio of the hoop to the core concrete, was 2.21%, which is nearly equal to the maximum amount of hoop effective in resisting shear force [1] This specimen showed rapid strength degradation when the cover concrete commenced spalling at the drift ratio of 0.01 rad. Cover concrete of the column completely spalled off at the end of loading cycles of 0.01 rad. During the subsequent cycle of loading to $R = 0.015$ rad, transverse hoop was broken, and the specimen lost its sustaining capacity to axial load and failed.

Specimen HD6-67-4B had the same quantity of transverse hoop as specimen HA6-67-4B. The difference between them was hoop configuration as shown in Fig. 1. The specimen HD6-67-4B

Table 2 Experimental and calculated results

Specimen	V_{max} (kN)	R_{max} (10^{-2}rad)	R_u (10^{-2}rad)	M_{exp} (kN-m)	M_{cal} (kN-m)	M_u (kN-m)	M_{ACI} (kN-m)	$\dfrac{M_{exp}}{M_u}$	$\dfrac{M_{exp}}{M_{ACI}}$
T4-67-4B	317	0.90	1.52	168	128	155	90	1.08	1.87
T4s-67-4B	338	1.38	4.50	183	147	176	87	1.04	2.10
T6-67-4B	264	1.00	2.01	140	114	142	69	0.99	2.03
T9-67-4B	274	1.50	5.40	149	129	163	62	0.91	2.40
HA6-67-4B	226	0.85	1.05	120	101	121	83	0.99	1.45
HD6-67-4B	254	1.28	2.45	138	101	139*	83	0.99	1.66

Note: V_{max} = maximum experimental lateral force R_{max} = drift ratio corresponding to V_{max}

R_u = drift ratio where the lateral load dropped to 90% of the V_{max}

M_{exp} = experimental ultimate moment M_{cal} = theoretical ultimate moment [2,3]

M_u = enhanced ultimate moment by Eq.1 M_{ACI} = the ACI moment [4]

*: n=0.884 for core section has been used to calculate the enhanced ultimate moment by Eq. 1

responded in a stable manner and sustained 90 percent of its peak load up to the peak drift of 0.025 rad. The cover concrete completely spalled off at drift ratio R = 0.01 rad, but spalling of cover concrete had little negative influence on the seismic performance of the column. This can be attributed to the use of supplementary hoops, which enhanced confinement force of hoop.

4. Ultimate moment capacity and deformation

Experimental moments of all specimens are given in Table 2. The experimental moments were measured as the maximum column end moment at the positive loading within drift ratio of 0.02 rad, including the N-δ moment. The ultimate drift ratios shown in Table 2 were measured as drift ratio where the lateral force dropped to 90% of the peak load. For specimens whose tests were terminated at drift ratio of 0.03 rad, the ultimate drift ratios were determined by extrapolation of the envelop curves. Theoretical moment M_{cal} and M_{ACI} were obtained by using two stress blocks proposed by authors [2,3] and in the ACI codes [4], respectively. confinement effect of steel tube has been taken into consideration in the stress block proposed by authors.

As is obvious in Table 2, the ACI ultimate moments are 45% to 140% conservative due to ignorance of confinement effect of steel tube. By taking confinement effect of steel tube into consideration, the moments predicted by authors method show good agreement with experimental moments. Experimental moments M_{exp} exceeded theoretical moments M_{cal} by 25% on average mainly because of existence of stiff loading stubs at the ends of column, which would apply extra confinement to the compressed concrete at critical end regions of column. To account for the effect of extra confinement from loading stub, authors have developed an empirical formula for the moment enhancement above the predicted moment M_{cal}, of the form [3]

$$\frac{M_u}{M_{cal}} = \begin{cases} 1.10, & n \le 0.3 \\ 1.10 + 0.8(n - 0.3)^2, & n > 0.3 \end{cases} \tag{1}$$

where M_u is the ultimate design moment, and n is the axial load ratio. From Table 2, very good agreement can be observed between the experimental moments and ultimate design moments calculated by Eq. 1. The ratio of M_{exp} to M_u has mean value of 1.00 and standard deviation of 0.06. These results show importance of taking confinement effect of steel tube into account when calculating the ultimate capacity of confined concrete columns.

The experimental ultimate drift ratios are plotted in Fig. 3. The linked horizontal line superimposed in Fig. 3 presents the permissible ultimate drift ratio for well-confined concrete columns recommended in the AIJ guideline [5]. When confined by steel tube, columns show higher ultimate deformation as wall thickness of steel tube is thicker. In addition, use of inner stiffener is very effective in enhancing confinement effect of thin steel tube, hence ultimate moment and deformation capacity of the column. On the other hand, hoop configuration provided by one perimeter hoop only cannot make column ductile enough to satisfy the requirement of AIJ guideline. So, to fully utilize advantage of high-strength hoop, hoop should be used with rational configuration.
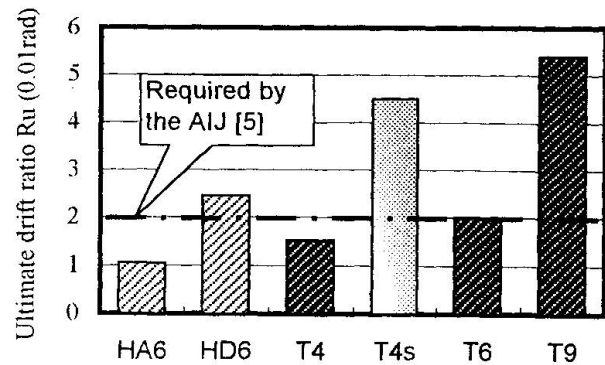

Fig. 3   Ultimate deformation

5.   Conclusions

To make concrete column in high-rise buildings more ductile, this paper proposed two confining methods that involve use of square steel tube and high-strength hoop. The following conclusions can be drawn from the tests reported in this paper on the effectiveness of the proposed methods.

(1)   Confinement of concrete by square steel tubes was effective in enhancing the ductility of reinforced concrete columns under high axial load, but too thin steel tube could not provide sufficient confinement to the column because of its weak lateral stiffness. For concrete column under high axial load to have the ultimate drift ratio of 0.02 rad, one should use steel tube with B/t <46 to confine the column. However, if strengthened with inner stiffener, the thin steel tube having B/t=60 could make column to be able to sustain 90% of the peak load at R = 0.045 rad.

(2)   One single perimeter hoop cannot prevent column under high axial load from brittle crushing failure, even a large amount of high-strength hoops were used. However, use of supplementary hoop could increase confinement effect of hoop, and the column confined by hoop with rational configuration showed very ductile performance at large deformation up to R = 0.025 rad.

References

[1]   Architecture Institute of Japan (AIJ), "Standard for Structural Calculation of Reinforced Concrete Structures," (in Japanese) 1991, pp. 159-161.
[2]   Sun, Y.P. and Sakino, K., "Ultimate Strain and Strength of RC columns Retrofitted by Steel Tubes," Conference Report on Composite Construction, IABSE, Austria, Sept. 1997, pp.675-680.
[3]   Sun, Y.P., Sakino, K., and Yoshioka, T., "Flexural Behavior of High-Strength RC Columns Confined by Rectilinear Reinforcement," J. of Struct. Constr., AIJ, No.486, Aug.1996, pp.95-106.
[4]   ACI Committee 318, "Building Code Requirements for Structural Concrete and Commentary - ACI 318-95," ACI, 1995, pp. 104-105.
[5]   Architecture Institute of Japan (AIJ), "Design Guideline for Earthquake Resistant Reinforced Concrete Building Based on Ultimate Strength concept," (in Japanese) 1990, pp. 186-189.

Seismic Behaviour of Steel Encased Reinforced Concrete Columns

Kazunori WAKAMATSU
Takenaka Corp.
Osaka, Japan

Tatsuo OKAMOTO
Takenaka Corp.
Osaka, Japan

Yukio SOBUE
Takenaka Corp.
Osaka, Japan

Yasuo HIGASHIBATA
Takenaka Corp.
Osaka, Japan

Yasuyoshi MIYAUCHI
Takenaka Corp.
Osaka, Japan

Summary

The earthquake type loading tests of steel encased reinforced concrete (SRC) columns were carried out. The main objectives of this program were to investigate the seismic behavior of SRC columns using high strength longitudinal bars and lateral reinforcing bars and to obtain guideline for its structural design for high-rise buildings.

1. Introduction

The 1995 Hyogoken-Nanbu Earthquake attacked Kobe on January 17, 1995 and brought us the huge destruction. In general, we have thought that steel encased reinforced concrete (SRC) members have more ductility than reinforced concrete ones have. But in this earthquake, a lot of wide flange encased reinforced concrete columns, especially in multiple dwelling houses, received shear failures. To avoid the shear failure, usage of more slender columns is effective. But, in that case, flexural and shear strength will be short due to the small section. Then, high strength longitudinal and lateral reinforcing bars are considered to be used for slender columns to give more flexural and shear strength. We proposed to use the SD490 (yield strength: 490 MPa, ultimate strength: 620 MPa) as the longitudinal bar, and the KSS785 (yield strength: 785 MPa, ultimate strength: 930 MPa) as the lateral reinforcement for SRC columns. However, the superposed strength method in the SRC Standards published by AIJ is not applicable to such high-strength materials. This paper presents empirical results of tests on prototype columns. The main objectives of this test were to determine the seismic behavior of the column using these reinforcing bars and to obtain guidelines for its structural design for high-rise buildings.

2. Beam-column test

2.1 Test Specimen

Seven column specimens were tested under earthquake-type loadings. The section of concrete(35 ×35 cm, specified compressive strength: 35.3 MPa) and that of cross shaped steel(2H-210×80 ×6×16, tensile strength: 490 MPa) are common to all specimens. The variables are:

1) shear span to depth ratio(M/QD=2.0 and 1.29);

2) area ratio of longitudinal reinforcement (Pt=0.47, 0.65 and 0.74%);

3) lateral reinforcement ratio(Pw=0.23～0.74%); and

4) axial load levels (n) with 0.1, 0.3 and 0.5, where n is calculated by equation (1) and (2).

$$n = N/N0 \tag{1}$$

$$N0 = B \cdot D \cdot c\,\gamma\,u \cdot Fc + As \cdot s\,\sigma\,y + Ar \cdot r\,\sigma\,y \tag{2}$$

where: $c\,\gamma\,u = 0.85\text{-}2.5 \cdot sPc$

$sPc = s\bar{a}c/BD$

sāc : Total area of compressive steel (cm²)

N0 : Ultimate compressive strength (N)

B : Column width (cm)

D : Column depth (cm)

Fc : Specified compressive strength (MPa)

As, Ar : Total areas of steel, longitudinal reinforcement (cm²)

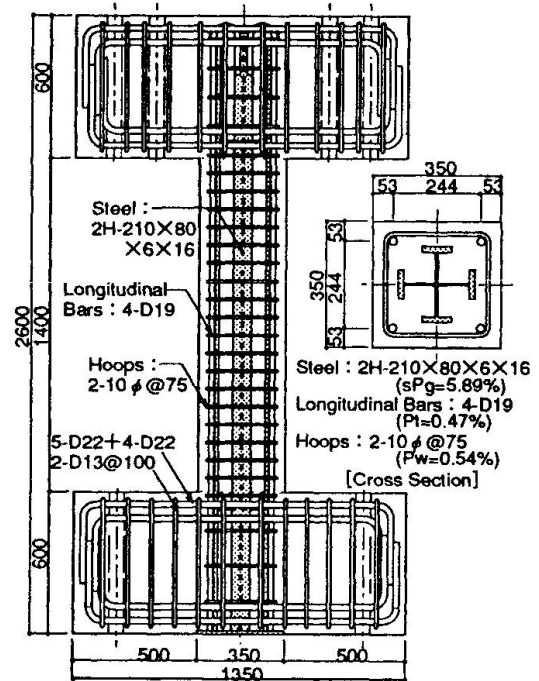s σ y,r σ y : Yield strengths of steel, longitudinal reinforcement (MPa)

Fig.1 Test Specimen

Table 1 Details of Test Specimens

Specimen		h (mm)	Longitudinal Reinforcement		Lateral Reinforcement		Axial Load Ratio	Qmu (kN)	Qsu (kN)	Qsu/ Qmu
			Arrangement	Pt (%)	Arrangement	Pw (%)	n			
M series	1	1400 (M/QD =2.00)	4-D19	0.47	2-10φ@75	0.54	0.3	530	666	1.26
	2						0.5	514	666	1.30
	3		4-D16, 8-D13	0.74	2-10φ@55	0.74	0.3	570	718	1.26
	4						0.1	572	718	1.26
S series	5	900 (M/QD =1.29)	8-D16	0.65	2-6φ@80	0.23	0.3	888	561	0.63
	6				2-6φ@80		0.5	857	561	0.65
	7				2-6φ@40	0.45	0.3	888	712	0.80

h : Inside measurment of column   Pt : area ratio of longitudinal reinforcement
Pw : Lateral reinforcement ratio
Axial load ratio : Ratio of axial load to ultimate compressive strength
Qsu : Ultimate shear strength
Qmu = (Mu1+Mu2)／h
    Mu1 : Ultimate flexural strength of upper end
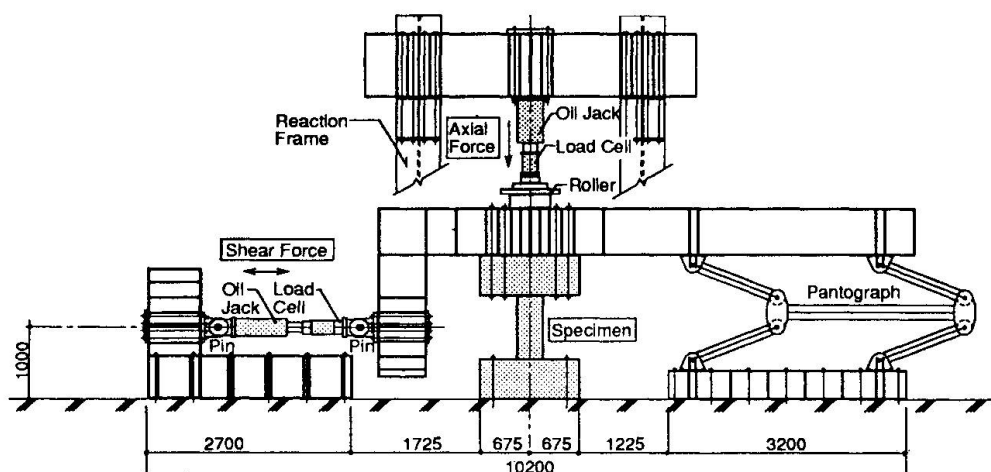   Mu2 : Ultimate flexural strength of lower end

Fig.2 Loading apparatus

Table 2 Mechanical Properties of Concretes

*1 unit (MPa)

Specimen	fc *1	fc' *1	E₁/sfc' (GPa)	ft *1
1~4	35.3	39.0	32.3	3.0
5~7	35.3	38.7	28.5	2.8

fc' : Measured compressive strength of concrete

$E_1/_s fc'$: Secant Modulus of concrete at fc'/3

ft : Measured splitting tensile strength

Table 3 Mechanical Properties of Steel

*1 unit (MPa)

	Thickness (mm)	f_y *1	f_u *1	ε_u(%)
Flange	16	326.0	527.2	27.64
Web	6	372.4	526.4	26.38

f_y : Yield strength of steel

f_u : Ultimate strength of steel

ε_u : Ultimate Strain

Table 4 Mechanical Properties of Steel Bars

Type of Steel Bars		f_y (MPa)	f_u (MPa)	ε_u (%)
Longitudinal Reinf.	Deformed Bar 13mm dia	569.3	699.0	15.43
	Deformed Bar 16mm dia	531.9	710.0	15.99
	Deformed Bar 19mm dia	566.4	771.8	15.95
Lateral Reinf.	High Strength Bar φ6mm	870.4	904.2	12.53
	High Strength Bar φ10mm	896.6	1096.9	12.30

f_y : Yield strength of steel bars

f_u : Ultimate strength of steel bars

ε_u : Ultimate Strain

The variables and ultimate shear strength of each specimen are as listed in **Table 1**. The full capacities of the specimen 1~4 in M series are determined so as to make them exhibit flexural-type failure mode and those of the specimen 5~7 in S series are determined so as to make them exhibit shear-type failure mode. The mechanical properties of concrete, steel and reinforcing bars are shown in **Table 2,3** and **4**. Cyclic horizontal load is applied to each specimen while the axial load keeping constant. The inflection point is kept at middle height of the column by using testing apparatus, as shown in **Fig.2**.

2.2 Test Results and Discussions

Table 5 gives the test results. **Fig. 3** and **4** show a comparison of measured horizontal load-story drift angle relations and the envelopes of horizontal load-story drift angle relations. The following results can be derived from these table and figures:

M series (specimen 1~4): Specimen 3 shows excellent ductility and lateral load carrying capacity up to the story drift angle exceeding 50×10^{-3}rad. On the other hand, specimen 1,2, and 4 tested under the higher axial compressive load of 30,50% of the ultimate compressive strength behaves in less ductile manner when compared with specimens 3. The failure mode for specimen 3 is flexural failure, and those for all other specimens are flexural compressive failure. The ductility of every specimen is reduced after reaching maximum strength, especially for specimen 2. It seems that this is due to the difference of the axial load levels between specimens. The story drift angles (R_M) at which the maximum lateral loads are sustained vary from 7.0 ~ 12.4×10^{-3}rad. and the ultimate story drift angles (R_U) at which 80% of the maximum lateral loads are sustained vary from 12 ~ 50×10^{-3}rad. The ratios of the measured ultimate strength (V) to the calculated strength by using superpose method[1] (Vcal) vary from 0.91 ~ 0.94. The strain of the concrete at ultimate compressive strength is 1750×10^{-6} and the yield strains of the longitudinal bars are $2647 \sim 2922 \times 10^{-6}$, respectively, and the compressive concrete had crushed before the longitudinal bars yielded. The longitudinal bars maintain the elastic state when the maximum lateral loads are sustained and this might be the reason why the ratios (V/Vcal) of the measured ultimate strength to the calculated one is smaller than 1.0. In case that the ultimate strength is calculated by using

Table 5 Test Result

Specimen		N (kN)	N0 (kN)	n	Maximum Strength			R_M ($\times 10^{-3}$ rad.)	R_U ($\times 10^{-3}$ rad.)
					Measured V (kN)	Calculated Vcal (kN)	V / Vcal		
M Series	1	2112	7040	0.30	496	530	0.94	10.0	30
	2	3521	7040	0.50	482	514	0.94	7.0	12
	3	739	7392	0.10	534	570	0.94	12.4	50
	4	2217	7392	0.30	521	572	0.91	9.9	40
S Series	5	2162	7207	0.30	599	561	1.07	5.1	15
	6	3604	7207	0.50	617	561	1.10	4.2	12
	7	2162	7207	0.30	651	712	0.91	5.1	30

N : Axial load

N0 : Ultimate compressive strength

V : Empirical value of shear force

Vcal : Smaller one of the two values of shear forces Qmu and Qsu , which are calculated by using superposed method[1]

R_M : The story drift angle at which the maximum lateral load was sustained

R_U : The ultimate story drift angle at which 80% of the maximum lateral load was sustained
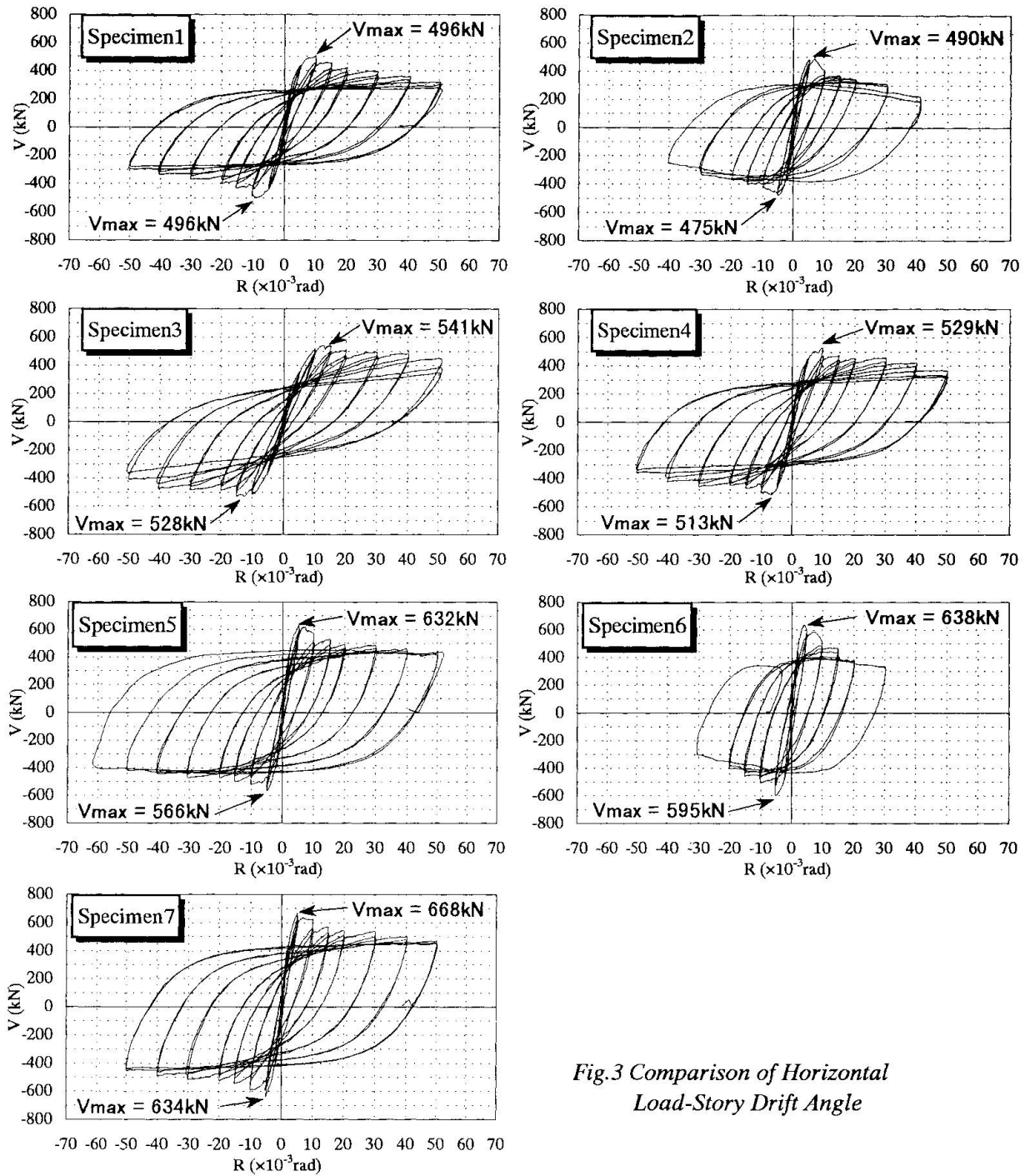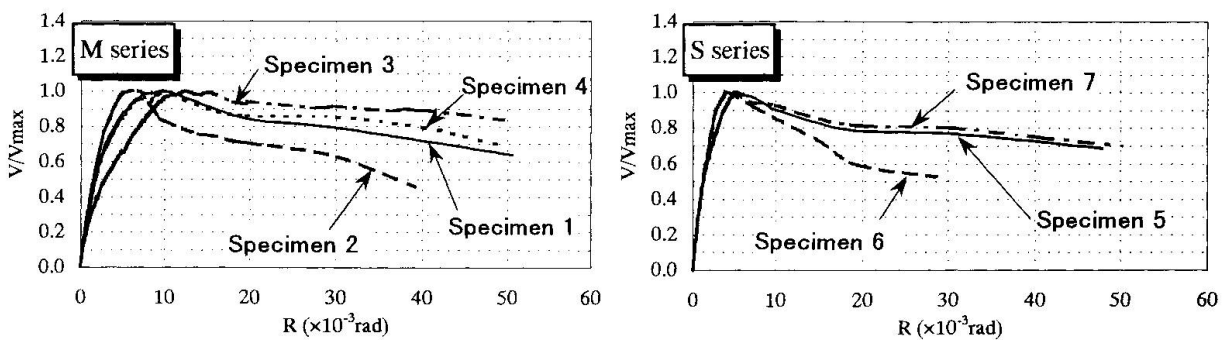
Fig.3 Comparison of Horizontal Load-Story Drift Angle

Fig.4 Envelopes of Horizontal Load-Story Drift AngleCurves

the stress of the longitudinal bars when their strains are 1750×10^{-6}, the ratios (V/Vcal) of the measured ultimate strength to the calculated one vary from 1.01 ~ 1.04.

S series (specimen 5~7): The failure mode for each specimen is shear failure. Specimen 5 and 7 show enough ductility and lateral load carrying capacity up to the story drift angle exceeding 5×10^{-2}rad. However, specimen 6 tested under the higher axial compressive load of 50% of the ultimate compressive strength behaves in less ductile manner when compared with specimens 5. It seems that this is due to the difference of the axial load levels between specimens as same as M series. The story drift angles (R_M) at which the maximum lateral loads are sustained vary from 4.2 ~ 5.1×10^{-3}rad. and the ultimate story drift angles (R_U) at which 80% of the maximum lateral loads are sustained vary from 12 ~ 30×10^{-3}rad.. The ratios (V/Vcal) of the measured ultimate strength to the calculated strength of specimen 5 and 6 (Pw=0.23%) are 1.07 and 1.10, respectively, and that of specimen 7 (Pw=0.45%) is 0.91. Therefore, the ratio V/Vcal tends to decrease as lateral reinforcement ratio (Pw) increases. This might be due to the fact that the lateral reinforcing bars maintain the elastic state when the maximum lateral load is sustained.

3. Conclusions

The conclusions obtained from the experimental study are summarized as follows.

(1) The SRC columns using high strength longitudinal bars and lateral reinforcing bars have the same sufficient ductility as those of SRC columns using normal strength ones.

(2) Axial load level influences the flexural ductility of the SRC column.

(3) In this test, the measured ultimate strength of columns using high strength longitudinal bars and lateral reinforcing bars are a little smaller than the calculated strength according to the SRC Standards[1]. To evaluate the ultimate strength of these columns, it is necessary to consider the relation between the strain of the concrete at ultimate compressive strength and the yield strain of the longitudinal bar in case of flexural failure mode, and also the strength balance between concrete and lateral reinforcing bar in case of shear failure mode.

4. References

1) Architectural Institute of Japan, " Standards for Structural Calculation of Steel Reinforced Concrete Structures", 1987.

Ultimate Strength and Collapse Mechanism of Composite Frames under Seismic Loading

Bunzo TSUJI
Prof.
Kyoto Univ.
Kyoto, Japan

Bunzo Tsuji, born 1940, received his doctorate degree from Kyoto Univ. His main research interests include the constitutive equations of the steel and concrete, stability of steel structures, and ultimate strength of steel and composite structures.

Summary

In seismic design of composite building frames in Japan, the weak beam strong column moment frame system is usually adopted. In the case of composite low rise building frames, the plastic hinges formed at beams and columns show not only the rotational deformation but also the axial elongation. Considering these axial and rotational deformations, the real collapse mechanism is somewhat different from the expected one. In this paper, the ultimate strength and the collapse mechanism of the composite frames under the vertical and horizontal loads are discussed. Using geometric compatibility condition, a recurrence formula is derived between the rotation angles of the columns and beams, and a procedure for obtaining the ultimate strength and the collapse mechanism is shown. The analytical results show that plastic hinges should be formed not only at the beam ends and column bases but also at almost all the lower ends of the columns.

1. Introduction

In seismic design of composite moment frames, the weak beam strong column system is usually adopted. In this case, plastic hinges are supposed to form at all beam ends and column bases. A plastic hinge formed in the composite members shows not only the rotational deformation but also the axial deformation. The effect of this axial deformation at the plastic hinges on the collapse mechanism is important, but only a few researches have been made[1,2,4]. In this paper, the ultimate strength and the collapse mechanism of the composite frames are discussed, considering both the rotational and axial deformations at the plastic hinges. A recurrence formula is obtained between the rotation angles of the members. Using the formula, a procedure to obtain the ultimate strength and the collapse mechanism is shown, and some numerical analyses are carried out.

2. Ultimate Strength and Plastic Deformation of Composite Members

Fig.1 shows a composite member having a rectangular concrete cross section with an ideal I-section steel. For simplicity, the cross section is idealized into three point model such as shown in the figure. Considering rigid perfect plastic stress-strain relationship for both concrete and steel, such as shown in Fig.2, the yield condition of the idealized model cross section can be obtained as a hexagonal shape under the axial force (N) and bending moment (M), such as shown in Fig.3(a)[3,4]. The associated flow rule shows that the ratio between axial deformation e and rotation ω is constant when the generalized stress (N,M) moves on each line of the yield locus, such as

shown in Fig.3(b).

$e = -(D/3)\omega$ for $-{_s}N_o \leq N \leq {_c}N_o/3$

$e = 0$ for ${_c}N_o \leq N \leq 2{_c}N_o/3$

$e = (D/3)\omega$ for $2{_c}N_o \leq N \leq {_c}N_o + {_s}N_o$

where ${_s}N_o = 2{_s}\sigma_o A_f$ and ${_c}N_o = {_c}\sigma_o BD$. If the axial load level is low ($-{_s}N_o \leq N \leq {_c}N_o/3$), axial elongation occurs when the plastic hinge rotates, such as shown in Fig.3(c).
The yield condition of this range is

$f = N - ({_s}N_o / {_s}M_o)M + {_s}N_o = 0$

Rate of energy dissipation D can be obtained as a simple form as follows:
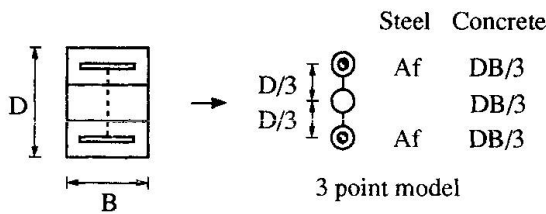
$D = N \cdot e + M \cdot \omega = {_s}M_o \cdot \omega$
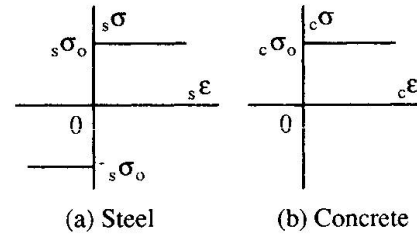

Fig.1 Model of composite cross section

Fig.2 Stress strain relations

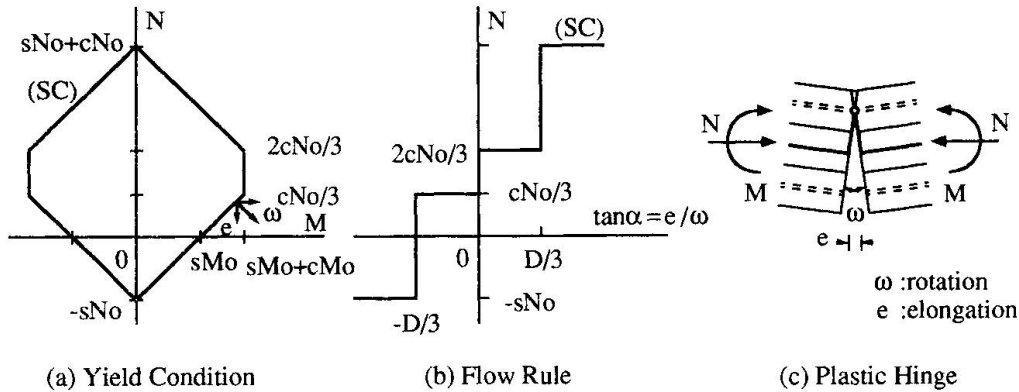(a) Yield Condition   (b) Flow Rule   (c) Plastic Hinge

Fig.3 Yield condition and associated flow rule

3. Ultimate Strength and Collapse Mechanism of Composite Frames

3.1 Design of Composite Frames

The composite frames subjected to vertical and horizontal forces are designed to collapse by forming plastic hinges at all beam ends and column bases, using simple plastic analysis. To realize the weak beam and strong column frames, the total amount of plastic moment of the columns is 1.2 times as large as that of beams gathering at each beam to column joint. The vertical and horizontal forces are applied at each beam to column joint such as shown in Fig.4. The horizontal force is specified in conformance with the building standard law of Japan. The base shear coefficient is assumed to 0.3 for the ultimate strength stage, in this case. For simplicity, all the column concrete cross sections are the same ($D_c x D_c$) and also all the beam cross sections are the same ($D_b / 2 x D_b$) such as shown in Fig.5. The required plastic moment capacity of each member ${_s}M_o$ is adjusted by the cross sectional area of the steel I section. The plastic moment of the outer column is assumed to be 0.6 times to that of the inner column.
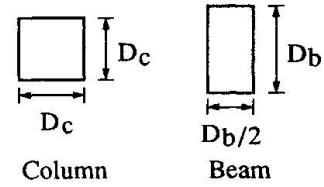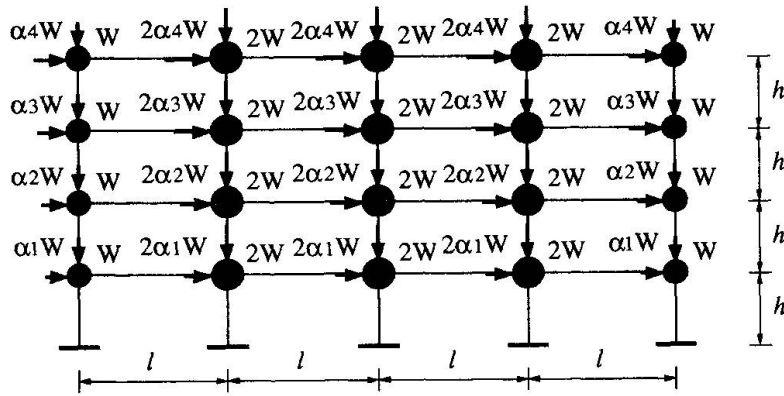
Fig.4 Composite frames subjected to vertical and horizontal loads   Fig.5 Cross section

3.2 Rotation Angle of the Members

The plastic hinge shows not only rotation but also elongation when the axial load revel is low. According to the axial deformation at the plastic hinges, elongation of the beam or the columns occurs. Fig.6(a) shows a possible collapse mechanism of a 2-span 3-storied frame. The plastic hinges are supposed to be formed at all beam ends and column bases, according to the simple plastic analysis. But this collapse mode (collapse mechanism A) shows the additional plastic hinges formed at some lower ends of the columns, due to the axial elongation of the beams. And elongation of the column plastic hinges brings the rotational deformation to the beams. On the basis of geometric compatibility condition, the rotation angle of the columns $\omega_c(i, j)$ can be expressed as follows :

$$\omega_c(2,3) = \omega_c(3,3) = \omega_c(1,3)$$

$$\omega_c(1,j) = [1 - (2D_b / 3hK_r)]\omega_c(1, j+1)$$

$$\omega_c(2,j) = [1 - (2D_b / 3hK_l)]\omega_c(2, j+1) + [\omega_c(1, j+1) - \omega_c(1, j)] / K_l$$

$$\omega_c(3,j) = [1 - (2D_b / 3hK_l)]\omega_c(3, j+1) + \sum_{i-1}^{2}[\omega_c(i, j+1) - \omega_c(i, j)] / K_l$$

where $K_l = 1 + (D_b / 3h)[1 - (2D_c / 3l)]$ and for j=1,2.

And the rotation angle of the beams $\omega_b(i, j)$ can be expressed as follows:

$$\omega_b(i, j) = (D_c / l)[\omega_c(i, j) - \omega_c(i, j-1)]$$

for i=1,2,3 and j=1,2.

Fig.6(b) shows another possible collapse mechanism (collapse mechanism B) of the same frame.

(a) Collapse mechanism A   (b) Collapse mechanism B
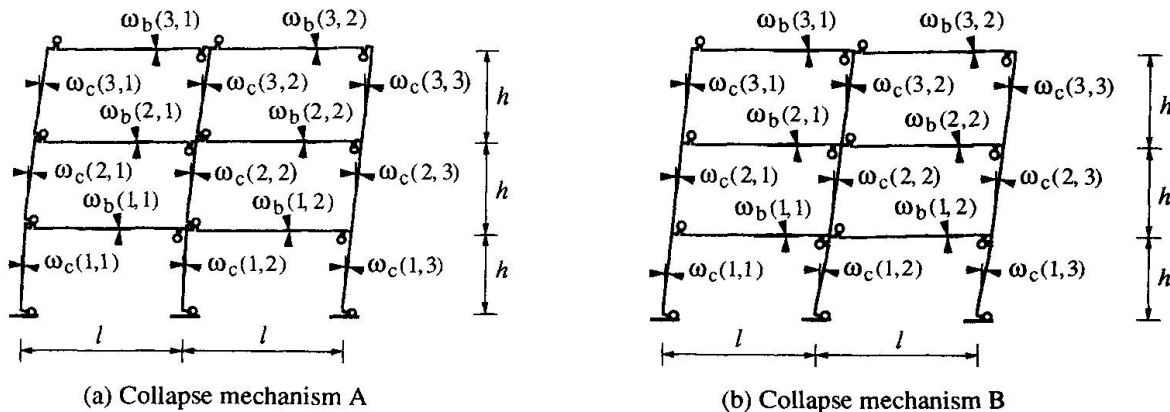
Fig.6 Collapse mechanism of 2-span 3-storied composite frame

The left hand side column forms a plastic hinge only at the column base. In this case, additional plastic hinges are formed at the upper end of another first-story columns. Using geometric compatibility condition, the rotation angle of the columns and beams can be expressed by the following equations:

$$\omega_c(1,2) = \omega_c(1,3) = [1 + (2D_b / 3hK_r)]\omega_c(1,1)$$

$$\omega_c(2,j) = \omega_c(1,1)$$

$$\omega_c(3,j) = \omega_c(1,1)$$

$$\omega_b(i,j) = 4D_cD_b /(9h/K_r)$$

where $K_r = 1 - (4D_cD_b / 9hl)$ and for i=1,2,3 and j=1,2.

Using the rotation angle of the column having a plastic hinge only at the column base, $\omega_c(1,1)$ in this case and $\omega_c(1,3)$ in the former case, the rotation angles of another columns and beams can be expressed by the recurrence formula shown above. The recurrence formula can be obtained for any composite frames designed according to the conditions shown in section 3.1.

3.3 Ultimate Load and Collapse Mechanism

The ultimate load and the collapse mechanism of the frames (from 2-span 2-storied to 6-span 6-storied frames) will be discussed in this section. Assuming the position of a column with a plastic hinge only at the column base, rotation angles of another columns and beams can be expressed, using the recurrence formula. The ultimate load factor λ associated with an assumed collapse mechanism can be obtained using the principle of virtual work as follows:

$$\lambda \sum_{j=1}^{m+1} \sum_{i=1}^{n} \alpha(i,j)W(i,j)u(i,j) - \sum_{j=1}^{m+1} \sum_{i=1}^{n} W(i,j)v(i,j)$$

$$= \sum_{j=1}^{m+1} \sum_{i=1}^{n} \{\xi(i,j,l)_c \omega_o(i,j,l) + \xi(i,j,u)_c \omega_o(i,j,u)\}_{sc} M_o(i,j)$$

$$+ \sum_{j=1}^{m} \sum_{i=1}^{n} \{\xi(i,j,l)_b \omega_o(i,j,l) + \xi(i,j,r)_b \omega_o(i,j,r)\}_{sb} M_o(i,j)$$

where $\alpha(i,j)$ shows the ratio of the lateral load to the vertical load $W(i,j)$ and $u(i,j)$ and $v(i,j)$ are horizontal and vertical displacements at the (i,j)th joint. $_c\omega_o(i,j,l)$ and $_c\omega_o(i,j,u)$ show the rotation of the plastic hinges at the lower end (l) and the upper end (u) of the (i,j)th column, and $_b\omega_o(i,j,l)$ and $_b\omega_o(i,j,r)$ the rotation of the plastic hinges at the left side (l) and the right side (r) of the (i,j)th beam. $\xi=1$ is for active plastic hinge and $\xi=0$ without plastic hinge. Changing the position of the column with plastic hinge only at its base in turn from left to right, the corresponding ultimate load factor can be obtained. According to the upper bound theorem of plasticity, the minimum load factor obtained is the real collapse load factor and the associated mechanism is the real collapse mechanism. Table 1 shows the collapse load factors calculated. $\lambda=1$ shows the load factor obtained using simple plastic analysis. As the number of stories increases, the collapse load factor decreases, and as the number of spans increases, the collapse load factor increases in a gentle manner, because the effect of the axial force of the beams on the bending capacity is small. Table 2 shows the position of the column forming plastic hinge only at the column base. The position of the column is usually at the right part of the frame, and as the number of stories increases and as the number of spans decreases, the position moves to the right end. So almost all the additional plastic hinges are formed at the lower end of the columns. Fig.7 shows an example of the collapse mechanism. The column having a plastic hinge only at the column base is the 2nd column from the right (j=6). The bar graph shows the ratio of the rotation angle of the plastic hinges formed. In the upper part of the frame, rotation of plastic hinges at the lower end of the columns is very small. In the lower part of the frame, rotation of plastic hinges at the beam ends or the column bases decreases as the number of spans (j) decreases but rotation increases at the

Table 1 Collapse load factor λ

number of stories	number of spans	2	3	4	5	6
2		1.123	1.126	1.131	1.136	1.141
3		1.082	1.084	1.086	1.089	1.090
4		1.065	1.067	1.069	1.071	1.072
5		1.053	1.055	1.056	1.058	1.059
6		1.047	1.046	1.047	1.049	1.050

Table 2 Position of the column forming plastic hinge only at the column base (j)

number of stories	number of spans	2	3	4	5	6
2		j=2	3	4	5	5
3		3	4	5	5	6
4		3	4	5	5	6
5		3	4	5	6	6
6		3	4	5	6	6

lower end of the columns as j decreases. Fig.7 shows not only the result of the 6-span 6-storied frame but also the information of another frames. For example, the collapse mechanism of the 4-span 4-storied frame can be shown by the dotted region in Fig.7. On the basis of the results shown in Table 1, the collapse mechanism and the rotation angles of the plastic hinges of the composite frames ranging from 2-span 2-storied to 6-span 6-storied can be obtained.

o : plastic hinge
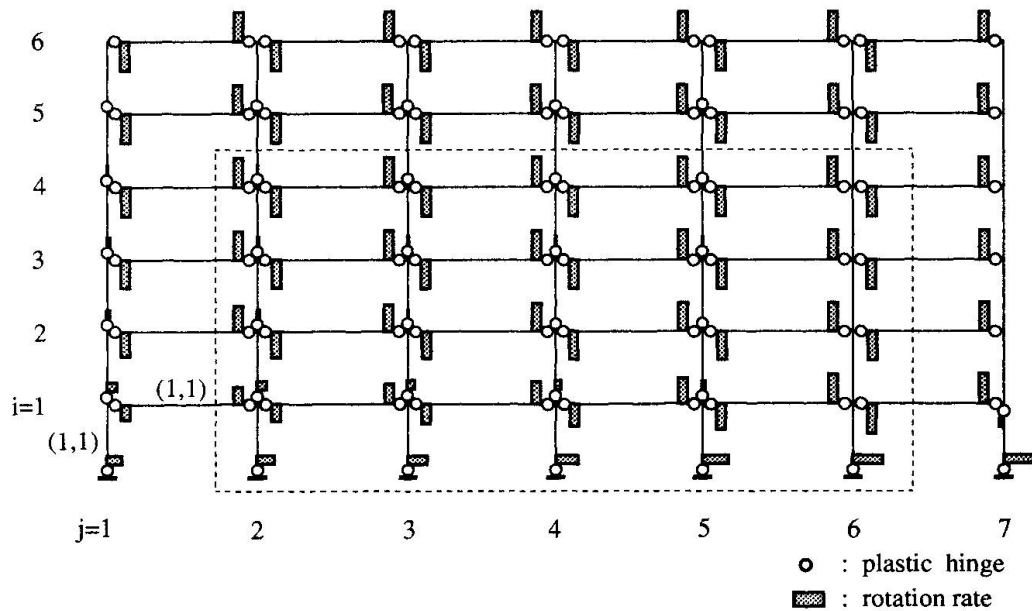▓▓ : rotation rate

Fig.7 Collapse mechanism and rotation angle of plastic hinges

4. Conclusions

This paper presented a method for obtaining the ultimate strength and the collapse mechanism of the composite frames subjected to seismic force, considering the yield condition of the composite

members and the associated flow rule. A recurrence formula is derived between the rotation angles of the plastic hinges formed at the beams and columns. Using the formula, the collapse mechanism of the composite frames composed of strong columns and weak beams is clarified, in the case of the low rise buildings. The real collapse mechanism shows that the plastic hinges are formed not only at the beam ends and column bases but also at almost all the lower end of the columns. The distribution of rotation at the plastic hinges changing from hinge to hinge, is also clarified.

References

[1] Sakata,H.,Hayashi,S.,Wada,A. and Kokusho,S:An experimental study on elastic and plastic behavior of reinforced concrete beam in consideration axial restriction effect of deformation, Jour. of Structural and Construction Eng. AIJ, No.380,pp.45-55,1987 (in Japanese).

[2]Sakata,H.and Wada,A.:Experiments on reinforced concrete one-twentieth scale model frames, Jour. of Structural and Construction Eng. AIJ, No.403,pp.45-55,1989 (in Japanese).

[3]Tsuji,B. and Wakabayashi,M.:Ultimate strength of composite beam-columns and beam-column joints using superposed strength method, Proc. of Plasticity '95, 1995,pp.467-470.

[4]Tsuji,B.:Ultimate strength of composite structures using superposed strength method,Proc. International Conference on Composite Construction,1997,pp.639-644.

Advanced Composites for Earthquake Resistant Structures

Peter HEAD
Chief Executive
Maunsell
Beckenham, UK
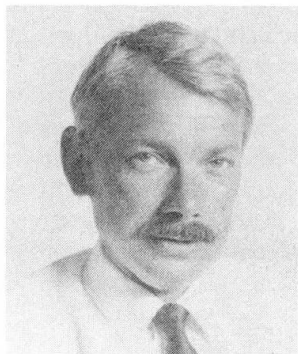
Peter Head has played a key role in research and design development leading to the introduction of advanced composites in civil and structural engineering. Notable successes are the world's first all composite footbridge, first advanced composite road bridge and one of the first all composite multi-storey buildings. He was awarded the Royal Academy of Engineering's Silver Medal in 1995 for an outstanding personal contribution to British Industry.

Summary

Lightweight high-strength advanced composite materials are now being used to retrofit and strengthen many earthquake-prone structures in Japan and USA. Little attention has been paid to the role these materials could play in the design of a new generation of building and bridge structures which have much greater resistance to earthquakes. The high strength to weight ratio of fibre reinforced polymers makes them ideally suited to this role and development work in new forms of composite structure carried out over the last ten years points the way forward. The paper examines this work in detail and shows the new forms of structure that could be adopted in the future to provide more cost effective and reliable solutions.

1.   Introduction

Advanced composite fibre reinforced polymer materials are now being introduced into a wide range of civil and structural engineering applications. In Japan these include concrete reinforcement and prestressing using carbon fibres, ground anchors using carbon and aramid fibres and rock bolts using glass fibres. Perhaps the largest application area is the retrofit strengthening of existing reinforced concrete structures to improve their resistance to earthquake damage. The high strength and stiffness characteristics of the fibres, when bonded to and wrapped around concrete columns and beams has been found to greatly increase the ductability of the reinforced concrete in the rapidly changing stress cycles experienced during earthquakes.

The stresses generated in earthquakes are a direct function of the mass and dynamic frequency response of the structure. Considerable design development has taken place in the last thirty years to refine the way in which steel and concrete are used in tall buildings and bridges to improve earthquake resistance and further developments are reported at this Conference.

However most findings are reported with no recognition of the important role that advanced composite materials could play in this design area in the future. Research work carried out in the United Kingdom over the last 15 years has demonstrated new structural forms that can be used to build lightweight advanced composite bridges and building structures.

The paper presents detailed information on these systems and then indicates using some design studies how they might be applied in the future to achieve reliable but effective solutions for major structures in earthquake prone areas. The paper concludes by suggesting areas of research for the future.

2.   Advanced Composite Materials and Building Systems

Advanced composite materials are fibre reinforced polymer structural sections in which the continuous fibres have high strength and stiffness and are orientated in the direction of maximum stress (Fig.1). Most sections currently used in construction are pultruded and typical properties for different fibre types are shown in Table 1. Important physical characteristics are the high strength to weight ratio compared with steel and concrete which makes the materials more attractive as the structure span and height increases. Designs, particularly when using glass reinforcement, are governed by stiffness rather than strength, because of the high strength to stiffness ratio. Hence in actual designs we find that the low structural weight reduces cyclical dynamic earthquake forces in these structures and there is also a large reserve of strength and strain capability before rupture. Although the materials are inherently brittle in tensile tests, well designed structures exhibit much improved earthquake resistance. The method of construction and form of connection are, however, critical.

Fibre Reinforcement		Glass	Carbon	Aramid	High Tensile Steel Wire
Fibre Fraction	%wt	80	72	67	-
Relative Density	ρ	2.31	1.57'	1.36	7.86
Tensile Strength τ	GPa	0.95	1.61	1.59	1.82
Tensile Modulus ε	GPa	50	136	64.3	200
Specific Strength	τ/ρ	44	105	119	24
Specific Modulus	ε/ρ	21.6	86.6	47.3	25.4

Table 1: Properties of composites with high proportions of unidirectional fibre reinforcement
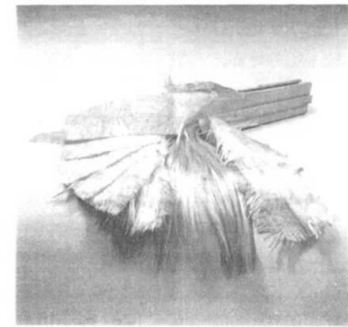
Fig. 1 Pultruded section showing glass reinforcement

The Advanced Composite Construction System (ACCS) was conceived and developed by Maunsell to try to meet the growing demand for a lightweight modular system for constructing buildings and bridges which would reduce the labour costs for assembly and would provide lower capital and operating costs. Other systems may come along in the future but this proven one enables new forms of bridge and building to be illustrated. The system that was conceived and patented in 1982 is a cellular system of components (Fig 2) which can be formed around an insulating core.
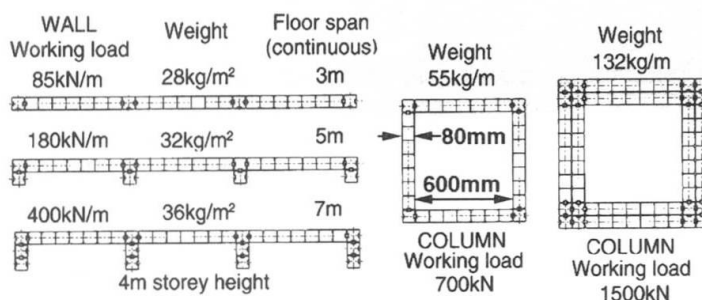

Fig. 2 ACCS components

Walls, columns, beams, bridge girders, floors and roofs can be built using just three primary components pultruded from glass fibres and a suitable thermoset resin and insulating core materials. Structures can be designed using a fully developed limit state design method which is consistent with British and European building codes (1) (Fig 3).

The unique method of connection allows any two components to be brought together, side by side, with epoxy adhesive applied to one face, and by sliding the toggle connector into the groove which holds the components together in accurate alignment while the adhesive cures. In site applications, heaters can be used to achieve controlled and rapid cure.

Fig. 3 LINK beam being assembled at the works

The first Research Programme undertaken on structures built from this System was a LINK programme carried out at the University of Surrey between 1991-93 in which two major beams, each 18 metres long, were built (Fig 3) and subjected to a wide range of long and short term static and dynamic load tests (2), including full flexural tests to
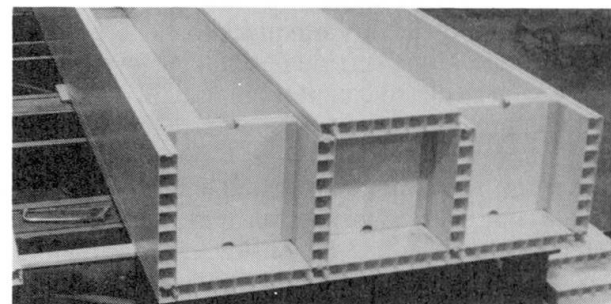
destruction. Small components were also subjected to a full range of accelerated weathering, fatigue, fire and strain aging tests.

3.   Bridge Decks

ACCS has been used to build a variety of different bridge decks. The beam shown in Fig 3 has been used for the design of footbridges with spans up to 17 metres (Fig 4) and road bridges with spans up to 12 metres (to be constructed in 1999). The weight of the beams is 40% of an all steel design and less than 15% of a steel composite solution with a concrete deck. Hence in addition to offering excellent durability, the lightweight structures

Fig. 4 Parson's Bridge, UK

offer much reduced vertical and horizontal earthquake forces generated in support structures.
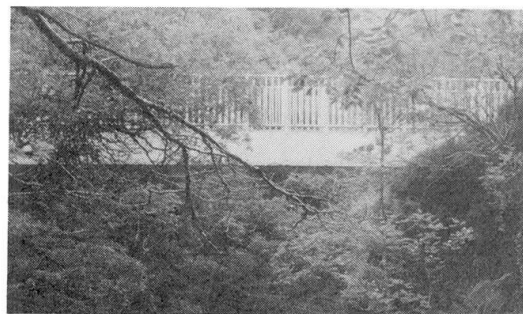
Designs are also being progressed in which the advanced composite materials are used to form an aerodynamic enclosure and torsional box connected to a lightweight steel space frame truss (Fig 5). This system is called *SPACES* and offers construction (3) and earthquake resistant advantages also. The weight can be significantly less than a traditional truss bridge deck.

Fig. 5 Poole Harbour bridge design, UK

4.   Building Structures

4.1   Beam, Column, Floor, Wall and Roof Sections

Figures 2 and 6 show typical configurations of ACCS used in beam and slab floors, load bearing walls and columns. Table 2 shows some comparative weights of typical steel, concrete, composite and brick structures which provide similar load carrying and other functional characteristics. It can be seen that very substantial weight reductions can be achieved using advanced composite materials and these can have major advantages in reducing foundation costs and improving earthquake resistance in tall buildings. Earthquake resistance also derives from the high strength to weight ratio and lower elastic stiffness. A two storey office building was built in Bristol in 1992 using this System and no other materials. It has been used successfully ever since (Fig 7).
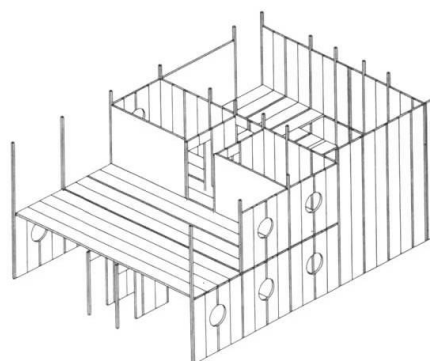

Fig. 6 Typical configuration of ACCS uses in buildings

Fig. 7 Second Severn Crossing site office

Typical Walls	ACCS Wall	= 0.3 Kn/m^2
	Brick Cavity Wall	= 2.0 Kn/m^2
	Reinforced Concrete Wall	= 2.2 Kn/m^2
Typical Floors (5 metre span)	ACCS Floor	= 0.35 Kn/m^2
	Reinforced concrete floor	= 3.3 Kn/m^2
	Lightweight concrete/metal deck floor	= 2.2 Kn/m^2

Table 2: Comparative weights of different materials

4.2   Thermal Insulation

ACCS sections 80mm thick with a polyurethane foam core have a thermal insulation value of U = 0.35 W/m^{2}K. This meets UK requirements for domestic buildings and offices. Buildings can be

fitted with double glazed windows with pultruded GRP window frames and this then provides a largely integral glass structure with excellent thermal insulation and uniform temperature expansion characteristics. The GRP sections overcome the cold-bridge effect and buildings have been found to be comfortable and have low running costs. Window seals maintain their integrity because of the lack of differential expansion.

4.3   Fire Performance

ACCS sections manufactured from glass fibre and isopthalic polyester resins, with a polyurethane foam core, have been tested in a whole range of fire tests (Fig 8). The high glass content in each pultruded section means that heat is not conducted away from the fire source, or through the panel thickness. Also glass has a relatively high melting temperature and the cellular configuration of the panels maintains load carrying integrity for long periods of time. Panels meet BS 476 Part 7 Class 1 surface spread of flame test requirements and can provide up to 60 minutes fire resistance as a wall or floor section in a BS 476 Part 21 Test. Surface coatings can be used to achieve Class 0 spread of flame performance and to further inhibit smoke emission. If smoke is a design criterion, alternative resins are available for pultrusion such as phenolics and methacrylates.

Fig. 8 ACCS wall panel test to BS 476 Part 21

4.4   Durability and Long Term Performance

Well designed Advanced Composite building structures such as ACCS can be expected to have low maintenance costs because of the inherent excellent durability of the materials. They are resistant to UV deterioration, moisture ingress and chemical attack because of the high glass content, careful manufacture and choice of resin. The technological advances made by those developing ACCS over the last ten years has led to a quality of manufacture and accuracy of fit that has previously been unavailable in the building industry. This enables water tightness and integrity to be achieved consistently with new modular forms of construction.

4.5   Environmental Considerations

There is a worldwide realisation of the damage that a rapidly rising energy-consuming population can do to the ecology and environmental balance of the planet. There is general agreement that future technology developments will need to meet criteria such as biological sustainability, minimum use of energy and raw materials that will probably be set internationally.

Advanced composite materials are being seen to have benefits compared with traditional materials in many of these areas, particularly in their low energy consumption during manufacture, construction and subsequent building operation (4). Although there are environmental problems associated with material manufacture, particularly resins, a number of far sighted manufacturers are already improving this aspect significantly. Glass reinforced plastics require relatively low energy during manufacture compared with metal structures, have much lower thermal conductivity and are more durable.

4.6   Electrical Properties and Service Integration

Electrical 'field free' properties are inherent in an ACCS building structure which is a major advantage in an age when buildings are becoming a support framework for large complex computer networks, whether it be the office or home. The cellular structure also enables services to be channelled out of sight. There is an inherent labyrinth of service channels in the panels of a building. If a water service leaks in an unseen location there is no danger of corrosion and structural deterioration.

4.7   Acoustic Insulation

Tests have shown that attenuation of airborne noise through a standard ACCS panel is much better than simple calculations based on the weight would suggest and is typically 25dB Leq. Structural borne noise is a significant design matter because of the lightweight structure. Special floor tiles with a foam underlay, or suspended floor structures are needed where stringent noise transmission requirements are present.

4.8 Blast and Dynamic Load Resistance

The integrity and flexibility of bonded monocoque advanced composite building structures makes them uniquely resistant to bomb and other dynamic loading such as gas explosions. This has been proven in tests carried out for the use of the materials in blast walls for offshore structures (5). Advanced composites have become important materials in offshore construction over the last five years to reduce topside weights and to improve accidental blast and fire resistance. This points the way for the use of the materials in tall buildings.
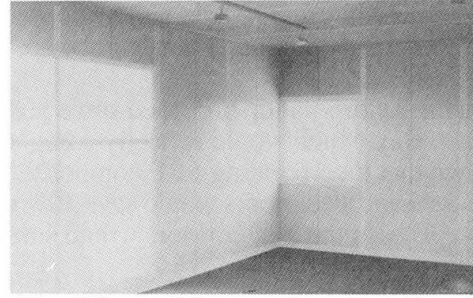

Fig. 9 Second Severn Crossing office conference room

5. Forms of Structure and Connections

A new form of building structure has been developed using ACCS in which the walls and floors are bonded together to form an integral monocoque structure (Fig 6). Vertical ACCS panels in the walls, with suitable openings for doors and windows, form the vertical box carrying members and floors span between them and act as stiffening diaphragms to the vertical box structure. Floors can be ribbed slabs or a beam and slab form if the spans are large.

Wall and floor components can be delivered flat packed and are light enough to be handled by small cranes or robots. Connections are made by bonding as described earlier and load continuity between ends of sections is achieved by bonded lapping sections, rather like bolted splice plates where bolts are replaced with adhesive. Connection integrity can be further enhanced with local *in situ* carbon fibre wrapping.

There is no reason why very tall multi-storey buildings cannot be built this way in the future. Such structures will have major advantages in earthquake prone areas and will enable a completely new approach to building safety to be achieved in these situations. Fig 9 shows the inside of an ACCS office building.

Design work carried out to date has shown that buildings up to ten storeys high can be built using the form of structure shown in Fig 6, and excellent resistance to even extreme earthquakes can be achieved. Also foundation loads are much lower and so construction on poor ground can become more attractive and cracking caused by differential settlement is eliminated.

The architectural possibilities of this form of building structure are only just beginning to be investigated. The combination of ACCS pultrusions, curved mouldings and glass provide exciting opportunities for new structural forms.
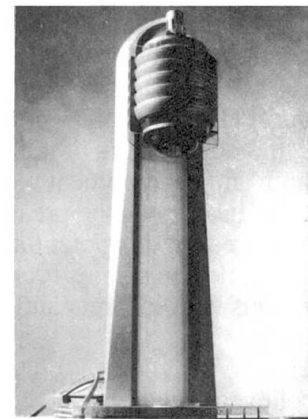
Fig. 10 Globorama Tower

Fig 10 shows a proposed tower structure called Globorama in which the top viewing platforms and entertainment centre are constructed using bonded advanced composite materials. The lightweight materials enable such new forms of structure to be considered, whereas previously with traditional materials dynamic oscillation would have been a near insoluble problem. A small mass damper is all that is needed to ensure the comfort of users at the top of the 190m high tower.

6. Extending The Limits of Tall Buildings

An important question that needs to be addressed is cost. Advanced composite materials are generally more expensive materials than steel and concrete but can form cost effective complete structures when advantages of lightness and ease of construction are fully utilised. When incorporated in taller buildings the advantages of weight reduction become greater and greater. Since even two storey buildings can be attractive from a cost point of view, when mass produced, it is certain that their use in tall buildings of

the future will grow rapidly and most particularly in earthquake prone areas. Here both vertical and horizontal acceleration effects will be accommodated more easily.

Obayashi Corporation proposed some years ago a building structure called Aeropolis 2001 (Fig 11) in Tokyo Bay which would be a city complex rising 2000m into the sky. A desk study by the author has shown that incorporating FRP composite floor systems into the 500 storeys instead of the lightweight concrete and steel floors would save 30% of the main column steel weight, a staggering 270,000 tonnes of steel. Also the lighter floors would substantially reduce the design problems under earthquake loading.

Lightweight materials can also be used to build extra storeys on top of existing buildings, thereby gaining significant additional revenue from a developer's existing land.

Building designers can also consider putting an increasing proportion of advanced composites into a building at a greater height from the ground. A building could therefore start with traditional heavy steel and concrete at ground level and move to the use of lighter advanced composite floors at the middle levels and then change to an all advanced composite bonded monocoque form at the top. This change in material could also be reflected in the architecture to bring more curved aerodynamic shapes at the higher levels, where wind speeds are greater.

Fig. 11 Aeropolis 2001

7.   Conclusions

Sophisticated design solutions are now being adopted in steel and concrete to produce cost effective tall buildings and bridges in earthquake prone areas. These include large dynamic dampers and the introduction of plastic hinges in steel beams.

More cost effective solutions may lie in the incorporation of advanced composite materials into bridge decks, the upper floors of tall buildings and in the complete structures of buildings up to ten storeys. Research and development work in the United Kingdom and the construction of a number of prototype structures has shown the great potential of these materials. Areas of research and development that are needed to realise this potential in other countries are testing for earthquake resistance and fire resistance; design studies for overall costing; national testing for compliance with Building Standards; discussions with Insurers and Statutory Authorities and production of building and construction standards.

It is believed that advanced composite materials will gain significant applications in building construction in earthquake prone areas of the world within the next 10 years.

References:

1.   Head P.R., Templeman R.B. *The Application of Limit State Design Principles to Fibre Reinforced Plastics*, British Plastics Federation RP Group Congress 1986.
2.   Lee J., Holloway L., Thorne A. and Head P.R. *Long term static testing of an FRP prototype highway structure*. Composite Structures 28 pp441-448. 1994.
3.   Cadei J.M.C., Churchman A.E. *The Design Approach for a Raw Composite Space Frame Bridge System*, IABSE Composite Construction Conventional & Innovative Conference, Innsbruck 1997
4.   Dawson D.G. *How Green is Reinforced Plastic in Construction*. British Plastics Federation RP Group Congress 1992 BPF.
5.   Churchman A.E., Cadei J.M.C. *The Development and Implementation of a Predictive Capability for Advanced Composite Materials*. Composite Materials for Offshore Use, MIMechE. London 1994

Use of I-Beams in Slim Floor Construction

S.K. GHOSH
Princ. Res. Mgr, RDCIS
Steel Authority of India Ltd
Ranchi, India

P.K. MAINI
Res. Eng., RDCIS
Steel Authority of India Ltd
Ranchi, India

D. MUKERJEE
Assist. Gen. Mgr, RDCIS
Steel Authority of India Ltd
Ranchi, India

D. KARMAKAR
Princ. Res. Eng., RDCIS
Steel Authority of India Ltd
Ranchi, India

Sanak MISHRA
Exec. Dir.
Steel Authority of India Ltd
Ranchi, India

Summary

The use of I-beam in Slim floor instead of the Universal column (UC) or Top Hat sections is the focus of this study. The investigation is limited to the design of simply supported beam under uniformly distributed load using limit state approach. The design formulation has the provision for both top and bottom flange plates. The results indicate the suitability of using such beams in Slim floor construction especially for structures subjected to heavier loads like those in warehouses, bridges etc. The cost competitiveness has also been established despite two times increase in steel consumption as compared to RCC structure.

1. Introduction

Slim floor construction is a special type of composite construction, where the beam is contained within the depth of the floor slab. The success of this type of construction using top hat sections as beam elements in Nordic countries, especially in Sweden in the last decade, has resulted in the adaptation of this type of construction in UK tailored to suit their requirement, using UC sections and bottom flange plates, supporting either the profile deck or precast slab both having concrete topping (1).

The major advantages of this type of construction lies in its ability to cover large column free areas, reduce building height, reduce overall weight of the structure, better seismic and fire resistance, faster construction, unhindered passage for service lines, elimination of the use of shuttering and props for the slab-beam system and better cost competitiveness despite increase in consumption of steel.

The work carried out till date has been limited to the use of top hat sections and UC sections. The suitability of using I-beams in place of UC section or top hat section in Slim floor construction was felt to be important as I-beams are the most commonly available beam section in developing countries. This study aims at introducing I-beams in Slim floor construction.

2.   Structural Configuration and Design

The simply supported Slim floor beam (Fig.1) considered here consists of a rolled I-beam having a bottom flange plate supporting a deep profile deck topped with concrete. The beam can also have a top flange plate to increase its efficiency and strength. The RCC topping can be either of normal weight concrete(NWC) or light weight concrete(LWC). Shear stud connectors welded to the top flange of the I-beam ensures composite action.
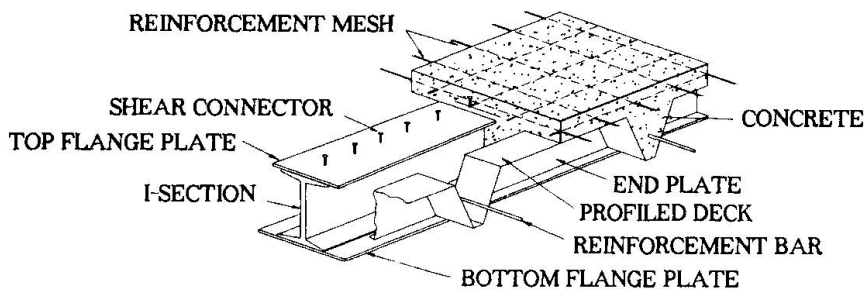
REINFORCEMENT MESH

SHEAR CONNECTOR
TOP FLANGE PLATE

I-SECTION

CONCRETE

END PLATE
PROFILED DECK
REINFORCEMENT BAR
BOTTOM FLANGE PLATE

Fig.1   Schematic View Of A Slim Floor Beam

2.1.   Basis of Design

Limit state approach has been followed for design. Factored load was used for strength design and working load for serviceability limits. In the absence of any uniform design guidelines in different countries, the provisions of the British codes (2,3) in general and those of Indian codes (4,5) in particular have been followed.

Only plastic or compact rolled beam sections in conjunction with rectangular stress block have been used for design. To ensure non-occurrence of irreversible deformations, the steel stress was limited to design stress and the concrete stress to 0.5 times the cube strength. The design steel stress may be either the yield stress or its reduced value depending on the code of practice to be followed.

2.2.   Steps in Design

In line with the sequence of construction that is followed, the design was carried out for both the construction stage and the composite stage loads.

Construction stage

The bottom flange plate was designed for biaxial state of stress caused by the deck loading and overall bending of the beam. Von-Mises Yield criteria (6) was used to obtain the moment capacity.

The combined steel section was designed considering the effect of lateral transverse buckling (LTB) caused due to the top flange being unrestrained (2).

During construction stage, the out of balance load on the beam caused by one side being fully loaded (concrete poured) results in torsion in the section. This was treated in a simplified manner by replacing these forces by equal and opposite horizontal transverse forces in the flanges in equilibrium with the torsion caused by the out of balance load.

The unity factor condition was checked for the combined stresses caused by biaxial bending. The beam was also checked for LTB in case of bending moment caused by the total construction load on the beam.

Composite stage

The effective breadth of concrete compression flange was taken as ¼ of the span but was limited to centre to centre distance of the beam. The modular ratio was taken as 10 and 15 for NWC and LWC respectively. The plastic moment capacity which depends on the degree of shear connection (assumed as 40%) was obtained in terms of the resistance of various elements of the beam by rearranging the stress diagram in a manner similar to that explained in British code (3).

Transverse reinforcement was provided to enable the concrete flange to transfer the longitudinal forces at ultimate limit state into the slab without splitting of concrete (3).

Serviceability Limit Check

All critical serviceability stresses (3) in concrete and steel were checked using cracked section properties. Deflection checks (3) were carried out for both construction stage and composite stage. Since most of these beams were quite long, the calculated natural frequency of vibration, based on the total dead load plus 10% imposed load, was limited to 4 Hz.

2.3.   Computer Programme

A programme in FORTRAN77 has been developed for the automated design of Slim floor beams having both top and bottom flange plates. The input data consists of a trial I-beam section, flange plate dimensions, span, loads and details about the profile deck and material properties. The output from the programme consists of the most optimum I-beam section, the final flange plate dimensions, number of shear connectors and the thickness of RCC topping.

3.   Results and Discussion

A few design examples with only bottom flange plate configuration have been worked out to study the various aspects of using I-beams in Slim floor construction. The I-beams and plates used have been restricted to those manufactured by Steel Authority of India Ltd.

Example 1 : A Slim floor beam for a 4.5 m x 4.5 m panel having imposed load of 6.0 kN and LWC (grade M30) topping have been designed using I-beam and compared with that using UC section as shown in Table 1. In both the cases yield strength of steel was 510 MPa, bottom flange plate thickness was 16 mm and steel decking was 210 mm deep. The smaller depth for UC section using British code can be attributed to higher distribution of material in its flanges

making it a more efficient section as compared to the I-beams. The higher load factor values as prescribed in Indian code, have led to even greater overall and section depth.

Item	British Code Load Factor		Indian Code Load Factor
	UC Section	I-Section	I-Section
Overall depth (mm)	295	310	335
Section depth (mm)	176.8	225	250

Example 2 : A comparative study of the effect of the steel strength on the size of I-beams is depicted in Fig.2. As expected, the size of I-beams decreases with the increase in the design stress of the material. Moreover, it is also noticed that as the steel strength increases, the effect
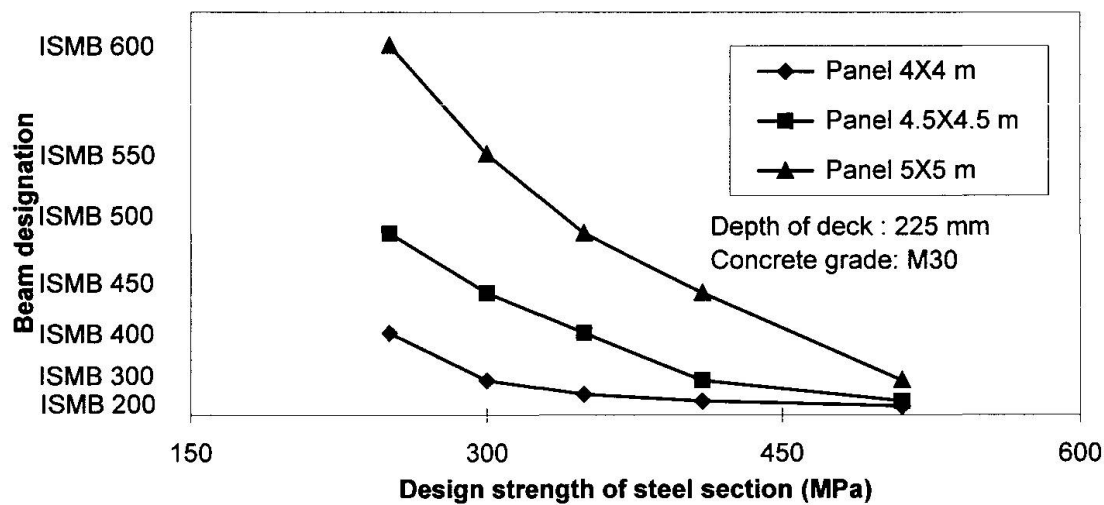
of panel dimension on the size of beam reduces in an asymptotic manner indicating greater moment capacity of beams with higher design strengths.

Example 3 : A seven storied commercial building having 400 sq.mt. area in each floor has been

Items	Type of structure			
	RCC		Slim floor	
	Quantity	Total (Rs)	Quantity	Total (Rs)
Reinforcement bars	66.53 T	11,84,378	15.95 T	2,84,052
SAIL-MA (Y S 410MPa)	-	-	86.24 T	21,99,120
IS: 513 sheet (Y S 250MPa)	-	-	45.01 T	11,20,749
Plastering wall	4018 M^2	1,86,354	2774.1 M^2	1,27,786
Plastering ceiling	2800 M^2	1,53,748	-	-
Brick work	416.15 M^3	6,10,076	344.4 M^3	5,04,890
Concreting	621.74 M^3	22,63,134	585 M^3	21,19,400
Shuttering	2800 m^2	3,39,780	-	-
False ceiling	2800 m^2	12,60,000	-	-
Interest	5 months	4,50,650	-	-
Total cost		64,48,120		63,55,997

designed as conventional RCC construction and also as Slim floor construction for cost comparison studies. Occupational and partition loads have been assumed as 4.0 kN/m^2 and 1.0 kN/m^2. The RCC design has been carried out using limit state approach (7). The cost analysis shown in Table 2 is based on the current market price in India (Rs. 38=1US $). The cost of both the structures are practically same. However, Slim floor construction has the added advantage of the building being available earlier for occupation due to faster construction and the salvage value of steel. The increase in steel consumption in case of Slim floor construction using I-beams is 2.2 times that of RCC construction as against about 4 times with UC-section (8).

Example 4 : Table 3 depicts the maximum imposed load a particular beam section can withstand for a fixed span. In all the cases the flange plate thickness was 16 mm, the grade of concrete was M30 and the yield strength of steel was 350 MPa with 210 mm deep steel decking. It is evident

Panel width (m)	Span (m)		
	4.0	5.0	6.0
	Maximum Imposed load (kN/m^2)		
4.0	22 (ISMB 225)	50 (ISMB 450)	> 50 (ISMB 550)
5.0	38 (ISMB 250)	> 50 (ISMB 500)	> 50 (ISMB 600)
6.0	40 (ISMB 350)	> 50 (ISMB 550)	--

that upto a certain span the design is governed by the construction load and is not sensitive to the imposed load.

Example 5 : Keeping in mind the requirement of reducing the dead load due to concrete, two sizes of profile decks of depth 225 mm and 290 mm were considered in the design along with I-beams in Slim floor construction. The results are presented in Table 4 for LWC which shows that after a particular panel size, the Slim floor construction with deeper deck is advantageous. Same trend has also been observed using NWC.

Panel size	225 mm Deck			290 mm Deck		
	Depth of section (mm)	Plate thickness (mm)	Overall depth (mm)	Depth of section (mm)	Plate thickness (mm)	Overall depth (mm)
3.0 m X 3.0 m	200	8	295	225	8	360
4.0 m X 4.0 m	250	12	335	250	8	360
4.5 m X 4.5 m	400	24	485	300	22	385
5.0 m X 5.0 m	500	20	585	500	10	585
5.5 m X 5.5 m	600	8	685	550	28	635

4. Conclusion

The analysis of the preceding examples brings out certain important features of Slim floor construction using I-beams .

1. It is cost competitive as compared to RCC construction.
2. The use of high strength beams for longer spans are more economical as compared to ordinary structural steel beams with yield strength of 250 kN/mm^2.
3. The ability of the Slim floor beams to support heavier imposed loads makes them suitable for use in warehouses, bridge decks etc. Conversely, for a particular imposed load condition, it is possible to cover longer span.

As the present study was restricted to simply supported beam under uniformly distributed load, it may be worthwhile to develop design and construction technique for primary and secondary beam system to cover even larger column free areas. For extending the Slim floor construction concept to bridge decks, study of dynamic behaviour of such construction needs to carried out.

Acknowledgement

References

1. Mullet, D.L., "Slim floor construction using deep decking", Steel Construction Institute, UK, 1992.
2. British Standard Institution, "BS 5950 : Structural use of steelwork in building, Part 1 : Code of practice for design in simple and continuous construction : hot rolled section", 1990.
3. British Standard Institution, "BS 5950 : Structural use of in building Part 3 Design in composite construction, Section 3 : Code of practice for design in simple and continuous composite beams", 1990.
4. Bureau of Indian Standard, "IS:800, Code of practice for general construction in steel', 1984.
5. Bureau of Indian Standard, "IS:11384, Code of practice for composite construction in structural steel and concrete", 1985.
6. Baxter Brown, J.M.C.D., "Introductory Solid Mechanics", John Wiely & Sons, 1973.
7. Bureau of Indian Standard, "IS:456, Code of practice for plain and reinforced concrete", 1978.
8. British Steel Corporation, "Publication in section, plate and commercial steel, Steel or Concrete, The Economics of Commercial Buildings".

Serviceability of Buildings Subjected to Sesmic Excitations

Anis FARAH
Prof.
Laurentian Univ.
Sudbury, ON, Canada
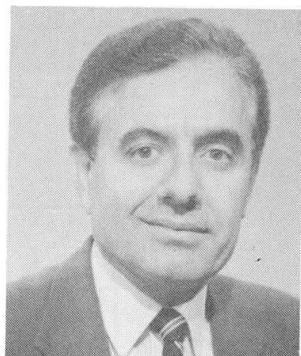
Anis Farah , born 1943, received his B.SC (Queen's, Belfast 1966), M.A.Sc (Toronto, 1967) and Ph.D (Waterloo, 1977) all degrees in civil engineering. He was Director of the School of Eng. at Laurentian Univ., and served on two committees of SCI, Deflection and Safety, and chaired the Computer Applications Committee of the Civil Eng. Div. of ASEE. He is currently a member of the ASCE Lifelines Earthquake Investigation Committee.

Summary

The response of a vibrating building, due to earthquake or wind, is greatly influenced by the soil-structure interaction. This interaction modifies the building resonant frequencies and affects its serviceability relative to the human occupant. In this paper, the serviceability is measured in terms of "human comfort" which is expressed as absorbed power(rate of energy dissipation) through a biomechanical model placed at a given floor in the building. This single value encompasses the characteristics of the structure, the soil, the human, and the dynamic excitation. The latter is represented by its power spectrum whose parameters were evaluated by using nonlinear regression on available earthquake spectra.. The results indicate that absorbed power differentiates between comfort levels at different floors, and that the damping in the structure as well as the soil foundation and power spectrum characteristics have significant impact on building serviceability.

1. Serviceability of buildings to vibration

In addition to being functional, a building must have structural integrity and be serviceable relative to the human user. The serviceability of a building in a vibrational environment has been the subject of numerous studies and recommendations, Chang and Robertson(3), and Chen(4). The recommended criteria have tended to specify acceleration, velocity or displacement limits. For example, it is generally accepted that accelerations of the order of 0.5%g-1%g are perceptible, 1%g-5%g are annoying, and >15%g are disturbing and may be intolerable. Some recommendations for residential buildings, Chang(3) also couple the amplitude of vibration with a corresponding frequency thus leading to human comfort limit curves which are a function of frequency. However, it has been shown by Farah (7) that human comfort levels can be evaluated in terms of the absorbed power through a biomechanical model. This single value incorporates the characteristics of the human, soil-structure system and the seismic excitation.

Earthquake excitation characteristics coupled with suitable site conditions can lead to a large amplification of the structural response of a building. Such a situation arose with the 1985 Mexico earthquake where resonance was set up in buildings due to the soft Tacubaya Clays near the surface of the lake bed in Mexico City, Abiss(1), resulting in extensive damage.

In this work, the seismic excitation is represented by its power spectrum, the building is modeled as a multi-degree-of-freedom system, the soil foundation is expressed in terms of translation and rocking motions resulting in 2DOF possessing mass, stiffness and damping elements, and the human is represented by a 3DOF model simulating a standing human.

2. System modeling

The computation of the building serviceability requires the modeling of the human, the building, the soil-structure interaction, and the seismic excitation.

2.1 Biomechanical model

The human body is highly sensitive to vibration, especially in the standing position. A suitable biomechanical model of a standing human in the fore and aft mode was developed by Farah(6) and is shown in Fig. 1. The parameters of the model were obtained by fitting its frequency response to available experimental data. Based on this model, the absorbed power for the thresholds of perception, annoyance and intolerance in residential buildings are 1.33×10^{-4} W, 8×10^{-4} W and 1.7W respectively. Note that there is great variation in human response to vibration among individuals, and thus the response of the

Fig.1 Three-degree model of standing man in the fore and aft mode

biomechanical model used in this work should be considered only as being a reasonable representation. The biomechanical model has three resonant frequencies, 0.58, 11.10, and 17.00 Hz. Note that the fundamental frequency lies within the range of the fundamental frequencies of tall and medium-height buildings.
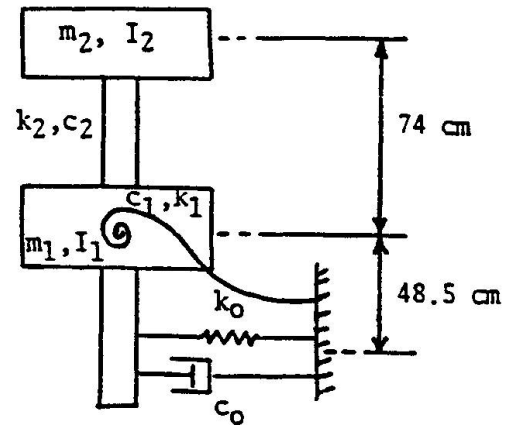
2.2 Building model

The building is represented as a multi-degree-of-freedom(MDOF) lumped-parameter system consisting of masses, springs, and viscous damping elements as shown in Fig. 2. The structure has as many degrees-of-freedom as it has stories. The mass and stiffness matrices are first determined, then empirical techniques such as Biggs' method(2) are used to generate a damping matrix for the building based on assumed critical damping ratios.
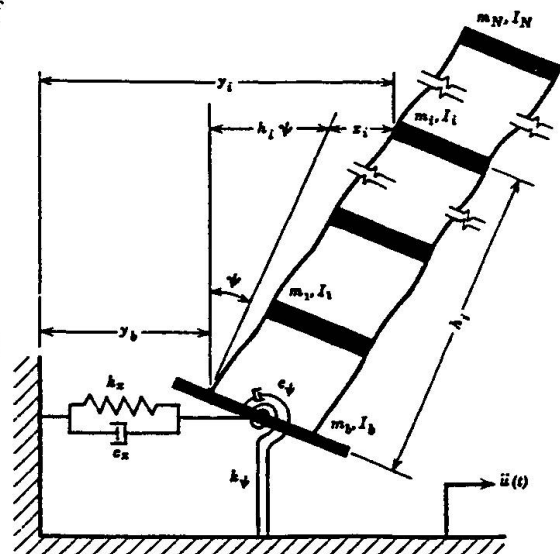

Fig.2 Configuration of flexible-base structure for horizontal seismic excitation (after Tsai)

2.3 Soil-structure interaction model

During an earthquake, the response of a building is greatly influenced by the flexibility of the soil foundation and its interaction with the structure. This interaction modifies the resonant frequencies as well as the amplitude of the structural vibrations. The soil-structure interaction impedances are represented by equivalent springs and dashpots to simulate the soil stiffness and damping. The virtual mass of the soil is calculated by a suitable formula and added to the mass of the base of the building. Generally the soil foundation characteristics are frequency dependent, however, for engineering applications these parameters can be treated as being frequency independent, Tsai(9). Only the translation and rotation(rocking) motions of the

foundation are considered in this work. This results in a soil-structure system with 2DOF greater than the number of DOF of the structure by itself. The values of the frequency-independent parameters are computed based on formulae developed with the soil being treated as an elastic half-space, Clough and Penzien(5). The soil properties involved in these calculations are the shear velocity, mass density of the soil, and the radius of the rigid disk representing the foundation half-space. The latter is usually taken as half the width of the building.

2.4 Seismic excitation model

Earthquake ground motions are usually treated as stochastic processes. While the simplest model represents ground accelerations as a white noise process with a constant power spectral density, accelerograms from earthquakes indicate that the spectral amplitudes of seismic energy are frequency dependent. Commonly used models of acceleration power spectra are those due to Kanai-Tajimi and Clough-Penzien.

Fig. 3 Acceleration power spectrum of SCT-EW 1985 Mexico earthquake (after Grigoriu et al)

The power spectra used in this study were obtained by fitting, in a least squares sense, available power spectra from the 1985 Mexico earthquake to rational functions which are capable of capturing three peaks in the power spectrum function as shown in Fig. 3.
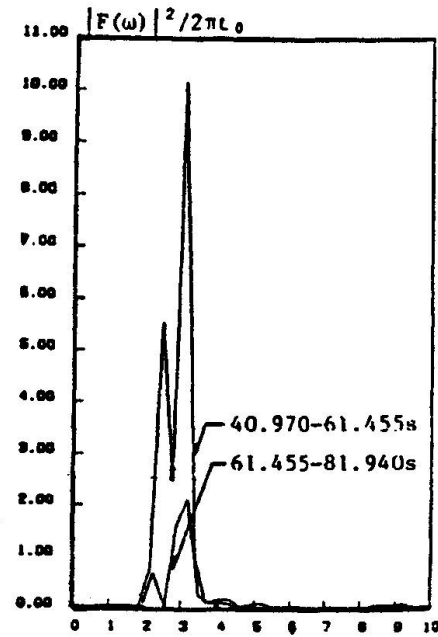
3. Equations of motion

The effect of the soil-structure interaction on the building is to change its structural response. This results from the incorporation of two additional degrees-of-freedom, horizontal translation and rotation, representing the soil foundation. This in turn increases the number of frequencies by two. Thus, there are N+2 equations of motion describing the soil-structure system response, where N refers to the number of stories in the building. The resulting equations of motion, based on Fig. 2, can be written in the following partitioned matrix form, Tsai(9):

$$\begin{bmatrix} [M] & [0] \\ \hline [0] & [m] \end{bmatrix} \{\ddot{v}\} + \begin{bmatrix} [C] & [C_1] \\ \hline [C_2] & [C_3] \end{bmatrix} \{\dot{v}\} + \begin{bmatrix} [k] & [k_1] \\ \hline [k_2] & [k_3] \end{bmatrix} \{v\} = -\ddot{u}(t) \begin{Bmatrix} \{M\} \\ m_b \\ 0 \end{Bmatrix} \quad (1)$$

where $[m] = \begin{bmatrix} m_b & 0 \\ 0 & I_s \end{bmatrix}$ with m_b being the mass of the base and I_s representing the sum of the

mass moments of inertia of the structure and the foundation; [M], [C], and [K] refer to the mass, damping, and stiffness matrices of the structure respectively, and are of size NxN; [C_1], [C_2], [C_3] and [K_1], [K_2], [K_3] are damping and stiffness matrices that couple the structure and the

flexible foundation; $\ddot{u}$ (t) is the seismic acceleration and $\{v\} = \left\{ \dfrac{\{y\}}{\dfrac{y_b}{\psi}} \right\}$.

4. Calculation of absorbed power

Absorbed power is calculated by considering the velocity and the force of interaction, between the human and the floor, at the point of contact. The force and velocity can be related to the displacement of the point of contact in the frequency domain, thus relating the biomechanical model response to that of the floor. The floor response power spectrum, $S_f(\omega)$, can be related to the seismic power spectrum, $S_a(\omega)$, by:

$$S_f(\omega) = |H(i\omega)|^2 S_a(\omega)$$
(2)

where $H(i\omega)$ is the complex frequency response function of the floor level where the biomechanical model is located. It can be shown, Farah(7) that the absorbed power, P, through the biomechanical model can be evaluated from the integral:

$$P = -\frac{1}{\pi} \int_0^\infty \omega \operatorname{Im}[G(i\omega)] S_f(\omega) d\omega$$
(3)

where $G(i\omega)$ is the complex frequency function between the force and displacement at the point of contact between the floor and the biomechanical model. The determination of $H(i\omega)$ requires that Eq. 1 be transformed to the frequency domain and the resulting matrix is inverted in closed form and $H(i\omega)$, for the various floor levels, is then obtained from the inverse matrix. The efficient inversion technique was developed by the author based on the Fadeev-Leverrier method. Note that the normal mode decomposition method cannot be used directly in this case due to the coupling terms in the damping matrix resulting from the soil-structure interaction.

4. Results and discussion

To illustrate the procedure described above, absorbed power values were calculated for the floors of an 8-story building and for various critical damping ratios. The power spectra of the seismic excitation were those of the Sept. 1985 Mexico earthquake as given by Grigoriu et al(8). The response of these buildings was evaluated for three site shear velocities 50m/s, 75m/s, and 400m/s. The shear velocity impacts the values of the damping and stiffness elements of the soil foundation. Note that both the damping and stiffness are proportional to the shear velocity and its square respectively, and that generally, the shear velocity is lower in softer soils. Fig. 4 shows that the response corresponding to the 50m/s is higher than that for the 75m/s velocity, and that the absorbed power for a given floor is larger than that corresponding to a lower floor as would be expected since higher values of absorbed power are associated with a lower comfort
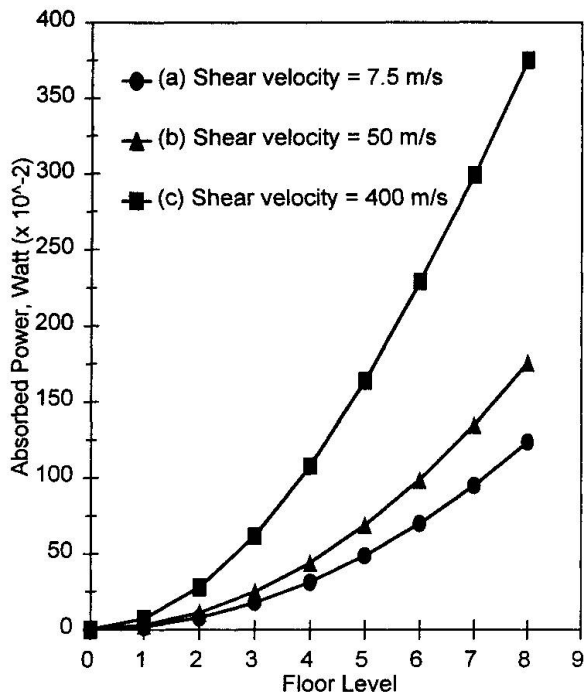
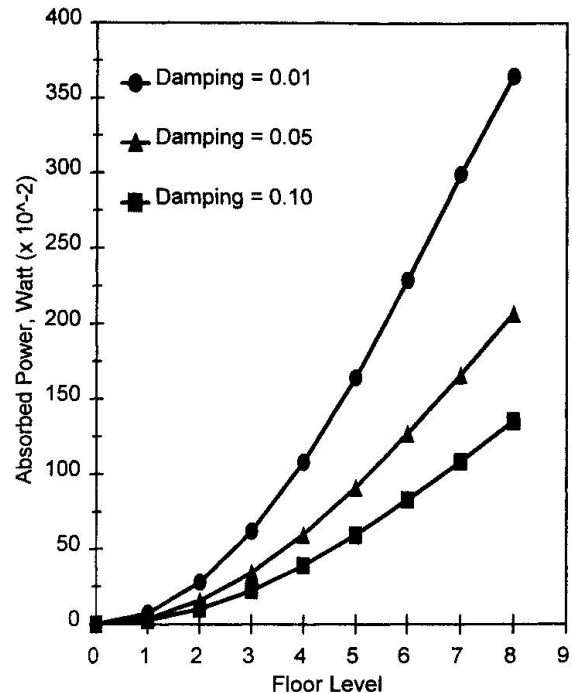Fig. 4 Absorbed power for an 8-story building with SCT power spectrum

Fig. 5 Effect of damping ratios in structure on absorbed power (shear velocity = 400 m/s)

level. In addition, the response of all floors and for all shear velocities is greater than the level required for the threshold of annoyance which is equal to 8×10^{-4} W. However, the absorbed power values for floors 6, 7 and 8 for the 400m/s shear velocity are even larger than the value of 1.7 W which corresponds to the threshold of intolerance. Such high values of absorbed power are indicative of an unacceptably severe building response such as that which occurred during the Mexico earthquake. It is also important to emphasize that for a large building response, the building behavior will not remain elastic and thus the absorbed power values would be different from those given above. The high absorbed power values for the 400m/s shear velocity were produced due to the introduction of frequencies in the soil-structure system which are very close to those of the seismic power spectrum and the first frequency of the biomechanical model. This situation arose because the fundamental frequency of the soil-structure system is 3.2r/s, that of the biomechanical model is 3.64r/s, and the dominant frequency of the earthquake power spectrum is 3.1r/s. In effect a quasi-resonance behavior was setup with the resulting large response.

The effect of the damping in the structure is very significant when the system is in a resonant vibration state. Fig. 5 shows the absorbed power in the building corresponding to a shear velocity of 400m/s. It is seen that the absorbed power on the eighth floor for a damping ratio of 0.01 results in a value of 3.75 W and the corresponding values for damping ratios of 0.05 and 0.10 are 2.07 W and 1.35 W respectively. However based on other results obtained in this study, the impact of damping in the structure is not as significant if resonant or quasi-resonant conditions are not generated.

5. Conclusions and recommendation

It has been shown that absorbed power can be a good indicator of the level of human response to building vibration subjected to seismic excitations, and has the capacity to distinguish human comfort at different floor levels. The damping in the structure is mainly important in reducing the response in a resonant or quasi-resonant vibrational environment. The properties of the soil foundation greatly influences the building behavior, with softer soils, associated with lower seismic shear velocities, generally producing higher absorbed power values except for situations where higher shear velocities generate resonant conditions. The ability to estimate the absorbed power should be invaluable to the engineer in achieving a serviceable building design.

Although this study has demonstrated the potential of absorbed power as a criterion for assessing buildings serviceability to earthquakes, further research is recommended in the following areas:

1. Development of a human model suitable for determining absorbed power under simultaneous horizontal and vertical vibration.
2. Calibration of absorbed power to various earthquake magnitudes and frequency characteristics associated with various site conditions.
3. Determination of the impact of nonlinear behavior of structures on absorbed power and therefore its serviceability.
4. Assessment of the effect of external damping devices such as viscoelastic dampers on the serviceability and safety of structures.

6. References

1. Abiss, C. P., "Seismic amplification-Mexico City", Earthquake Engineering And Structural Dynamics, vol. 18, 79-88, 1989.
2. Biggs, J. M., Introduction To Structural Dynamics, McGraw-Hill Co., 140-147, 1964.
3. Chang, F. K., "Human response to motions in tall buildings", J. Struct. Div., ASCE, ST8, 1259-1272, 1973.
4. Chen, R. W., and Robertson, L. E., "Human perception thresholds of horizontal motion", J. Struct. Div., ASCE, ST8, 1681-1695, 1972.
5. Clough, R. W., and Penzien, J., Dynamics of Structures, McGraw Hill Co., p. 591, 1975.
6. Farah, A., Serviceability of tall buildings using human perception of motion as criterion", The Third East Asia-Pacific Conf. On Struct. Engineering And Construction, vol.1, Shanghai, China, April 1991.
7. Farah, A., "Structural serviceability under dynamic loading", Deflection Of Concrete Structures, ACI, SP-86, 419-434, 1986.
8. Grigoriu, M., Ruiz, S. E., and Rosenblueth, E., "The Mexico Earthquake pf Sept. 1985-nonstationary models of seismic ground acceleration", Earthquake Spectra, vol. 4, No. 3, 1988.
9. Tsai, N. C., "Modal damping for soil-structure interaction", J. of the Engineering Mechanics Div., ASCE, April 1974.

Zarate - Brazo Largo Bridges: Stay Cable Damages and Rehabilitation

Dietrich L. HOMMEL
Chief Eng. Bridges
COWI
Copenhagen, Denmark

D. Hommel gratuated from Technical Univ. of Braunschweig, Germany, in 1966. in 1968 he joined Leonhardt, Andrä und Partner, where he during 25 years was involved in bridge designs in Germany and internationally. Since 1995 he is a member of COWI and acts presently as project manager on the Zarate-Brazo Largo bridges, a project familiar from an earlier assignment.

Michael H. FABER
Chief Eng.
COWI
Copenhagen, Denmark

M.H.Faber received his PhD. degree in Structural Reliability Theory in 1989 at the Technical Univ. of Aalborg. In 1993 M.H. Faber joined COWI where he has been working on reliability based assessment of existing structures and bridges and is presently Chief Engineer in the filed of Structural Reliability.

Summary

The paper describes the reasons and basis for a structure related design basis for rehabilitation which is using the modern load resistance factor design. This design basis is formulated such that it depends on all available information regarding the loading conditions, results from material tests, observations of the degree of deterioration and an in-depth knowledge of the structure in question. The main results of a sensitivity analysis for the roadway load model are presented and the assessment of the stay cable capacity explained.

1 Introduction

The Zárate - Brazo Largo bridges are part of a roadway and railway infrastructure project in Argentina providing a crossing of the national road No 12 over the two main branches of the Paraná river - Paraná de Las Palmas and Paraná Guazú - northwest of the river delta close to the town of Zárate. The two bridges comprise cable stayed steel girder main bridges with spans of 110-330-110 m and a total of about 16 km concrete approach viaducts for railway and roadway traffic.

The bridges were constructed during the years 1972-1977, based on an alternative bid design submitted by the Joint Venture Techint - Albano, and opened to roadway traffic in 1977 and railway traffic in 1978 - the Guazú bridge is shown in fig 1.
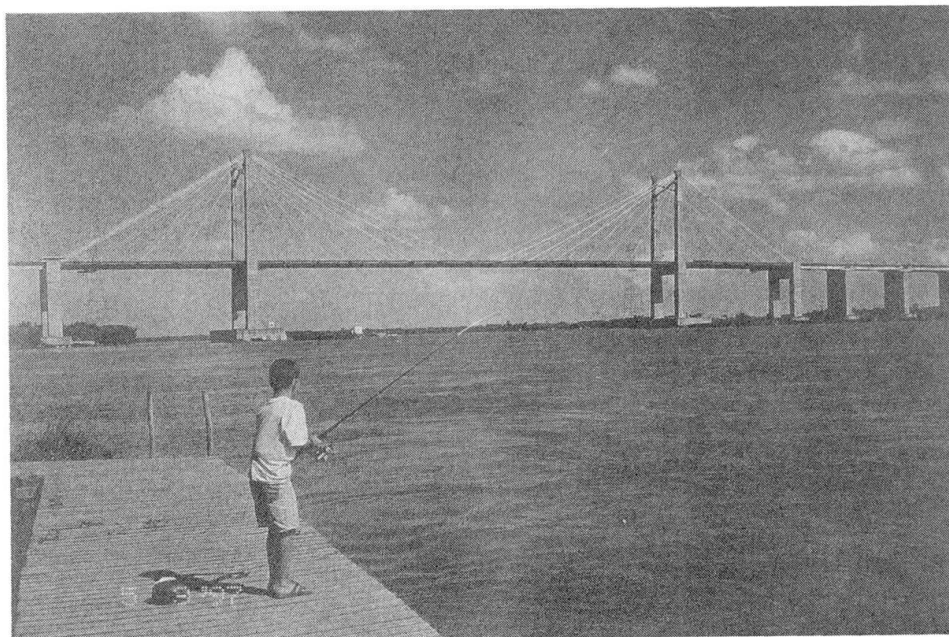
Fig. 1:   Photograph of the Guazú bridge

Since the opening of the bridges the traffic volume and traffic pattern has changed. Due to the continuous development of the mercantile requirements for transportation as well as the use of new and heavier trucks. Since Argentina entered into the Common Market of South America, the MERCOSUR, late in 1991, the national road No 12 constitutes an important part of the infrastructure on an inter-American scale and its condition is a matter of highest importance.

Stay cable 7C of the bridge across Paraná Guazú ruptured on 20 November 1996. The stay cable failed close to the bottom socket at the deck level. The cable was removed from the top anchorage and put on the bridge deck. It showed that almost all of the 121 wires Ø 7 mm failed at about 200 mm outside of the bottom socket with severe signs of corrosion and fatigue-like ruptures in the wires.

As an emergency action, the bridges were closed to traffic on 25 November 1996, and the consortium Albano - DyCASA - Freyssinet (ADF) was entrusted by Dirección Nacional de Vialidad, DNV, the national highway authority of Argentina, with the immediate replacement of stay 7C, using the Freyssinet mono strand stay type.

2 Bridge Assessment and Rehabilitation Approach

The design and assessment of ordinary structures under normal conditions is appropriately accommodated by codes of practice and regulations. This is because the codes and regulations have been formulated and calibrated specifically to ensure that the most commonly built structures under normal conditions are both economic and sufficiently safe.

For the design and assessment of structures which are unique, e.g. by proportion, concept, material or condition, codes and regulations cannot be expected to yield structures which are appropriate in terms of economy and safety. It is therefore common practice for such

structures to formulate and calibrate a design basis which is specific. Such a design basis can be understood as a specific code of practice for the design and assessment of that structure.

2.1 The rehabilitation design basis

The Zárate-Brazo Largo bridges are unique what concerns the condition of the deteriorated stays. The existing codes and regulations are thus not adequate for use as basis for a safety assessment and for rehabilitation design. Therefore, in order to ensure that the bridges are efficiently rehabilitated to a condition where they maybe accepted for safe continued use, and possibly even upgraded in terms of traffic loading, it is necessary to formulate and calibrate a rehabilitation basis specific for this bridge type, its observed state and the desired use of the bridges in the future.

To ensure the compatibility between this specific rehabilitation design basis and generally accepted design basis, such as the Eurocodes, the ISO codes and the AASTHO codes, the safety format for the rehabilitation design basis is the well-known load and resistance factor design (LRFD).

In general, the basis for the calibration of the safety factors and load combination factors is the application of modern reliability methods in accordance with the principles described in the background documents for the Eurocodes and the ISO codes, see [1].

2.2 Updating of the rehabilitation design basis

The rehabilitation design basis is formulated such that it can be modified for changes in the

* assumptions regarding past and future road and rail traffic
* results from material tests from dismantled stays
* measurements of stay forces
* inspections of damaged wires strengthening and replacement of stays.
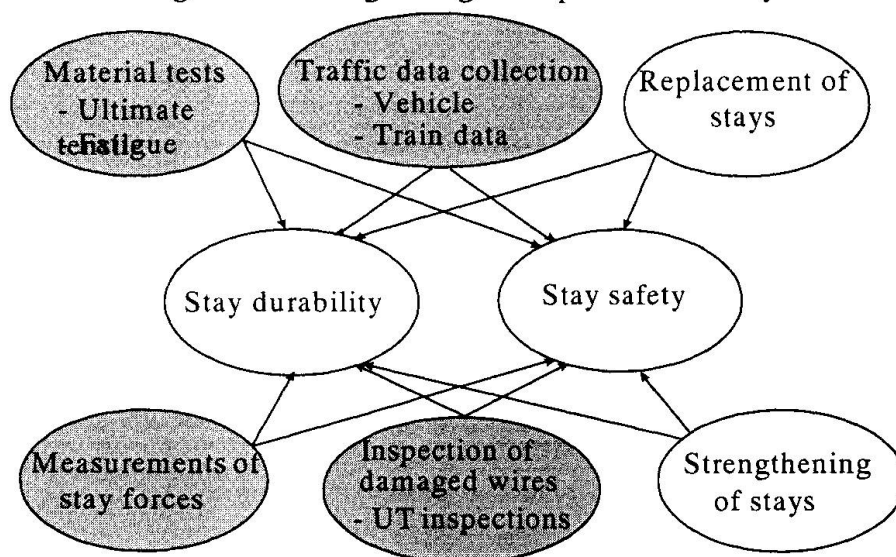

Fig. 2   *Illustration of the rehabilitation actions considered in establishing the rehabilitation design basis for the Zárate-Brazo Largo bridges.*

In fig 2 the rehabilitation actions considered for the rehabilitation of the Zárate-Brazo Largo bridges are illustrated. The grey toned "knowledge collecting" actions are those which continue changing during the course of the assessment and for which the rehabilitation design basis has been especially designed to accommodate.

The design basis for the rehabilitation of the Zárate-Brazo Largo Bridges presented in the following summarises the relevant information on loads and materials for the different stages of the rehabilitation of the bridges.

3 Roadway and Railway Loads

Probabilistic models have been formulated for the roadway and the railway loads acting on the bridges. With regard to the roadway load model basis has been taken in the theoretical framework formulated for the development of the design basis for the Great Belt East Bridge, see [2]. The railway load model has been formulated on basis of the model developed for the design of the Great Belt West bridge [3].

The roadway load model has been calibrated to the extend possible on the basis of traffic observations from the Zárate-Brazo Largo bridges. Some experience for European traffic has been used as a supplement when necessary.

The railway load model has been based on information regarding the actual traffic and traffic restrictions made available by DNV.
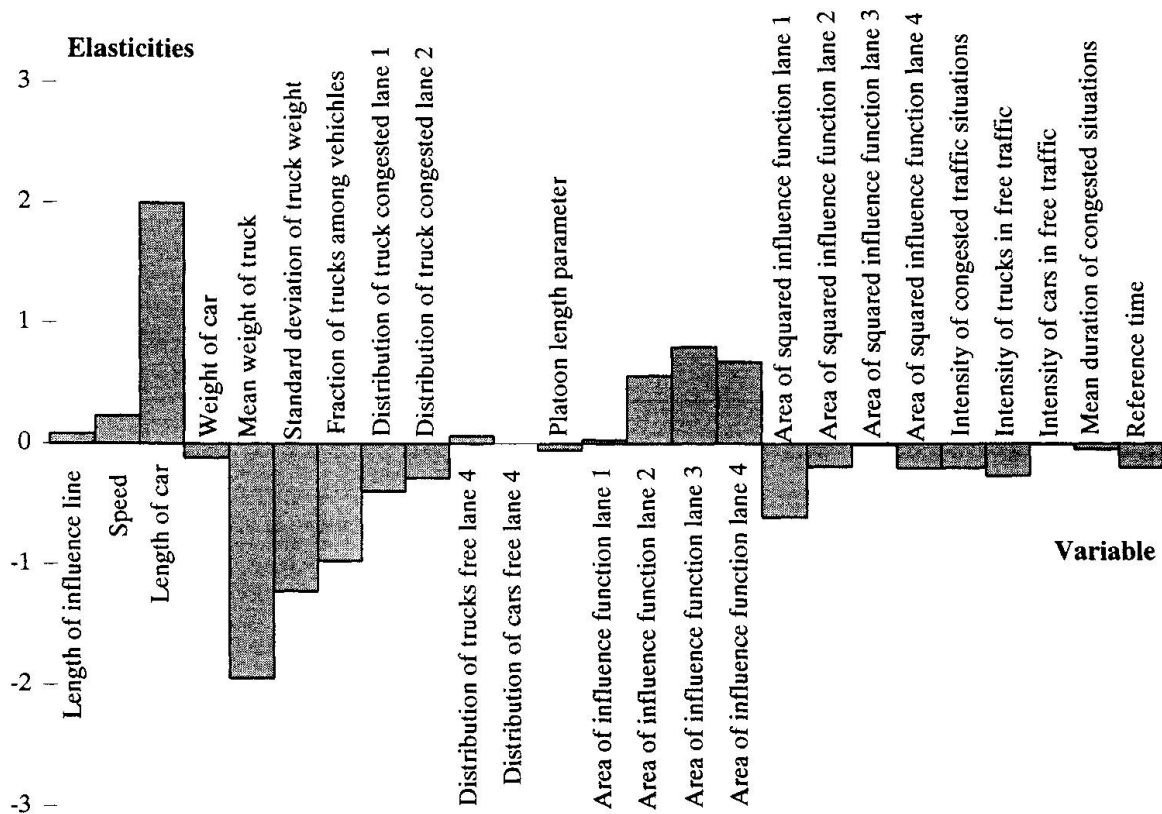

Fig. 3   Sensitivity analysis of the roadway load model.

Using the probabilistic load models together with influence lines for a number of selected load effects (including stay forces, road girder load effect and pylon load effect), the statistical distribution of the maximum load effect during one year has been determined. By defining the characteristic load as the 98 percentile of this distribution, an equivalent uniformly distributed load (EUDL) has been derived which yields the same load effect as the real load.

The results of a sensitivity analysis regarding the influence of the different input to the roadway load model is shown in fig 3.

Taking basis in the same requirements to safety as have been suggested in the back ground documents to both the Eurocodes and the ISO codes, the safety factors for the permanent and the variable loading together with the combination factors for vehicle and train loads have been derived on the basis of probabilistic principles.

4 Condition Assessment

To estimate the strength of a parallel wire cable it is necessary to determine the number of broken wires in the cable. The number of broken wires can be estimated by the use of UT-inspection. However, the UT-inspection will not be able to detect all broken wires with probability one. Furthermore, the inspection may indicate that intact wires are broken. To estimate the reliability of the inspection method it is necessary to determine the probability of detecting a wire which is broken and the probability of detecting that an intact wire is broken.

5 Assessment of Stay Cable Capacity

The resistance safety factors for the stay cables have been derived with basis in a probabilistic model of the time varying strength of parallel wire cables subject to fatigue deterioration. The model incorporates all available information regarding the material characteristics of the wires as obtained through testing under ultimate tensile as well as fatigue loading. The ultrasonic testing, together with the limited testing of cable 7C and two further cables, constitute the most essential data input to the current safety evaluation.

The model for the safety factor for the stay strength allows for a differentiation of safety factor in accordance with the intended service life of the considered stay. Furthermore the safety factors are given for the stays individually, taking specifically into account the damage condition and the loading on the individual stays.

Using the model, it is possible to derive safety factors corresponding to an interim period of the bridge (rehabilitation period) which is shorter compared to the situation where a normal service life is considered. Furthermore, the model also yields safety factors to be used in the design of stay cable replacements.

The computation of the residual life is based on a method proposed in [4]. The first step in the computation of the residual life is the estimation of the life distribution of a single wire. The number of cycles, t, to failure of a given wire subject to a stress range, Δs, is given by a Weibull distribution,

$$F_T(t, \Delta s) = 1 - \exp\left(-\left[\frac{\Delta s}{r_c}\right]^\alpha \left[\frac{t}{K}\right]^{\frac{\alpha}{m}}\right),$$

where α, m, K,

and c are unknown parameters, n is the number of sections of the test specimen with different properties and A_0 is the cross sectional area of the wire. The parameters m and K are also the parameters in the SN-curve which is given by $t = K\Delta s^{-m}$.

A large parallel wire cable with an infinite number of wires is considered. It can be shown that even though the number of wires is assumed to be infinite the results are in general valid for cables with a finite number of wires. The failure times of the intact wires given a certain level of mean stress and stress range are assumed to be identically and independently distributed. Also, the initial load on the cable is small enough to cause no static wire failure.

During service one wire breaks after the other due to accumulated fatigue damage. The wire with smallest failure time fails first in each state of the system. There is an immediate load redistribution after failure of a wire without dynamic effects during stress redistribution. The residual static strength of the individual wires is not influenced by the fatigue damage which might be accumulated. Finally, it is assumed that there is no dependency between the static strength of a given wire and the fatigue resistance of the wire.

The effect of corrosion is taken into account by determining a set of material parameters specifically for corroded wires. Further, corrosion implies that the length of wire where the material parameters can be assumed to be constant becomes small. Therefore, the parameter r_c which depends on n (the number of parts with different material parameters) depends on whether the wire is corroded.

References

[1]   H.O. Madsen, S. Krenk and N.C. Lind, *Methods of Structural Safety*, Prentice-Hall Inc., Englewood Cliffs, NJ, 1986.

[2]   H.O. Madsen and O. Ditlevsen, *Stochastic Traffic Load Modelling for the Eastern Bridge*, A/S Storebæltsforbindelsen, Review Board 3, May 1990.

[2]   H.O. Madsen, *Stochastic Train Load Modelling for the Western Bridge*, A/S Storebæltsforbindelsen, Review Board 3, May 1990.

[4]   R. Rackwitz and M.H. Faber, *Reliability of Parallel Wire Cable under Fatigue*, in: Proceedings to the ICASP 6 Conference, Mexico, 1991, Vol. 1, pp. 166-175.

Suitability of Recycled Aggregate Concrete in High-Rise Construction

K.B. PRAKASH
Assist. Prof.
T.K. Inst. of Eng & Technology
Warananagar, India

K.T. KRISHNASWAMY
Head of Dept, Applied Mech.
Walchand College of Eng.
Sangli, India

Summary

This paper presents the results of an experimental investigation carried out on the suitability of recycled aggregate concrete for the construction of high rise structures. The strength and workability of conventional natural aggregate concrete obtained from high grade cements (43 grade & 53 grade) is compared with recycled aggregate concrete obtained from high grade cements. Also, it is shown that, the shortcomings of recycled aggregate concrete in strength and workability can be overcome by the use of superplasticizers.

1. Experimental Work

In this experimental programme the strength parameters and workability of three different concretes (with different w/c ratios to cater the needs of workability) were compared. Viz -
a. concrete with conventional natural aggregates.(w/c = 0.45)
b. concrete with recycled aggregates (w/c = 0.55)
c. concrete with recycled aggregates and known dosage of superplasticizers (w/c = 0.45)

The tests were conducted on a mix of proportion 1:2:4. Zentrament Super BV superplasticizer (lignosulphonate based) was used with a dosage of 0.7%.

2. Experimantal Results

Table 1 gives the strength parameters (compressive strength, tensile strength and flexural   strength)   of different categories of concretes produced from 43 grade & 53 grade cements.

Table 2 gives the workability of different categories of concretes produced from 43 grade & 53 grade cements. The workability of 43 grade & 53 grade concretes are almost same.

Table - 1 Results of strength parameters.

Particulars of concrete	Conventional natural aggregate concrete produced from		Recycled aggregate concrete produced from		Recycled aggregate concrete with superplasticizer produced from	
	43 grade	53 grade	43 grade	53 grade	43 grade	53 grade
Comp. strength (MPa)						
7 days	16.92	19.93	12.00	13.64	22.71	24.00
28 days	18.92	22.66	16.44	18.66	24.79	32.88
2 months	29.77	35.50	28.53	32.44	32.08	36.79
Tensile strength (MPa)						
7 days	1.95	3.27	1.79	2.19	2.40	3.96
28 days	2.70	3.82	2.06	3.13	3.97	4.52
2 months	4.38	4.78	4.07	3.90	5.45	5.27
Flexural strength (MPa)						
7 days	4.64	5.36	2.96	3.76	5.04	5.96
28 days	5.40	5.80	5.04	4.04	7.00	7.44
2 months	5.84	8.52	5.24	7.36	8.92	9.36

Table 2 - Results of Workability

Particulars of Concrete	w/c ratio	Slump (mm)	C.F.	V.B. Degree (sec)	% Flow
Conventional natural aggregate concrete	0.45	0	0.87	20	4
	0.60	10	0.90	12	13
	0.70	15	0.92	6	20
	0.80	20	0.94	4	60
	0.90	Collapse	0.97	2	80
Recycled aggregate concrete	0.45	0	0.84	25	2
	0.60	0	0.86	14	9
	0.70	12	0.90	8	15
	0.80	18	0.92	7	52
	0.90	Collapse	0.95	3	71
Recycled aggregate concrete with superplasticizer	0.45	0	0.89	18	5
	0.60	8	0.93	10	14
	0.70	14	0.94	5	21
	0.80	Collapse	0.96	4	60
	0.90	Collapse	0.98	2	80

3. Conclusions

The following conclusions can be drawn -

a.   The compressive strength, tensile strength and flexural strength of conventional natural aggregate concrete is more than that of recycled aggregate concrete. But the strength of recycled aggregate concrete with superplasticizer show a distinct rise in the strength compared to the conventional natural aggregate concrete. Thus the offset in the strength properties of recycled aggregate concrete can be overcome by using a right dosage of superplasticizer.

b.   The strength properties are distinctly greater for concrete produced from 53 grade cement as compared to concrete produced from 43 grade cement.

c.   The workability is distinctly more for recycled aggregate concrete with superplasticizer.

d.   Hence recycled aggregate concrete can be effectively used in the construction of high rise buildings, especially near the vicinity where recycled aggregates are available in plenty.

Reconstruction of a Department Store Damaged in the 1995 Earthquake

Naoki UCHIDA
Assoc. Dir.
Nikken Sekkei Ltd
Osaka, Japan

Seiichi OWADA
Mgr, Structural Dept
Nikken Sekkei Ltd
Osaka, Japan

Kenzo TAGA
Senior Structural Eng.
Nikken Sekkei Ltd
Osaka, Japan

Summary

Daimaru-Kobe's Main Building had been expanded in 4-phases since 1925, and had 7 stories above ground, 1 basement (partially 2), and the total floor area of about 34,000 m². The Main Building along with its adjoining West and South Annex buildings, and the 38-ban Annex were loved by many Kobe citizens as a symbol for Kobe-Motomachi. However, the Southern Hyogo Earthquake occurred on January 17, 1995 and destroyed most of its above ground levels, and a fast restoration was keenly desired.
In spite of a reconstruction plan for the entire building, we decided to make use of most of the substructure portion, which did not suffer major damages, for restoration with shorter construction period and more economical construction cost.

1. Basic Principles of the Restoration Plan

We established the following principles, hoping this project to lead the restoration plan for the energetic and historical Motomachi streets.

1. Make a comeback by shortest possible construction period.
2. Try to work out with the least possible construction cost.
3. To seek an ideal department store prospecting future needs and necessities.
4. To restore streets integrated with historical architectures.

2. Structural Solutions

For the above 1 & 2, reduce the costly and time-consuming underground work by exploiting the external wall and foundation of the Main Building's underground portion that were luckily undamaged.
The aboveground new building was designed to be of rigid steel frame to enjoy its merit, i.e. shorter construction period. The steel frame was rooted to the underground by erecting major columns from B1 floor to ensure earthquake resisting performance of the entire building. Horizontal force will be resisted aboveground by the rigid steel frame and underground by giving sufficient net effective rigidity and strength to the 1F floor slab so that the most part of the shear force be transferred to the underground exterior walls and shear walls. What is intended here is to reduce the stress transferred from the steel column legs to the old columns and beams by decreasing the burden, upon the B1 structure, of the horizontal force from the rigid steel frame.

For the above 3., spans were reviewed. The span is to be about the double length of the existing 6- to 7-meter(approx.) spans, so that square-sales space with visibility can be created.
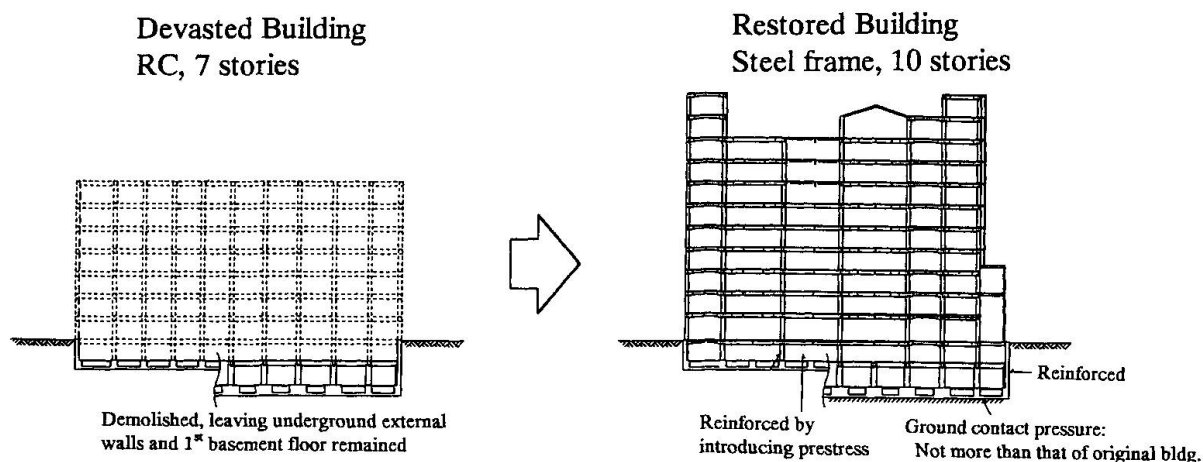
Devasted Building
RC, 7 stories

Restored Building
Steel frame, 10 stories

Demolished, leaving underground external
walls and 1st basement floor remained

Reinforced by
introducing prestress

Ground contact pressure:
Not more than that of original bldg.

Fig.1 Outline of Restoration Plan

With the enlargement of the span of the aboveground structure, the span of the foundation beams (spread foundations) had to be doubled to about 12 m. This involved the great increase of stress due to subgrade reaction. Further, it was difficult to reinforce lower sides of the foundation beams, which are in tensile zone at their ends. For this, the width of the foundation beams were increased and upper reinforcing bars were sufficiently installed to ensure ultimate strength, and then prestressing was introduced to prevent its cracking and ensure durability.

Present

Concrete to be removed

B1FL

Arrange bars at the side of foundation beam and on upper surface of the slab and place concrete.

After reinforcing

Concrete placement

B1FL

Tendon

Anchor
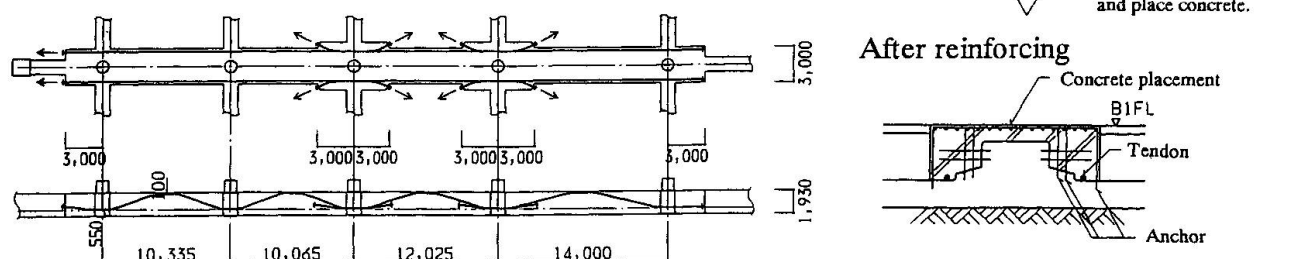
Fig.2 Reinforcement of Foundation Beam by Using Tendons

For the above 4., align the lower levels to the adjoining historical building's height, and set back the higher levels by about 5m. The purposes of these are to pay attention the continuity of the old streetscape skyline.

Setting back the building without decreasing necessary floor area requires increasing the number of floors. The new building has ten aboveground floors, exceeding the original number of seven, with the maximum subgrade reaction being about the same as of the original building by adopting steel frame structural system with light-weight-concrete of the original building.

3. Conclusion

The above mentioned solution on structural issues enabled us to realize the principles for the restoration plan, and to complete the construction works with shorter period of 6 to 8 months and construction cost reduction of about 12%, comparing to renovating the entire structure.

Daimaru-Kobe store celebrated its rebirth-grand opening on March 2, 1997, and has been receiving many customers along with a good reputation that it has been a torch for Kobe's comeback.

Coating Technology for Maintenance and Architectural Applications

Carl ANGELOFF
Sen. Technical Specialist
Bayer Corp.
Pittsburgh, PA, USA

Born in 1948, received his Civil
Engineering Degree form the
University of Pittsburgh in 1970,
and MSCE in 1976. He is currently
heads Market Dev. for North
America.

Summary

Moisture-cured polyurethane coatings are widely used in maintenance and new
construction applications because they offer durable protection. When compared with
other coatings, polyurethane systems rank among the lowest in life cycle costs.
Polyurethane coatings also provide chemical and abrasion resistance, low-temperature
curing and recoatability and surface tolerance application. Of added significance, the
solvent based formulations are commercially available to meet VOC emission limits of
2.8 lbs./gal.

Moisture-Cured Polyurethane Technology

Polyurethane moisture-cured coatings are classified as Type II urethanes under the
ASTM D-16 Specification. They are single package compositions that cure by the
reaction of residual isocyanate groups with atmospheric moisture. The reaction of these
products with atmospheric water in the field is a two stage process. The water and
isocyanate groups first produce the unstable carbamic acid, which immediately
dissociates to form an amine and carbon dioxide. The carbon dioxide evaporates from
the film, and the amine reacts with a second isocyanate group, yielding a polyurea. In a
two-component polyurethane coating, the polyisocyanate reacts with a resin having a
reactive hydrogen, which can be acrylic, polyester or polyether. The paint film resulting
from this reaction is the foundation of the performance properties of polyurethanes:
durability, corrosion and chemical resistance, and color and gloss retention. Moisture-
cured polyurethane coatings are increasing in popularity due to the wide range of
application advantages that some manufacturers are claiming:

- Can be applied on cold damp surfaces
- At temperatures below freezing
- No dew point restriction
- Adhesion to bare metal, marginally
  prepared surfaces and existing coatings

- Year round application season
- Excellent recoatability
- Single component - no mixing/measuring
- Excellent chemical resistance

Moisture-cured polyurethane coatings are applied independent of weather (temperature,
humidity and dew point), are quick drying and surface tolerant. Moisture cured surface
tolerant polyurethanes can be applied as a two coat or a three coat system using various
preparation techniques. Zinc rich primers are preferred when blast cleaning is used to
prepare the surface, varying from SSPC-SP 6 "Commercial Grade" to SSPC-SP 10 "Near
White," depending upon service conditions. In addition, moisture cured polyurethane
based primers perform well even when using lower level of zinc or zinc free

pigmentation. Coatings containing micaceous iron oxide provide excellent adhesion and durability. When overcoating tightly adhered rust remaining from hand/ power tool cleaning, it may be desirable to treat the rusted surface with a clear moisture-cured polyurethane penetrating sealer to help seal and reinforce the substrate surface.

Pigments commonly used in moisture-cured urethanes are titanium dioxide, mica, talc and micaceous iron oxide (natural or synthetic). During application of moisture-cured urethane primers and intermediate coats pigmented with micaceous iron oxide, mica and talcs, platelets align themselves more or less parallel to the substrate in closely packed layers. After the coating has cured, the overlapping pigment particles form a dense barrier against moisture and other corrosion promoters. The pigment layers also reinforce the coating, relieve stresses within the paint film and improve intercoat adhesion.

New Construction, Maintenance, and Overcoat Painting

Shop Painting: Moisture-cured polyurethane zinc rich primers are growing in use for fabrication shops due to their greater tolerance for higher film builds without mud cracking, easy touch-up in the field and they can now pass the Class B slip coefficient rating for fayed surfaces. Maintenance Painting: Both moisture-cured zinc rich primer and micaceous iron oxide and aluminum pigmented primer systems are utilized for blast cleaned surfaces. Overcoat Painting: Moisture-cured polyurethane coatings are very popular for overcoat application because of their excellent adhesion to marginally prepared surfaces, rust and existing coats. They are very tolerant of job side conditions that include low temperature variation and surface moisture.

TEST	APPLIED OVER NEAR WHITE BLASTED STEEL (SSPC-SP 10)	
	Zinc Rich Moisture Cured Urethane Primer/MIOX Filled Intermediate Coat/Moisture Cured Urethane Aliphatic Topcoat	Moisture Cured Urethane Primer with MIOX and Aluminum/MIOX Filled Intermediate Coat/Moisture Cured Urethane Aliphatic Topcoat
Salt Spray ASTM B-117 (8000 hours)	Moderate rust and 1/8" creepage and few medium blisters at score line	Moderate rust, scattered medium blisters and 1/8" creepage at score line
Prohesion (8000 hours) 1 hour wet, 1 hour dry	Moderate rust, medium dense blisters and 1/8" creepage at score line	Moderate rust, dense medium blisters and 1/8" creepage at score line
Humidity Chamber (7000 hours)	No Effect	No Effect
Chemical Resistance (250 hours) 37% HCl 50% H_2SO_4 10% CH_3COOH 50% NaOH	No Effect No Effect No Effect No Effect	No Effect No Effect No Effect No Effect
TEST	APPLIED OVER MARGINALLY PREPARED STEEL	
	Moisture Cured Urethane Primer with MIOX and Aluminum/MIOX Filled Intermediate Coat/Moisture Cured Urethane Aliphatic Topcoat	
Salt Spray ASTM B-117 (6000 hours)	Moderate rust, dense medium blister formation around score line and 1/8" creepage at score line	
Prohesion (6000 hours) 1 hour wet, 1 hour dry	Heavy rust, medium to large dense blister formation around score line	
Chemical Resistance (250 hours)	Same as above	
TEST	APPLIED OVER MARGINALLY PREPARED STEEL	
	Moisture Cured Urethane Penetrating Sealer/MIOX Filled Intermediate Coat/Moisture cured Urethane Aliphatic Topcoat	
Salt Spray ASTM B-117 (2800 hours)	Slight rust along score line, 1/16" creepage at score line	
Prohesion (1500 hours) 1 hour wet, 1 hour dry	Slight rust and 1/16" creepage at score line	

Figure 1. Performance Tests for Moisture Cured Polyurethane Systems

Working Session

Assessment by Analysis and Experiment

Papers and Poster

Leere Seite

Blank page

Page vide

Three-Dimensional Response Spectrum Analysis for Multicomponent Seismic Excitation

Ioannis E. AVRAMIDIS
Prof.
Aristotle Univ. of Thessaloniki
Thessaloniki, Greece

Kyriakos ANASTASSIADIS
Prof.
Aristotle Univ. of Thessaloniki
Thessaloniki, Greece

Summary

Within the framework of response spectrum analysis, a general solution for the three-component orthotropic seismic excitation problem is presented. The contributions from three different orthogonal earthquake components are combined in a rational manner to the maximum and minimum values of any structure response quantity. The critical orientation of the seismic input associated with these values is also determined. The method incorporates in its formulation the Penzien-Watabe model of ground motion. Therefore, in contrast to the SRSS rule, it can explicitly account for the correlation of the three seismic components, which makes it particularly usefull in the dynamic analysis of curved bridges. All given relations are easy to implement in current standard dynamic analysis software.

1. Introduction

According to the model of Penzien and Watabe [1], the three translational seismic motion components on a specific point of the ground are statistically uncorrelated along a well-defined orthogonal system of axes whose orientation remains reasonably stable over time during the strong motion phase of an earthquake. This system of principal axes of the ground motion is oriented such that the major principal axis "p" is horizontal and directed towards the epicenter, the intermediate principal axis "w" is in the transverse (orthogonal) direction, and the minor principal axis "v" is vertical (The choosen notation shall remind of Penzien-Watabe model). This orthotropic ground motion is described by three generally independent response spectra S^a, S^b and S^c, with $S^a > S^b > S^c$.

In the special case of equal horizontal components $S^a = S^b$, the extreme values of the structure's response quantities do not depend on the direction "a" of the epicentral seismic component [2,3]. However, in the general case of $S^a > S^b$, the extreme value of a response quantity strongly depends on this direction. Therefore, the determination of the most unfavorable (critical) epicentral direction for each response quantity is of great practical interest. Smeby and Der Kiureghian [4] determined the critical direction in case of analogous response spectra $S^a = \gamma S^b$, where $0 <= \gamma <= 1$. Also, Anastassiadis [3] and Lopez and Torres [5] determined the critical direction for the more general case of arbitrary response spectra.

In this paper, on the basis of the Penzien-Watabe idealization, the tensorial properties of the extreme values of response are presented. The critical epicentral direction as well as the correspondent maximum and minimum values of an arbitrary response quantity can be straightforwardly deduced from these properties.

2. Notation

A fixed global orthogonal reference system Oxyz is used for the structure. The spectra S^a or S^b are applied individually in the direction of the x- or y-axis according to Figure 1. The corresponding peak probable values of a typical response quantity R (force or displacement) are symbolized as $R_{,xa}$, $R_{,xb}$, $R_{,ya}$ and $R_{,yb}$ (Figure 1a,b,c,d), where the first subscript refers to motion in direction x or y and the second (a or b) to the input earthquake spectrum (S^a or S^b). $R_{,x}$ and $R_{,y}$ symbolize the extreme values of a typical response quantity R produced from a bidirectional excitation with epicentral direction along the axis x or y respectively (Figure 1e,f). An analogous notation is used for the variable system of principal axes Opwv.
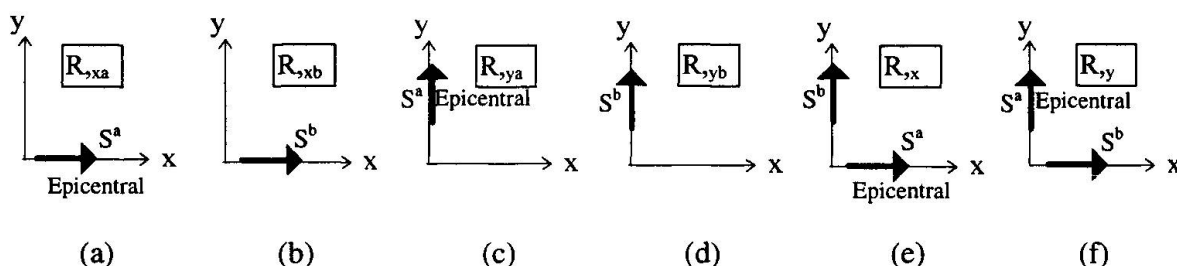
Figure 1. Response parameter notation

3. Tensorial properties - Critical direction

We assume that the epicentral principal axis p of the ground motion is defined in terms of an angle θ relative to the x axis of the fixed reference system of the structure (Figure 2). If S^a is the design spectrum in the direction of p axis and S^b the design spectrum in the direction of w axis, the probable extreme value of a response quantity R is [6] :
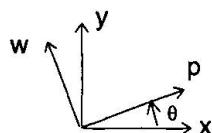
Figure 2. Definition of angle θ

$$R_{,p}^2 = R_{,pa}^2 + R_{,wb}^2 = \sum_i \sum_j \varepsilon_{i,j} \left(R_{i,pa} R_{j,pa} + R_{i,wb} R_{j,wb} \right) \tag{1a}$$

In the above expression, $\varepsilon_{i,j}$ denotes the correlation coefficient between the responses in modes i and j, and $R_{i,pa}$ and $R_{i,wb}$ denote the modal values of quantity R for the excitations defined by the indices after comma. If S^b is the design spectrum in the direction of p axis and S^a the design spectrum in the direction of w axis, we obtain the probable extreme value

$$R_{,w}^2 = R_{,pb}^2 + R_{,wa}^2 = \sum_i \sum_j \varepsilon_{i,j} \left(R_{i,pb} R_{j,pb} + R_{i,wa} R_{j,wa} \right) \tag{1b}$$

and the correlation term

$$R_{pw} = R_{pw,a} - R_{pw,b} = \sum_i \sum_j \epsilon_{i,j} \ (\ R_{i,pa} R_{j,wa} - R_{i,pb} R_{j,wb}\ ) \tag{1c}$$

The modal values $R_{i,p}$ and $R_{i,w}$ are connected to the modal values $R_{i,x}$ and $R_{i,y}$ through the following relations, which are independent of the used earthquake spectrum S^a or S^b :

$$R_{i,p} = + R_{i,x} \cos\theta + R_{i,y} \sin\theta \tag{2a}$$

$$R_{i,w} = - R_{i,x} \sin\theta + R_{i,y} \cos\theta \tag{2b}$$

Inserting these relations in the right-hand terms of (1) we obtain

$$R_{,p}^2 = R_{,x}^2 \cos^2\theta + R_{,y}^2 \sin^2\theta + R_{xy} \sin2\theta \tag{3a}$$

$$R_{,w}^2 = R_{,x}^2 \sin^2\theta + R_{,y}^2 \cos^2\theta - R_{xy} \sin2\theta \tag{3b}$$

$$R_{pw} = - (\tfrac{1}{2}) (R_{,x}^2 - R_{,y}^2) \sin2\theta + R_{xy} \cos2\theta \quad , \tag{3c}$$

where

$$R_{,x}^2 = R_{,xa}^2 + R_{,yb}^2 = \sum_i \sum_j \epsilon_{i,j} \ (\ R_{i,xa} R_{j,xa} + R_{i,yb} R_{j,yb}\ ) \tag{4a}$$

$$R_{,y}^2 = R_{,xb}^2 + R_{,ya}^2 = \sum_i \sum_j \epsilon_{i,j} \ (\ R_{i,xb} R_{j,xb} + R_{i,ya} R_{j,ya}\ ) \tag{4b}$$

$$R_{xy} = R_{xy,a} - R_{xy,b} = \sum_i \sum_j \epsilon_{i,j} \ (\ R_{i,xa} R_{j,ya} - R_{i,xb} R_{j,yb}\ ) \tag{4c}$$

It is important to note that relations (3) are similar to the transformation rules for the components of a symmetric second order tensor. Consequently, the four quantities $R_{,x}^2$, $R_{,y}^2$ and $R_{xy} = R_{yx}$ can be considered as components of a symmetric second order tensor, expressed analytically by matrices

$$\begin{bmatrix} R_{,x}^2 & R_{xy} \\ R_{yx} & R_{,y}^2 \end{bmatrix} \quad \text{and} \quad \begin{bmatrix} R_{,p}^2 & R_{pw} \\ R_{wp} & R_{,w}^2 \end{bmatrix}$$

in the Oxy and Opw reference system respectively. Due to its tensorial character, the arbitrary response quantity R is characterized by the following properties which are common to all symmetric second order tensors :

(a) The trace and the determinant of the above matrices are not dependent on the orientation of the earthquake excitation :

$$R_{,x}^2 + R_{,y}^2 = R_{,p}^2 + R_{,w}^2 \quad \text{and} \quad R_{,x}^2 R_{,y}^2 - R_{xy}^2 = R_{,p}^2 R_{,w}^2 - R_{pw}^2$$

(b) There is a specific earthquake orientation defined by the axes (I, II) for which the correlation term R_{pw} vanishes. This specific orientation is determined by the critical angle (see eq. 3c) :

$$\theta_{cr} = (\tfrac{1}{2}) \tan^{-1}(2R_{xy}/(R_{,x}^2 - R_{,y}^2)) \tag{5}$$

The corresponding response quantity R takes the following maximum and minimum values :

$$\max R^2 = R_{,I}^2 = (R_{,x}^2 + R_{,y}^2)/2 + \sqrt{[(R_{,x}^2 - R_{,y}^2)/2]^2 + R_{xy}^2} \tag{6a}$$

$$\min R^2 = R_{,II}^2 = (R_{,x}^2 + R_{,y}^2)/2 - \sqrt{[(R_{,x}^2 - R_{,y}^2)/2]^2 + R_{xy}^2} \tag{6b}$$

(c) The correlation term R_{pw} takes its maximum value

$$\max R_{pw} = R_{12} = (\tfrac{1}{2})(R_{,I}^2 - R_{,II}^2)$$

for a seismic excitation along axes (1,2) defined by the angle bisecting the axes (I, II). For these seismic directions, a response quantity R takes the value

$$R_{,1}^2 = R_{,2}^2 = (\tfrac{1}{2})(R_{,I}^2 + R_{,II}^2)$$

i.e., the interchange of the input design spectra S^a and S^b along the axes 1 and 2 does not affect the peak value of R.

It is clear from the preceding considerations that the calculation of the maximum and minimum values of an arbitrary response quantity requires four independent dynamic analyses of the structure, applying input spectra S^a and S^b as shown in Figures 1a to 1d. All necessary terms, e.g., the modal values in the right-hand sides of equations (4), are routinely calculated by current standard linear dynamic analysis programs. Then, using (4), $R_{,x}^2$, $R_{,y}^2$ and R_{xy} can be computed, and from (6a,b) the maximum and minimum values of any response quantity R can be immediately obtained, with no need to previously calculating the critical angle θ. Finally, the contribution of the vertical seismic component is to be added to the above values, according the SRSS combination rule. It is obvious that all mentioned relations can be easily implemented in current standard software for multicomponent seismic analysis.

4. Conclusions

A general solution for the three-component orthotropic seismic excitation problem is presented. It offers, within the framework of response spectrum analysis, a rational procedure for determining the maximum and minimum values of any given response quantity R of a structure. It also provides a simple means of determining the critical orientation θ associated with the extreme values of R. In contrast to the SRSS rule prescribed by many design codes, the presented method can explicitly account for the correlation of the different seismic components by incorporating in its formulation the Penzien-Watabe model of ground motion. This fact makes it particularly usefull in the dynamic analysis of curved bridges. All necessary relations are of a computationally simple form and can be easily implemented in current standard dynamic analysis software.

References

[1] Penzien, J. and Watabe, M., Characteristics of 3-D Earthquake Ground Motions, Earthquake Engineering and Structural Dynamics, 1975, 3, 365-373.

[2] Anastassiadis, K. and Avramidis, I.E., Unfavourable directions of seismic excitation for multistorey buildings (in greek), in Proc. of the 1st Greek Conf. on Earthq. Eng. and Eng. Seismology, 252-263, March 1992, Athens.

[3] Anastassiadis, K., Directions sismiques défavorables et combinaisons défavorables des efforts, Annales de l' I.T.B.T.P., 1993, no.512, 83-97.

[4] Smeby, W. And Der Kiuregian, A., Modal combination rules for multicomponent earthquake excitation, Earthquake Engineering and Structural Dynamics, 1985, 13, 1-12.

[5] Lopez, O.A. and Torres, R., Determination of maximum structural response to two horizontal motion components applied along any arbitrary directions for application to building codes, XI World Conference Earthquake Engineering, Acapulco, paper No. 619, Mexico, June 1996.

[6] Der Kiureghian, A., A response spectrum method for random vibration analysis of MDF systems, Earthquake Engineering and Structural Dynamics, 1985, 9, 419-435.

Leere Seite

Blank page

Page vide

Small Strain Non-Linear Relations for 3D Space Beam Systems

Milan VASEK
Assoc. Prof.
Czech Techn. Univ.
Praha, Czech Republic

Milan Vasek, born 1941, received his civil
eng. degree from the Czech Techn. Univ.
Prague and PhD in 1974. He is currently
teaching at the Czech Techn. Univ. and
working as consulting and forensic eng.
He was as visiting Prof. at Mie Univ. in
Japan 1991 and Fulbright scholar at
Pittsburgh Univ. in USA in 1995.

Summary

This contribution is dedicated to the improvement of the geometric non-linear solution of 3D
beam space structural system based on a finite element approach. The improved relations are
based on all terms of the energy expression for the axial deformation. The energy due to the
deformation caused by St.Venant torsion of 3D-beam element is taken into the account for the
geometric non-linear behavicr of the 3D element. The influence of each component of a joint
deflection on the others within the non-linear solution of the element is clearly separated. The
effect of the elastically constrained members is included in relations. The new cross sectional
properties of the 3D beam are presented.

1. Introduction

Geometric non-linear behavior of space structures is investigated by many researchers. The
classical approach is dealing with the geometric stiffness matrix k_G. The nodal forces are given by
the well known equation (1) from [1].

$$S= (k_E + k_G) U \qquad (1)$$

where S is the vector of nodal forces of the element, U is the vector of the nodal displacements,
k_E is the elastic stiffness matrix and k_G is the geometric stiffness matrix.

The point of interest on the influence of semirigid connections together with the non-linear
behavior of structure is described in [2], [3], [4], [5], [6]. Space structural frameworks are inten-
sively used since 1980's. Papers dealing with these problems are published in proceedings on
Space structures [4], [5]. At the work [9] are derived relations for the semirigid connections with
respect to the all twelve degrees of freedom in the space. The solution which is based on the
equation (1) is omitting higher order terms of the beam energy due to axial deformation. The
concept of a geometric stiffness matrix is based on the simplification that the load imposed onto
the structure is unchanged, during the load step increment. The relations which are introduced in
this paper are not using any simplification and all the terms in the energy expression are used. As
result of the approach leads to a clearly separated relations for each component of the deflection.
The other effect of the approach is that the relations are more accurate then the previous equation
(1). The detail derivation and the solution procedure is described in [6], [7], [8]. It is   also

possible to introduce the effect of the semirigid connections as were derived by Toader at [9]. The derived results are corresponding to the relations for the plane frame structures in [10].

2. Non linear relations

2. 1 Basic Assumptions

The derivation is based on the following assumptions:
1) 3D members are straight without any imperfections
2) The local coordinate system of the member follows the right hand rule and is coincident with major principal axis of the member
3) Navier's hypothesis is valid for the cross-section of the member.
4) Torsion is assumed to be Saint Venant type, i. g. warping is neglected.
5) The load step increment is finite
6) The loads are acting on joints
7) The structural material is elastic-perfectly plastic
8) Local stability effects do not occur

2.2. The basic relations of geometric non-linear behavior

The relation between the nodal displacements and element deformations is described by
$$u \ (x, y, z) = a \ U \ (u_1,u_2,u_3,......u_n) \tag{2}$$
where u is the vector of the element deformations and U is the vector of nodal displacements. Matrix a is the matrix of functions describing the geometrical relations between these displacements. Non-dimensional coordinates are introduced as $\xi = \frac{x}{L}, \zeta = \frac{y}{L}, \eta = \frac{z}{L}$, where x, y, z are dimensions in local coordinate system and L is the length of the 3D element (Fig. 1)
The deformed length of an infinitesimally small element (Fig.2) can be expressed as
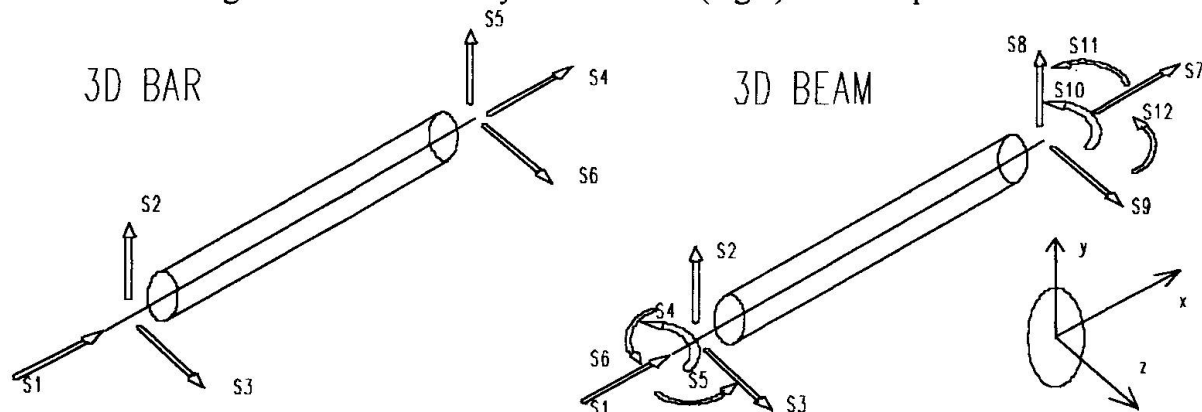
Fig. 1: The 3D bar and beam member

$(1+\varepsilon_x^a)dx$ where the ε_x^a is the engineering axial strain and dx is the elements length. Applying Pythagora's theorem, the elongation of the element may be expressed as

$$[(1 + \tfrac{a}{x})dx]^2 = \left(dx + \frac{\partial u}{\partial x}dx\right)^2 + \left(\frac{\partial v}{\partial x}dx\right)^2 + \left(\frac{\partial w}{\partial x}dx\right)^2 \tag{3}$$

This can be simplified as:

$$\varepsilon_x\left(1 + \frac{\varepsilon_x}{2}\right) = \frac{\partial u}{\partial x} + \frac{1}{2}\left(\frac{\partial u}{\partial x}\right)^2 + \frac{1}{2}\left(\frac{\partial v}{\partial x}\right)^2 + \frac{1}{2}\left(\frac{\partial w}{\partial x}\right)^2 \tag{4}$$

The right hand side of equation (4) represents the component of the Green strain tensor e_{xx}. For the condition of small strain, we can write $(\varepsilon_x{}^a)^2 = 0$ and the Green tensor coincides with the engineering strain ε_x. If we introduce terms for the axial deformation due to bending to the expression (4) we receive

Fig.2: The beam element

$$\varepsilon_x = \frac{\partial u}{\partial x} + \frac{1}{2}\left(\frac{\partial v}{\partial x}\right)^2 + \frac{1}{2}\left(\frac{\partial w}{\partial x}\right)^2 - y\frac{\partial^2 u_y}{\partial x^2} - z\frac{\partial^2 u_z}{\partial x^2} \tag{5}$$

The energy of the member due to the axial deformation (5) can be expressed by equation (6)

$$U = \tfrac{1}{2}E\int_V \varepsilon^2 dV \tag{6}$$

The whole axial energy expression is expressed as:

$$U = \frac{E}{2}\int_0^L \oint_A \left\{\left(\frac{\partial u_x}{\partial x}\right)^2 + \left(\frac{\partial^2 u_y}{\partial x^2}\right)^2 y^2 + \left(\frac{\partial^2 u_z}{\partial x^2}\right)^2 z^2 + \frac{1}{4}\left(\frac{\partial u_x}{\partial x}\right)^4 + \frac{1}{4}\left(\frac{\partial u_z}{\partial x}\right)^4 + \frac{\partial u_x}{\partial x}\left(\frac{\partial^2 u_y}{\partial x^2}\right)^2 + \frac{\partial u_x}{\partial x}\left(\frac{\partial^2 u_z}{\partial x^2}\right)^2 \right.$$

$$-2\frac{\partial u_x}{\partial x}\frac{\partial^2 u_y}{\partial x^2}y - 2\frac{\partial u_x}{\partial x}\frac{\partial^2 u_{zy}}{\partial x^2}z + \frac{1}{2}\left(\frac{\partial u_y}{\partial x}\right)^2 - \left(\frac{\partial u_y}{\partial x}\right)^2\left(\frac{\partial^2 u_y}{\partial x^2}\right)y - \left(\frac{\partial u_y}{\partial x}\right)^2\left(\frac{\partial^2 u_z}{\partial x^2}\right)z - \frac{\partial^2 u_y}{\partial x^2}\left(\frac{\partial u_z}{\partial x}\right)^2 y$$

$$\left. -\left(\frac{\partial u_z}{\partial x}\right)^2\left(\frac{\partial^2 u_z}{\partial x^2}\right)z + \frac{\partial^2 u_y}{\partial x^2}y\frac{\partial^2 u_z}{\partial x^2}z\right\}dAdx \tag{7}$$

Let's express the deflection vector u in the form of nodal displacements using the equation (2) and perform the integration of the equation (7). After that, Castigliano's theorem (part 1) can be applied to the expression (7) with respect to the deflections $u_1, u_2, \ldots\ldots u_{12}$. We obtain the relations for the nodal forces $S_1, S_2, \ldots\ldots S_6$ for the 3D bar and $S_1, S_2, \ldots\ldots S_{12}$ for the 3D beam. To express results in the matrix form we have to introduce new cross sectional properties to express torsional moments S_4 and S_{10}. These terms are written as

$$K_y = \oint_A z^4 dA, \qquad K_z = \oint_A y^4 dA, \qquad K_{zy} = \oint_A z^2 y^2 dA, \tag{8}$$

We can call these expressions "moments of inertia of second order". Another feature of the approach is that each nodal force is dependent on a symmetrical square matrix which includes terms composed only from the cross-sectional properties and constants. The non-linear influence of the other nodal displacements are excluded from the geometric nonlinear stiffness matrices. Therefore it is possible to separate the influences of different nodal displacements on the observed nodal force. This approach leads to the expression for each force which relies on the 6x6 matrices for the 3D bar element or 12 x 12 matrices for the 3D beam element.

2.3 The Non-linear solution for 3D members with the separate effects of deflections

The general equation for the forces at the end nodes of a 3D bar element is as follows:

$$S_i = k_{Ei} \, U + (U^T \, h_i \, U) + u_j \, (U^T \, q \, U) + u_j \, (U^T \, g \, U) \tag{9}$$

where index j relies on the index i of the evaluated force as $j=i+3$ for $i=2,3$ and
$j=i-3$ for $i=5,6$

u_i, u_j .... nodal displacements (scalar quantities) which have the major effect   on
the corresponding   force S_i

k_{Ei} .... i-th row of the elastic stiffness matrix,

h_i .... square 6x6 matrices, which express the loading change during the load
step (corresponds to   the well known geometrical stiffness matrix k_G)

U.............. 6x1 vector of node displacements

U^T............. transpose of vector U

q, g ....square 6x6 matrices which express the higher terms of order in the longitudinal
strain energy of a bar

The expression results for a 3D beam element are more complicated. The derivation procedure is similar to that of a 3D bar element. The general equation for nodal forces applied to a 3D beam, which represent shear, axial force and bending, is

$$S_i = k_{Ei} \, U + (U^T \, {}^7h_i \, U) + (U^T \, {}^1h_i \, U) \tag{10}$$

$$+ u_i \, (U^T \, {}^i e1 \, U) + u_{i+6} \, (U^T \, {}^{i+6}e2 \, U) + u_j \, (U^T \, {}^j e3 \, U) + u_{j+6} \, (U^T \, {}^{j+6}e4 \, U)$$

where ${}^7h_i = -{}^1h_i$ are square 12x12 matrices which express the loading change during the loading step (corresponds to,   the well known, geometrical stiffness matrix k_G).   Superscript 7 or 1 express the influence of $7th$ or $1st$ node deflection as a major influence

k_{Ei} .... corresponding row of the elastic stiffness matrix

U.......................... 12x1 vector of nodal displacements

${}^i e1, {}^{i+6}e2, {}^j e3, {}^{j+6}e4$ .. square 12x12 matrices which express the influence of higher order
terms in the axial strain energy expression of a 3D beam element

$u_i, u_j, u_{i+6}, u_{j+6}$......... the node displacements (scalar quantities), which have a major
influence on the corresponding force S_L where index i is 2 and index j
is 6 for the forces S_2, S_8, S_6, S_{12}, index i is 3 and index j is 5 for the
forces S_3, S_9, S_5, S_{11},

Expressions for the torsional moments S_4, S_{10} are slightly different. These forces represent Saint Venant's torsion. The matrix equation for the nodal torsional moment is as follows:

$$S_i = k_{Ei} \, U + (U^T \, {}^7h_i \, U) + (U^T \, {}^1h_i \, U) + u_i \, (U^T \, {}^i g1 \, U) + u_{i+6} \, (U^T \, {}^{i+6}g2 \, U) \tag{11}$$

where index i is either 4 or 10.

Matrices $g1$ and $g2$ for the torsional moment S_4, at the near   end of the element include   the same terms as matrices $g1$ and $g2$ for the   torsional moment S_{10},   at the far   end of the beam element, except they are of an opposite sign. The basic difference between   the expressions for bending moments and shear forces is in the non-linear influence of   the governing deflection u_i which is separated out of the matrix equation as a factor. The torsional moments are influenced only by the torsional deflection u_4 and u_{10}. Then the equation (10) or (11) can be expressed in a form

$$S = S_E + S_G + S_Q \tag{12}$$

Forces S_G which corresponds to the forces which were calculated with the geometric stiffness matrix k_G are   now divided into two parts $(U^T \, {}^7h_i \, U)$ and $(U^T \, {}^1h_i \, U)$. The first part $(U^T \, {}^7h_i \, U)$ express the influence of the deflections at the far end of the element to the solved nodal force S_i.

The second part $(\mathbf{U}^T\ ^1\mathbf{h}_i\ \mathbf{U})$ express the influence of the deflections at the near end of the element to the solved nodal force S_i. For the force S_1 the matrix $^1\mathbf{h}_1 = \mathbf{0}$. Similarly for the force S_7 the matrix $^7\mathbf{h}_7 = \mathbf{0}$. For the force S_1 and S_7 are matrices $^7\mathbf{h}_1 = -\ ^1\mathbf{h}_7$ and the terms remind in the geometrically stiffness matrix $\mathbf{k}_G$. Thus, the effect of the geometric non-linear behavior expressed by the approximate formula using the geometric stiffness matrix is good for axial force, but the other non-linear influences to the shear forces and bending and the torsional moments are not taken into the account in the equation (1).

Matrices $^i\mathbf{e1}$, $^i\mathbf{e2}$, $^i\mathbf{e3}$, $^i\mathbf{e4}$ for shear forces S_2 and S_8, and similarly for S_3 and S_9, include the same terms, however they are negative for $^i\mathbf{e1}$, $^i\mathbf{e2}$, $^i\mathbf{e3}$, $^i\mathbf{e4}$ for the forces S_8 and S_9 at the far end of the element. The same is true for the torsional moments S_4 and S_{10}. Therefore, only matrices $^i\mathbf{e1}$, $^i\mathbf{e2}$, $^i\mathbf{e3}$, $^i\mathbf{e4}$ need to be written to express the forces S_2 and force S_3. The matrices $^i\mathbf{e1}$, $^i\mathbf{e2}$, $^i\mathbf{e3}$, $^i\mathbf{e4}$ for the bending moments vary in a position and value of non zero elements. The following are matrix expressions showing the non linear relations between internal forces and deflections with respect to the governing deflections which are as factors out of the matrices.

The elastic matrix $\mathbf{k}_{Ei}$ in this expression can be submitted by the matrix with the influence of semirigid connections as was derived in [13]. We can therefore solve the member forces with respect to the non-linear behavior with included semirigid connections. The coefficients for the connections can be established either by experiments or by FEM calculation of a joint with respect to the material non-linear behavior. The simple iteration procedure described at the example at [6] could be applied for the solution.

2.4 The effect of the shear torsional energy

The influence on the geometrically non linear behavior due to the shear energy should be also included in the expression for the energy of the element. In the space framework the forces at any joint are distributed to the bending and the torsional moments. Also the torsional energy should be taken into the account. The space frame members are usually made from tubes. The Saint Venant torsion express properly the behavior of the member. Several basic assumptions are as folows. With respect to these assumptions the cross sections of the beam are not deformed, they are only rotated against each other under the Saint Venant torsion. For the position at axis x, e.g. $z_0 = 0$, $y_0 = 0$ we can write

$$\frac{\partial u_x}{\partial y} = 0, \frac{\partial u_x}{\partial z} = 0 \qquad \gamma_{zy} = 0 \qquad \frac{\partial u_x}{\partial y_0} = \frac{\partial u_x}{\partial z_0} = 0 \tag{13}$$

We can now write the expression for the rest of the shear stress tensor as follows

$$\gamma_{xy} = \frac{\partial u_y}{\partial x} + \frac{\partial u_z}{\partial x}\cdot\frac{\partial u_z}{\partial y} \qquad \gamma_{xz} = \frac{\partial u_z}{\partial x} + \frac{\partial u_y}{\partial x}\cdot\frac{\partial u_y}{\partial z} \tag{14}$$

Energy of the deformed beam due to the shear deflections can be expressed at equation (15)

$$U = \frac{G}{2}\int\limits_L\int\limits_A\left[\left(\frac{\partial u_y}{\partial x}\right)^2 + \left(\frac{\partial u_z}{\partial x}\right)^2 + \left(\frac{\partial u_z}{\partial x}\cdot\frac{\partial u_z}{\partial y}\right)^2 + \left(\frac{\partial u_y}{\partial x}\cdot\frac{\partial u_y}{\partial z}\right)^2 + 2\left(\frac{\partial u_y}{\partial x}\right)\left(\frac{\partial u_z}{\partial x}\cdot\frac{\partial u_z}{\partial y}\right) + 2\left(\frac{\partial u_z}{\partial x}\right)\left(\frac{\partial u_y}{\partial x}\cdot\frac{\partial u_y}{\partial z}\right)\right]dx\,dA \tag{15}$$

After the same procedure which was shown and explained above, we will receive matrix expression for the nodal forces with respect to the energy spent for the shear deformation due to the Saint Venant torsion. The values of terms in the matrices are similar to the values at the stiffness matrix with respect to the axial deformation. For the materials with relatively large shear modulus is therefore reasonable to include the effect to the analysis. Final matrix equation for the nodal forces is different for the forces due to the shear and bending and different for the forces due to

the torsion S_4, and S_{10}. This fact is similar as at the previous equations (10) and (11). We can write for the first group of the forces the equation (16)

$$S = \frac{GA}{2} \{ e\ U + \tfrac{1}{3} e\ U\ U^T\ c\ U \} \tag{16}$$

and for the torsional forces we have

$$S_4 = \frac{GA}{2}\ ^4d\ U\ U^T\ r\ U, \qquad S_{10} = \frac{GA}{2}\ ^{10}d\ U\ U^T\ r\ U, \tag{17}$$

These expressions can be added to the equation (12) and solved simultaneously. The orthogonal transformation from the local to the global system can be used to express the non-linear expression for the whole system.

Conclusion

The derived equations allow to obtain geometric non-linear solution of an arbitrary 3D beam system with the possibility to solve effect of each deflection component separately. The accuracy of the solution can be easily controlled according to which matrices are used. The stability of large one-layer systems is highly effected by the real rigidity of nodes, which can be partially plastified. The derived equations allow to solve 3D system with respect to the non-linear behavior with the effect of the semirigid connection. The evaluation of the effect of each deflection to the non-linear behavior of system is assume to be done with respect to different topology of space systems.

References

[1] J.S. Przemieniecki, Theory of Matrix Structural Analysis, Mc Graw Hill, (1968)

[2] Y. Goto and W. F. Chen, Second- Order Elastic Analysis for Frame Design, J. of Struct. Eng. ASCE, Vol. 113, 7, July, 1501-1529, (1987)

[3] J.Y. Richard Liew and W. F. Chen, Stability Design of Semirigid Frames, John Willey & Sons Inc., New York, (1996)

[4] H. Nooshin , Third International Conference on Space Structures, Elsevier Ap plied Science Publishers, London, New York, (1984)

[5] G. A. R. Parke and C. M. Howard, Space Structures 4 th Conference Proceedings on Space Structures , Thomas Telford Services Ltd. London , (1993)

[6] M. Vasek, Solution of Bars or Beams with repect to Geometrical Nonlinearity, Stavebnicky časopis VEDA, Vol.24, 5, 415- 428, Vyd. Slovenskej Akademie Vied, Bratislava, (1975)

[7] M. Vasek, The Non-linear Behaviour of Large Space Bar and Beam Structures, G.A.R. Parke and C.M.Howard, Space Structures 4 th Conference Proceedings on Space Structures , 665-674, Thomas Telford Services Ltd. London, (1993)

[8] M. Vasek, M. Drdacky, K. Hoblik, Research Report of the Czech Grant Office no. 103/93/2027 , Space   Roof Structural System, Pittsburgh, Prague, (1996)

[9] I. H.J. Toader, Stability functions for Members with Semirigid Joint Connections, J. of Struct. Eng., Vol.119, 2, February, ASCE, 505-521, (1993)

[10] M.A.M.Torkamani, M.Sonmez, J.Cao,Second-Order Elastic Plane-Frame Analysis Using Finite Element Method,J. of Struct. Eng., Vol.123, 9 , Sept, ASCE, (1997)

The Finite Strip Method in Computational Engineering

Dragan D. MILASINOVIC
Assoc. Dean
Faculty of Civil Eng.
Subotica, Yugoslavia

Dragan D. Milasinovic, born 1954, received his Civil Eng. degree from the Univ. of Sarajevo in 1978 and Ph.D. in 1987. He is currently a faculty member at the Univ. of Novi Sad where he is an Assoc. Prof. of Plates and Shells Theory.

Summary

In the last two decades the Finite Strip Method (FSM) has been successfully introduced in the studies of linear behavior, vibrations and buckling as well as nonlinear behavior of various types of prismatic folded plates and curved shells. The reason for the introduction of this method lies in the fact that resolving of several classes of practical problems it is much faster than the more comprehensive and adaptable Method of Finite Elements (FEM). This is generally valid for structures with regular geometrical shape and simple boundary conditions, whose discretization into many finite elements is often very expensive. In such cases the FSM can be extremely competitive in terms of cost and accuracy, both during calculations and in practical application. Discretization of the cross-section into a mesh of finite strips enables the adoption of a finite number of degrees of freedom in the section.

1. The Finite Strip Variational Formulation

The well-known basic procedure of the method is the discretization of plate structures into longitudinal strip elements. The general form of the finite strip displacement function is approximated by the product of polynomes and series which is an interpolation between the classical Ritz and the FEM,

$$f = \sum_{m=1}^{r} Y_m(y) \cdot \sum_{k=1}^{c} N_k(x) \cdot q_{km} \qquad (1)$$

where $Y_m(y)$ are functions from the Ritz and $N_k(x)$ are interpolation functions from the FEM. According to the Green-Lagrange's strain tensor, we present the strain components in an arbitrary point, on the distance z from the middle plane of the plate, as functions of the displacement components of the point of the middle plane of the plate (u_0, v_0, $w=w_0$), as follows:

$$\varepsilon_x = u_{o,x} + \frac{1}{2}\left(u_{o,x}^2 + w_{,x}^2\right) - z \cdot w_{,xx},$$

$$\varepsilon_y = v_{o,y} + \frac{1}{2}\left(u_{o,y}^2 + w_{,y}^2\right) - z \cdot w_{,yy}, \qquad (2)$$

$$\gamma_{xy} = u_{o,y} + v_{o,x} + u_{o,y} \cdot u_{o,x} + w_{,x} \cdot w_{,y} - 2 \cdot z \cdot w_{,xy}$$
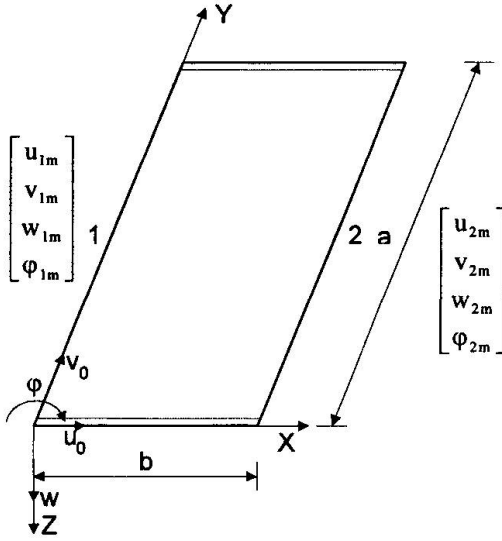
Fig. 1 A finite strip with eight degrees of freedom

The previous expressions can be obtained as products of the following matrices and vectors:

$$\mathbf{e}_o = \mathbf{L}_1 \mathbf{A}_u \cdot \mathbf{q}_u = \mathbf{B}_{u1} \cdot \mathbf{q}_u$$

$$\eta_o = \frac{1}{2}\mathbf{L}_1 \tilde{\mathbf{A}}_w \cdot \mathbf{W} \cdot \mathbf{L}_2 \mathbf{A}_w \cdot \mathbf{q}_w = \frac{1}{2}\mathbf{B}_{w1} \cdot \mathbf{W} \cdot \mathbf{B}_{w2} \cdot \mathbf{q}_w$$

$$\xi_o = \frac{1}{2}\mathbf{L}_1 \tilde{\mathbf{A}}_u^u \cdot \mathbf{U} \cdot \mathbf{L}_2 \mathbf{A}_u^u \cdot \mathbf{q}_u^u = \frac{1}{2}\mathbf{B}_{u1}^u \cdot \mathbf{U} \cdot \mathbf{B}_{u2}^u \cdot \mathbf{q}_u^u$$

$$\kappa = \mathbf{L}_3 \mathbf{A}_w \cdot \mathbf{q}_w = \mathbf{B}_{w3} \cdot \mathbf{q}_w$$

$$\mathbf{e}_o^I = \mathbf{L}_4 \mathbf{A}_u^u \cdot \mathbf{q}_u^u = \mathbf{B}_{u4}^u \cdot \mathbf{q}_u^u$$

$$\mathbf{e}_o^{II} = \mathbf{L}_5 \mathbf{A}_u^v \cdot \mathbf{q}_u^v = \mathbf{B}_{u5}^v \cdot \mathbf{q}_u^v$$

(3)

Where:

$$\mathbf{e}_o = \begin{bmatrix} u_{o,x} \\ v_{o,y} \\ u_{o,y}+v_{o,x} \end{bmatrix}, \quad \mathbf{e}_o^I = \begin{bmatrix} u_{o,x} \\ 0 \\ u_{o,y} \end{bmatrix}, \quad \mathbf{e}_o^{II} = \begin{bmatrix} 0 \\ v_{o,y} \\ v_{o,x} \end{bmatrix},$$

$$\eta_o = \begin{bmatrix} \frac{1}{2}w_{,x}^2 \\ \frac{1}{2}w_{,y}^2 \\ w_{,x}\cdot w_{,y} \end{bmatrix}, \quad \xi_o = \begin{bmatrix} \frac{1}{2}u_{o,x}^2 \\ \frac{1}{2}u_{o,y}^2 \\ u_{o,x}\cdot u_{o,y} \end{bmatrix}, \quad \kappa = \begin{bmatrix} -w_{,xx} \\ -w_{,yy} \\ -2w_{,xy} \end{bmatrix},$$

$$\mathbf{L}_1 = \begin{bmatrix} \dfrac{\partial}{\partial x} & 0 \\ 0 & \dfrac{\partial}{\partial y} \\ \dfrac{\partial}{\partial y} & \dfrac{\partial}{\partial x} \end{bmatrix}, \quad \mathbf{L}_2 = \begin{bmatrix} \dfrac{\partial}{\partial x} \\ \dfrac{\partial}{\partial y} \end{bmatrix}, \quad \mathbf{L}_3 = \begin{bmatrix} -\dfrac{\partial^2}{\partial x^2} \\ -\dfrac{\partial^2}{\partial y^2} \\ -2\dfrac{\partial^2}{\partial x\partial y} \end{bmatrix},$$

(4)

$$\mathbf{L}_4 = \begin{bmatrix} \dfrac{\partial}{\partial x} \\ 0 \\ \dfrac{\partial}{\partial y} \end{bmatrix}, \quad \mathbf{L}_5 = \begin{bmatrix} 0 \\ \dfrac{\partial}{\partial y} \\ \dfrac{\partial}{\partial x} \end{bmatrix},$$

$$\mathbf{A}_u = \begin{bmatrix} \mathbf{A}_u^u & 0 \\ 0 & \mathbf{A}_u^v \end{bmatrix}, \quad \mathbf{q}_u = \begin{bmatrix} \mathbf{q}_u^u \\ \mathbf{q}_u^v \end{bmatrix}, \quad \tilde{\mathbf{A}}_w = \begin{bmatrix} \mathbf{A}_w & 0 \\ 0 & \mathbf{A}_w \end{bmatrix},$$

$$\mathbf{W} = \begin{bmatrix} \mathbf{q}_w & 0 \\ 0 & \mathbf{q}_w \end{bmatrix}, \quad \tilde{\mathbf{A}}_u^u = \begin{bmatrix} \mathbf{A}_u^u & 0 \\ 0 & \mathbf{A}_u^u \end{bmatrix}, \quad \mathbf{U} = \begin{bmatrix} \mathbf{q}_u^u & 0 \\ 0 & \mathbf{q}_u^u \end{bmatrix}.$$

The total potential energy is defined as the sum of the potential energy of external forces and the strain energy. The formulation of strip characteristics will be presented using the principle of minimum total potential energy.

1.1 Geometrically Nonlinear Viscoelastic Problems

In the non-homogeneous finite strip composed of the layers of concrete and reinforcement, the conditions of balance represent a system of geometrically nonlinear equations.

$$\left[\hat{\mathbf{K}}(t) + \tilde{\mathbf{K}}(t)\right] \cdot \mathbf{q}(t) = \mathbf{D}_o(t) \cdot \left[\hat{\mathbf{K}}(t_o) + \tilde{\mathbf{K}}(t_o)\right] \cdot \mathbf{q}(t_o) + \mathbf{Q},$$

(5)

where $\hat{\mathbf{K}}$ is the classical or basic stiffness matrix, $\tilde{\mathbf{K}}$ the geometrical stiffness matrix.

1.2 Geometrically Nonlinear Elastic Problems

As the instant strains are elastic Eq. (5) can be written in the form:

$$\left[\hat{K}(t_o)+\tilde{K}(t_o)\right]\cdot q(t_o) = Q_o. \qquad (6)$$

This is a system of non-linear simultaneous equations at time t=t₀.

1.3 Linear Elastic Problems

By exclusion of the geometrical stiffness matrix from the above equation we obtain a linear system of differential equation.

$$\hat{K}(t_0)\cdot q(t_0) = Q_0. \qquad (7)$$

1.4 Linear Viscoelastic Problems

The behavior of the material, which changes with time, can be approximation by the following equations of balance

$$\hat{K}(t)\cdot q(t) = D_0(t)\cdot Q_0 + Q \qquad (8)$$

which is a system of linear simultaneous equations, which enclose time dependent effects.

The basic stiffness matrix blocks, together with the geometrical stiffness matrix blocks are used in this interactive analysis:

$$\hat{K}(t) = \begin{bmatrix} \hat{K}_{uu} & \frac{1}{2}\hat{K}_{uw} \\ \frac{1}{2}\hat{K}_{wu} & \hat{K}_{ww} \end{bmatrix},$$

$$\tilde{K}(t) = \begin{bmatrix} 0 & \frac{1}{4}\tilde{K}_{uw} \\ \hline \frac{1}{2}\tilde{K}_{wu} & \frac{1}{2}\tilde{K}_{ww}+ \\ & \frac{3}{4}\tilde{K}^{\cdot}{}_{ww}+ \\ & \frac{3}{4}\tilde{K}^{\cdot\cdot}{}_{ww} \end{bmatrix} + \begin{bmatrix} 0 & \frac{1}{4}\tilde{K}^{u}_{uw}+ \\ & \frac{1}{2}\tilde{K}^{u\cdot}_{uw} \\ \hline \frac{1}{4}\tilde{K}^{u}_{wu}+ & 0 \\ \frac{1}{4}\tilde{K}^{u\cdot}_{wu} & \end{bmatrix} +$$

$$+ \begin{bmatrix} \frac{1}{2}\tilde{K}^{uu}_{uu}+ & \\ \frac{3}{4}\tilde{K}^{uu\cdot}_{uu}+ & \frac{1}{2}\tilde{K}^{uv}_{uu} \\ \frac{3}{4}\tilde{K}^{uu\cdot\cdot}_{uu} & \\ \hline \frac{1}{4}\tilde{K}^{vu}_{uu} & 0 \end{bmatrix} \qquad (9)$$

Since the system of equations is nonlinear, the equations of balance in any step of the iterative procedure resolving will not be satisfied. Due to this fact, we shall have the vector of non-balanced forces, i.e., residual loading. It is favorable to present this vector separately for the linear and nonlinear part.

$$R = \hat{R}+\tilde{R}-Q, \qquad (10)$$

Q is the load vector and q the vector of nodal line displacement parameters for the finite strip.

$$Q = \begin{bmatrix} Q_u \\ \hline Q_w \end{bmatrix}, q = \begin{bmatrix} q_u \\ q_w \end{bmatrix} , \qquad (11)$$

2 Newton-Raphson's iterative procedure of solution

The variational statement about stationary of the total potential energy in nonlinear problems results in a vector of non-balanced forces,

$$R = \left[\Phi_{,q^T}\right] = \left[\hat{K}+\tilde{K}\right]\cdot q - Q = 0, \qquad (12)$$

Taylor's expansion of (12) gives:

$$R_1 = R(q_0 + \delta_0) = R(q_0) + \overline{K}_0\delta_0 + \ldots = \\ R_0 + \overline{K}_0\cdot\delta_0 + \ldots \qquad (13)$$

where $\overline{K}_0 = R_{,q}$ is the second partial derivative of Φ calculated at q_0 (tangent stiffness matrix).

If (13) is zero and if only the linear terms in q_0 are considered the standard Newton-Raphson iteration is obtained:

$$\delta_0 = -\overline{K}_0^{-1}\cdot R_0. \qquad (14)$$

Using this approach, an iteration further gives:

$$\delta_n = -\overline{K}_n^{-1}\cdot R_n, \qquad (15)$$

where $\overline{K}_n = R_{,q}$ at q_n.

The criterion for convergence, based on the residual force values, is:

$$\frac{\sqrt{\sum_{i=1}^{N}\left(R_i^n\right)^2}}{\sqrt{\sum_{i=1}^{N}\left(Q_i\right)^2}}\cdot 100 \le \varepsilon \, , \qquad (16)$$

where N is the total number of nodal lines of the decomposed structure, and rt. determines the number of iteration. This criterion means that convergence occurs when the norm of residual forces becomes lesser than ε, which is assigned.

3   Examples

3.1 Example 1

This example presents a comparative analysis of calculations of a prestressed concrete element according to the theory of prestressed concrete within a line analysis, and to the FSM. The results differ considerably, due to two main reasons. First, by the FSM, as opposed to the classical calculation based on the theory of line girders, we can obtain the stress-strain state of the thin-walled bar with open and deformable cross-section. Second, in the calculation of the stress-strain state in an arbitrary time t, the Poynting-Thompson's model of viscoelastic body is used.

Figure 2 presents the cross-section of prestressed concrete element, with the length of 10.20 m.
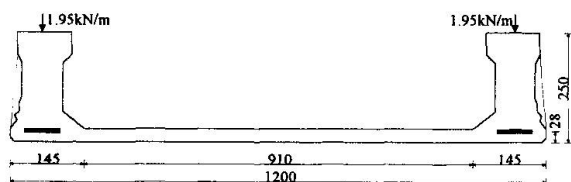
Fig. 2 Cross-section of prestressed concrete element

The element is made of C60, and it is prestressed adhesively with four cables 7ϕ5mm, with total area of 5.5 cm^2 and total initial prestresing force of 667.2 kN. The

allowed stress in steel is 128×10^4 kN/m^2, and the elasticity modulus of steel is $E_t = 2 \times 10^8$ kN/m^2.
Characteristics of concrete as a viscoelastic material are:

$E_c = E_{28} = 4.138 \cdot 10^7$ kN/m^2,

$\varphi(t_\infty, t_o) = 2.8$,

$\chi(t_\infty, t_o) = 0.75$,

$\sigma^p_{allowed} = -18500$ kN/m^2,

$\sigma^t_{allowed} = 2200$ kN/m^2.

Apart from the own weight, the element is subject to live loading which is transmitted to the longitudinal beams. This loading is considered to be movable, and it does not induce the effects of concrete creep. The loading on two beams is 3.9 kN/m. In combination with the own weight, if it is also considered as line loading, the loading on both beams is 6.0 kN/m. Figure 3. presents the mesh of finite strips with the corresponding boundary conditions.
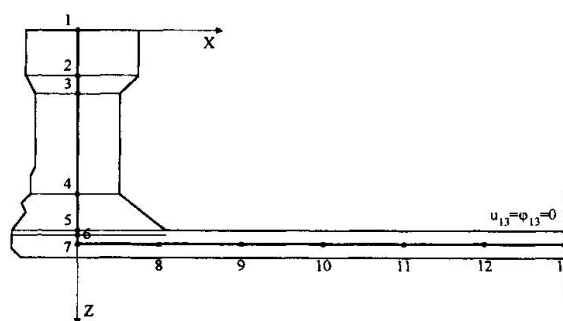
Fig. 3 Mesh of finite strips and symmetry conditions

The results of calculation are presented in Figure 4 (a), (b) and (c). In Figure 4(a) the diagram drawn in the full line represents σ_y caused by own weight and prestressing in the time t_0, while the dotted line is for the time t_∞. The stresses are calculated in the middle of the span length. Figure 4(b) presents the diagram of σ_y caused by the live loading, and Figure 4(c) of that caused by the total loading and prestressing in the time t_∞.
It can be seen that the stresses in the concrete exceed the allowed values. The line analysis, which can not yield good results for such a cross-section, gives stress values which are within the allowed limits. According to this calculation, in the upper
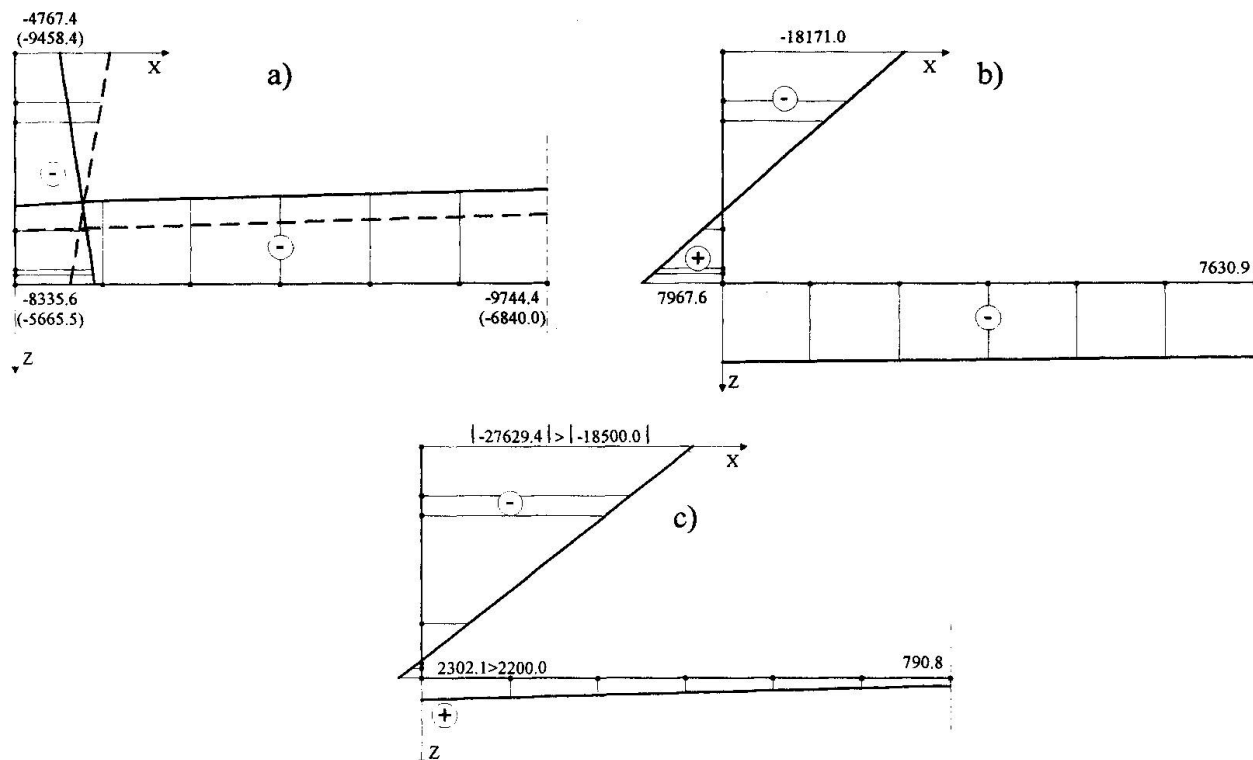
Fig. 4 Diagrams of stress σ_y in the middle of girder span length, (a) effect of own weight and prestressing in t_0 and t_∞ (b) effect of live loading, (c) effect of own weight, prestressing and live loading in t_∞

fibre $\sigma_y{}^p$ = -18310 kN/m^2, and in the lower fibre $\sigma_y{}^t$ = 616 kN/m^2.

In addition, it should be noted that according to the FSM, the loss of prestressing force caused by elastic strains of concrete (3.23%) and elastic strains and creep of concrete (6.99%) is much lesser than the total prestressing force loss anticipated in the calculation according to the line analysis (20%).

3.2 Example 2

Prefabricated prestressed concrete girders are complex elements, 75 x 210 cm, lightened by three openings ϕ50 cm. The elements are from 13.40 to 25.40 m long, see Figure 5 and they serve as bridge girders. They are made of the following materials:

- steel for prestressing 1800/16Q0, with nominal cross-section of 0.93 cm^2,
- concrete C40.

The cutting of tendons can be carried out only when the concrete reaches the strength of 30 MN/m^2. The reason for this is the

unfavorable stress state of the girder in the moment of prestressing. Here we shall
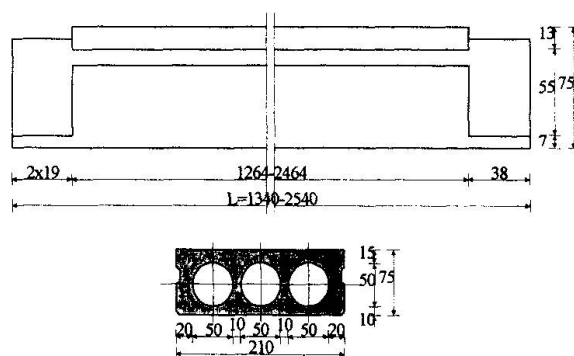
Fig. 5 View and cross-section of bridge girder

analyze a girder, which is 19.50m long, prestressed with 48 tendons with total area of 44.64 cm^2, and total initial prestressing force of 5625 kN.

The mesh of finite strips in the cross-section

of the girder is presented in Figure 6. Polyhedral shell finite strips with eight degrees of freedom were used. Eleven terms of the series were used in the calculation of own weight and prestressing.
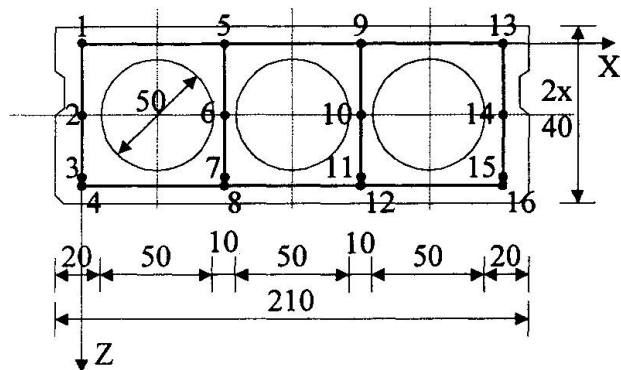
Fig. 6 Mesh of finite strips in the cross-section of girder

Figure 7 presents the most unfavorable distribution of the stress σ_y in the node lines 1 and 3. Tension stress is unfavorable for node line 1, and high stress of pressure for node line 3

displacement amplitudes. Complex mathematical expressions were programmed within the frame of the standard Newton-Raphson's iterative procedure. The application of the FSM promises more reliable results than the application of the FEM, since the errors of discretization in the former method are much lesser. Bearing in mind that the FSM is a semi-analytical and semi-numerical method, in the theory of polyhedral shells, we find it very favorable in solving of this problem.

References

1. Cheung, Y.K., "The Finite Strip Method in Structural Analysis", Oxford, Pergamon Press, 1976.
2. Loo, W.C., Causeus, A.R., "The Finite Strip Method in Bridge Engineering", Wexham Springs, Viewpoint Publications (C&CA), 1978.
3. Milašinović, D.D., "The Finite Strip Method in Computational Mechanics, Faculty of Civil Engineering: Subotica, Budapest, Belgrade, 1997

Fig. 7 Distribution of stress σ_y (kN/m²); (a) in node line 1, (b) in node line 3

5   Conclusions

A nonlinear FSM has been presented for use in the design of reinforced concrete plate structures. The procedure has advantages over the conventional FEM, since the application of numerical integration is avoided, and the stiffness matrices, loading vectors and residual forces are expressed explicitly as a function of the nodal

Strength Optimisation and Crack Resistance of RC Structures

Yuriy M. POCHTMANN
Prof.
Dnepropetrovsk State Univ.
Dnepropetrovsk, Ukraine

Yuriy M. Pochtman, born 1934, Dr
Sc, Prof. of Dept of Applied
Mathematics and Mechanics,
Dnepropetrovsk State University.
Member of New York Academy of
Sciences and IABSE.

Summary.

The calculation of strength for reinforced concrete members is at present executed pursuant to requirements [1], where for efforts each of combinations in sections, in view of position of the section relatively to longitudinal axis of member (normal, inclined, spatial) the appropriate formulas for calculation of strength are adduced. The aid [2], made in development of [1], contains the auxiliary tables oriented on «hand-operated» calculations. However such approach is badly combined with opportunities of computer simulation.

1. Optimum Formulation

At the same time, all problems of calculation of strength, submitted in [1] and [2] have sufficient generality, as follows: in each of them, at given efforts, overall dimensions of section, classes of concrete and reinforcement, it is necessary to find the minimum area of reinforcement at which the conditions of strength, as well as parametrical and structural restrictions, intended in [1], are provided. Such formulation of the problem of calculation of strength quite correspondents to the problem of nonlinear mathematical programming (NMP), as it represented, for example, in [3]:

$$\min\left\{F(\overline{x}) \middle| g_i(\overline{x}) \geq 0, i = 1,..q; h_j(x) = 0, j = 1,.., P\right\}. \tag{1}$$

Here: $\overline{x} = x_i(1,..,n)$ - n-dimensional the vector of unknown variables; $\Phi(\overline{x})$ - scalar, in general case - nonlinear functions of all several variables x_i; $g_i(\overline{x}), h_j(\overline{x})$ - scalar, in general case - nonlinear functions of all or some variables forming system of restrictions, correspondingly, in form of unequations and equations.

It is important to note that formalization of wide class of strength problems in form of optimization model [1] permits during the construction of appropriate computing algorithms to use enough general dependencies which describes stress-strained state of reinforcement and concrete in section, without additional simplifications, stipulated by the limited opportunities of «hand-operated» calculation.

This article enters the improved diagram of dependence of stress in longitudinal reinforcement σ_s from the relative depth of compressed zone of concrete ξ for bending and eccentric com-

pressed members from concrete having class B30 and below, with reinforcement of class A-I, A-II, A-III (see fig.1, curve 1). The stress σ are described by not direct but broken line in segment $\xi \in [\xi_R, 1]$ with point of inflection in { } in contrast to known simplified diagram, adduced in [4] and used in [1]. By this it is provided the better coincidence with exact formula of stress [4].

Here: $\bar{\sigma} = \dfrac{\sigma_s}{R}$ -reduced stress in reinforcement placed at extended or less compressed edge of member.

Beside it is used a single expression for determination of stresses in longitudinal reinforcement

$$\sigma_s = R_s \cdot F(\xi), \xi \in [0,1.1] \tag{2}$$

where $F(\xi)$ - function, approximated the considered diagram. The interpolation polinom of 6-th degree is applied as such function.

$$F(\xi) = a_0 + \sum_1^6 a_i \xi^i \tag{3}$$

Values of coefficients $a_i (i = 0,..,6)$ for classes of concrete B12,5 and B15 by $\gamma_{B2} = 0,9$ are calculated on computer and listed in table.

Table.

a_i	Class of Concrete	
	B12.5	B15
a_0	0.987019	0.987970
a_1	3.036522	2.868721
a_2	-36.030163	-34.394078
a_3	140.012541	135.665211
a_4	-224.673126	-222.200063
a_5	149.077017	151.287490
a_6	-33.430986	-35.232187
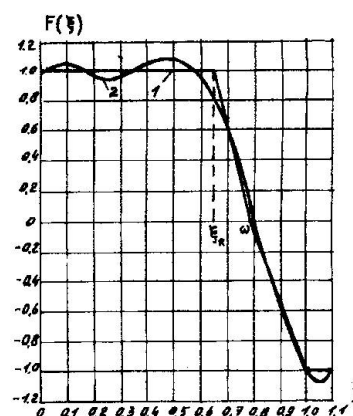
fig 1.

The diagram $F(\xi)$, having been received for concrete B15, is represented on fig.1 (curve 2). Let's consider some problems of calculations of reinforced concrete members formulating as a problem of NMP using dependencies (2) and (3). All the designations, except of specially mentioned, are accepted from [2].

2. The strength calculation for normal sections of bended members

The relative depth of compressed zone of concrete, as well as tensioned and compressed areas of reinforcement are accepted as unknown variables of the NMP problem:
$x_1 = \xi, x_2 = As, x_3 = A's$. The NMP problem accepts the following air:
Find the minimum of object-function:

$$\min \Phi(x) = x_2 + x_3 \tag{4}$$

by executing of:

 a) conditions of strength

$$x_1(1 - 0.5x_1) + \frac{x_3 R_s(h_0 - a')}{R_B bh_0^2} - \frac{M}{R_B bh_0^2} \geq 0 \tag{5}$$

 b) equation of balance

$$\frac{\left(x_2\left(a_0 + \sum_1^6 a_i x_1^i\right) - x_3\right)}{x_1} - \frac{R_B bh_0}{R_s} = 0 \tag{6}$$

 c) parametrical and structure restrictions

$$\left.\begin{array}{l} x_1 > 0, \\ x_1 < 1.1, \\ x_2 - 0.0005bh0 \geq 0, \\ x_3 \geq 0. \end{array}\right\} \tag{7}$$

Solutions of problem (4)-(7) is illustrated by control examples taken from [2].
The example 1: b=30cm; h=80cm; a=5cm; a' =3cm; concrete B15 (γ_{B2} = 0,9); reinforcement AIII; M=20.0 toneforce·m . The results (the correspondenced values from [2] are indicated in brackets):

$x_1 \equiv \xi = 0.323(0.322); \ x_2 \equiv A_s = 11.36(11.34)cm^2$

The example 2: b=30cm; h=80cm; a=5cm; a' =3cm; concrete B15 (γ_{B2} = 0,9); reinforcement AIII; M=80.0 toneforce·m . The results :

$x_1 \equiv \xi = 0.538(0.550); \ x_2 \equiv A_s = 35.96(35.91)cm^2; \ x_3 \equiv A_s' = 10.62(10.00)cm^2$.

3. The strength calculation for eccentric stressed members

Unknown variables of the NMP problem are accepted as in previous example:

$$x_1 \equiv \xi; x_2 \equiv A_s; x_3 \equiv A_s'.$$

The object-function has a previous air and conditions of strength is presented as:

$$\frac{2(R_B bh_0^2 x_1(1 - 0.5x_1) + R_s(h_0 - a') \cdot x_3)(K_1 + K_2(x_2 + x_3) - N)}{2e_0(K_1 + K_2(x_2 + x_3)) + (h_0 - a')(K_1 + K_2(x_2 + x_3) - N)} \geq N \tag{8}$$

Here :

$$K_1 = \frac{1.6 E_B bh}{3\left(\frac{l_0}{h}\right)^2 \varphi_1}\left(\frac{0.11}{0.1 + \delta_e} + 0.1\right),$$

$$K_2 = \frac{1.6E_s}{\left(\dfrac{l_0}{h}\right)^2}\left(\frac{h_0 - a'}{h}\right)^2 ,$$

Then the equation of balance is:

$$\left(x_2\left(a_0 + \sum_1^6 a_i x_1^i\right) - x_3\right) + \frac{N}{R_S x_1} - \frac{R_B b h_0}{R_S} = 0 \tag{9}$$

Parametrical and structure restrictions are recorded as

$$\left.\begin{array}{l} x_1 > 0, \\ x_1 \le 1.1, \\ x_2 - 0.0005 b h_0 \ge 0, \\ x_3 - 0.0005 b h_0 \ge 0. \end{array}\right\} \tag{10}$$

It is accepted that in case of symmetric reinforcement $x_2 = x_3$ in problem (4),(8)-(10).
The example 3: b=40cm; h=60cm; a=a' =4cm; concrete B25
($\gamma_{B2} = 0.9$); $l_0 = 6.0m$; $N_1 = 70.0$ tonforce; $E_B = 275000$ kgforce / cm^2; reinforcement AIII;
$M_1 = 21.3$ toneforce $\cdot$ m. . The results (value from [2] are in brackets):
$x_1 \equiv \xi = 0.235(0.235)$; $x_2 = x_3 \equiv A_s = 6.51(7.6)cm^2$;

4. The strength calculation of inclined sections of bended members

The length of projection of inclined crack $C_0 \equiv x_1$, the length of projection of inclined section
$C \equiv x_2$ and the area of cross reinforcement within the limits of inclined crack, referred to space
of cross bars $\dfrac{A_{sw}}{S} \equiv x_3$ are accepted as unknown variables of the NMP problem.
The NMP problem has the following air:
The object-function:

$$\min \Phi = x_1 \cdot x_3 \tag{11}$$

condition of strength:

$$\frac{(1 + \varphi_f)\varphi_{B2} R_{Bt} b h_0^2}{x^2} + R_{sw} \cdot x_1 x_3 + q_1 \cdot x_2 - Q_{max} \ge 0 \tag{12}$$

restriction on maximal value of $Q_B \le Q_B^{max}$:

$$x_2 - \frac{\varphi_{B2} h_0}{2.5} \ge 0 \tag{13}$$

restriction on minimum value of $Q_B \ge Q_B^{min}$:

$$x_2 - \frac{\varphi_{B2} h_0}{\varphi_{B3}} \leq 0 \tag{14}$$

restriction on minimum of web reinforcement:

$$x_3 - \frac{(1 + \varphi_f)\varphi_{B3} R_{Bt} b}{2 R_{sw}} \geq 0 \tag{15}$$

restrictions on value of C_0:

$$x_2 - x_1 > 0 \tag{16}$$

$$x_1 - \frac{\varphi_{B2} h_0}{2.5} \geq 0 \tag{17}$$

$$x_1 - 2 h_0 \leq 0 \tag{18}$$

and, at least, condition of equality $Q_B = Q_S$:

$$\frac{x_1^2 x_3 - (1 + \varphi_f)\varphi_{B2} R_{Bt} b h_0^2}{R_{sw}} = 0 \tag{19}$$

The example 4: b=20cm; h=40cm; a=3cm;concrete B15;
($\gamma_{B2} = 0,9$); cross reinforcement A-I;

$Q_{max} = 13.75$ tonforce;

$q_1 = 3.2$ tonforce / m.

The results (value from [2] are in brackets):

$x_1 \equiv C_0 = 45.2(44.8) cm^2$; $x_2 \equiv C = 107(108) cm$;

$x_3 \equiv A_{sw} / S = 0.07(0.07) cm^2 / cm$.

Conclusions

As is obviously, the results of solution of examples 1-4 having been received approach, have good coincidence with results from [2].
The all numerical experiments were conducted by computer IBM PC in environment of programming «EUREKA» [5] and have shown the high efficiency of offered approach. By this, the possibility and expediency of unification of calculation problems of strength for reinforced concrete members by reducing them to corresponding problems of NMP. Such approach can be fruitful also for the problems of calculation of strength in which the new physical models of reinforced concrete with plenty of unknown parameters are used and for which the «hand-operated» calculations are highly difficult. The new method of calculation of strength for reinforced concrete structures under the action of cross forces, offered in [6], can serve as example of such problem.

References

[1] SNiP 2.02.01-84. Concrete and reinforced concrete structures [in Russian],TsITP,Moscow,1985.

[2] Aid to the design of concrete and reinforced concrete structures for heavy and light concretes without of prestpressing of reinforcement [in Russian]. TsITP. Moscow,1989.

[3] Himmelblau D. Applied non-linear programming. MIR. Moscow,1975.

[4] Zalesov A.S., Kodish E.N., Lemesh L.L., Nikitin I.K. Calculation of reinforced concrete structures on strength, crack resistance and strains [in Russian]. Stroyisdat. Moscow,1988.

[5] Djakonov V.P. Reference book for application of system «EUREKA» [in Russian]. Nauka Moscow,1993.

[6] Zalesov A.S., Klimov Y.A. Strength of reinforced structures under the action of cross forces.
Budivelnik. Kiev, 1989.

Knowledge-Based System for Dynamic Analysis and Design of Structures

Abbes BERRAIS
Assist. Prof.
Abha College of Technology
Abha, Saudi Arabia

Abbes Berrais, born 1961, received
his civil eng. degree form Algeris
Univ. in 1985, MCs from Liverpool
Univ. in 1988, and PhD from Leeds
Univ. in 1992. He is currently an
assist. prof. in the construction dept
Abha College of Techn., KSA.

Summary

Dynamic analysis techniques for high-rise structures under earthquake effects are rapidly being developed and have been recognized as indispensable tools. The valid use of these techniques requires from the design engineer a comprehensive understanding of the limitations and inaccuracies of the analysis, and constant review of the results for errors. Computer-based structural design assistants are needed to provide engineers with decision support tools and to guide them through the dynamic analysis and design of high-rise structures. Therefore, the incorporation of knowledge-based systems techniques will play a great role in helping carrying out the complicated dynamic analysis and design process. This paper describes the development of a knowledge-based design tool for the dynamic analysis and design of high-rise structures subjected to earthquake forces.

1. Introduction

As structures become more complex in shape, taller and lighter, so the need grows for better and more reliable tools to help in the analysis and design of such structures. Dynamic analysis and design techniques for high-rise structures under earthquake effects are rapidly being developed and have been recognized as indispensable tools. However, their use in design offices requires specially trained and skilled engineers. Understanding the dynamic behavior and ultimate capacity is essential for the design of safe and economical structures. Computer-based structural design assistants are needed to provide practicing engineers with decision support tools and to guide them through the dynamic analysis and design processes. Therefore, the incorporation of knowledge-based systems techniques (KBES) will play a great role in helping carrying out complicated dynamic analysis and design of high-rise structures. This paper is concerned with the following: Development of a knowledge-based design tool (KBDT) for the dynamic analysis and design of high-rise structures subjected to earthquake forces. The design methodology included in this KBDT is based on the *ductility* concept, and is briefly described. Knowledge representation and the coupling of numerical methods with symbolic processing are also considered.

2. Earthquake Design Methodology

In earthquake analysis/design process, the engineer should consider the different factors that control the inelastic behavior of a building. The most critical factors to be considered in earthquake design are *ductility* and the detailing requirements. The earthquake design methodology (EDM) adopted in this research is divided into two phases (see Fig. 1): *preliminary design phase* and *detailed design phase*. In the first phase a simple elastic analysis is employed to establish an initial deployment of reinforcement. In the second an inelastic dynamic analysis is

performed to allow a detailed review and refinement of this reinforcement. The EDM has been applied to a particular type of lateral resisting system, coupled shear wall structures.

2.1 Preliminary Design Phase

This phase comprises three stages (see Fig. 1): conceptual design, preliminary analysis (elastic), and allocate reinforcement: in the *Conceptual design stage*, the overall form of the building is specified together with the relative positions of the lateral load resisting elements. The regularity requirements are checked against codes limitations. In the *Preliminary analysis stage*, an elastic analysis is carried out of the structure under the effect of the lateral static forces obtained in the previous stage. In the *Allocate reinforcement stage*, an initial estimate of elements reinforcement is carried out.

2.2 Detailed Design Phase

This phase comprises three stages (see Fig. 1): *detailed analysis* (inelastic dynamic), *review ductility*, and *refine reinforcement*. In the *Detailed analysis stage*, an inelastic dynamic analysis is carried out by choosing a suitable earthquake record to critically excite the structure. The inelastic dynamic analysis is carried out using the program DRAIN-2D [1]. In the *review ductility satge*, the rotational *ductility* of each structural element is estimated as [2]:

$$\mu_r = \frac{\theta_{max}}{\theta_y} = \frac{\theta_y + \theta_p}{\theta_y} = 1 + \frac{\theta_p}{\theta_y} \tag{1}$$

Where: μ_r is the rotational ductility; θ_{max} is the maximum rotation;
θ_p is the plastic rotation; and θ_y is the yielding rotation

The purpose of the *ductility review stage* is to check the performance of the structure as designed. In the *Refine reinforcement stage*, the reinforcement adopted in the *allocate reinforcement stage* is refined based on the result of the *ductility* requirements in the *review ductility stage*.

3. The Knowledge-Based Design Tool (KBDT)

The aim of the developed KBDT is to assists design engineers in the following tasks:
• Check the regularity requirements of a building.
• Estimate the different earthquake factors used in UBC [3] code requirements.
• Model and perform the inelastic dynamic analysis of the structure under earthquake records.
• Estimate the required reinforcement in structural elements.

A macro level schematic view of the KBDT architecture is shown in Fig. 2. The architecture has the following components:

• *Knowledge base:* comprises of several modules, each module is responsible ､ ﾙr a specific task;
• *Context:* contains the collection of facts which represent the current state of the problem in hand;
• *Inference Mechanism:* controls the system by modifying and updating the context using the knowledge in the knowledge base;
• *External analysis programs:* contain the structural analysis program DRAIN-2D, which is interfaced to the system;
• *Explanation facility:* provides the user with the necessary explanations about the task being performed; and
• *User interface:* provides a channel through which the user can interact with the modules of the system.

4. Non-linear Dynamic Analysis Module

The non-linear dynamic module is one of the knowledge-base modules of the system. It is concerned with the inelastic dynamic analysis of RC structures under earthquake records. It uses the DRAIN-2D finite element program [1]. Interfacing with the program DRAIN-2D takes place on three levels:

Input Data Level: At this level data needed for the dynamic analysis is prepared and checked for consistency. The earthquake record is selected from a set of records. The data in the resulting file DRAIN.IN, is read by DRAIN-2D.

Solution Process Level: At this level, the module executes the analysis program DRAIN-2D as a background process. During the inelastic analysis, limited information is displayed on the screen to inform the user of progress. More detailed information is directed to an output file DRAIN.OUT which is investigated at the evaluation level.

Evaluation Level: At this level a quantitative-qualitative transformation of the dynamic analysis results is carried out for the user. The module interfaces to the output file DRAIN.OUT, reads the results it contains, and transforms them into formats and graphical displays suitable for assimilation by the user (see Fig. 3). The results that are displayed and interpreted in this way include the following: Elastic/inelastic lateral deflections; Lateral drift at each floor level; beams moment, axial and shear forces, and bending moments; and rotational ductility.

In case the ductility requirements are not satisfied, or if the walls yield at the base before the beams, the user is informed by the system. The module then assists the user to carry out further inelastic analysis with modified element strength until the design is satisfactory. During the re-analysis phase, the module automatically modifies the input data for DRAIN-2D. The general steps taken to carry out the dynamic inelastic analysis of coupled shear walls are shown in Fig. 4.

5. Knowledge Representation

The knowledge representations used in this system include production rules, frames and data-driven procedures, these being provided by Quintec-Prolog and Quintec-Flex [4,5]. Additionally, the numeric procedures are represented using FORTRAN 77 as external programs. An example of a typical rule that decides on the type of reinforcement configuration to be used in the beams follows:

Rule Beam_reinf1
      IF Vbcr is the critical beam shear stress
      AND   min_cal_beam_shear_stress > Vbcr
      THEN compute_diag_steel_area
      BECAUSE
        minum cal_beam_shear stress is > 0.1*beam_length*fcu**0.5/beam_height

An example of using Quintec-Flex frames is the representation of earthquake records for use by the program DRAIN-2D. The San Francisco record is represented as frame with slot values as shown in Fig. 5.

6. The User Interface

The acceptability of any KBDT depends largely on its user interface. The design of a good user interface must consider many aspects of human computer usage ranging from cognitive models of the user's thought processes to the aspect of usability. It is assumed that the user is knowledgeable

about structural design, but not necessarily about dynamic analysis concept. The following system requirements were identified and form the objective of the system implementation:
Easy to use; Takes the initiative and question the user; Teaches the user how to formulate the problem; Allows the user to invoke the system at any level of abstract; and informs the user about the next step in the design process. The user interface of KBDT is shown in Fig. 3.

7. Conclusions

In this paper a prototype KBDT for the dynamic analysis and design of high-rise structures was described. The prototype system helped on the iterative design to achieve a balance between element strength and stiffness to fulfil ductility requirements. The integration of symbolic processing and dynamic analysis methods is a necessity for a robust and practical computer-aided earthquake design. Moreover, KBES technology could be used in collecting and managing earthquake engineering expertise from different sources and formalizing this knowledge for future use by less experienced engineers. Heuristics alone are not sufficient to solve real design problems. The system needs to be linked to numerical and structural analysis modules.

The KBDT has accomplished the following:

- Automate much of the dynamic analysis/design process, which could free the design engineer from the more tedious aspects of design and allow him to concentrate on concepts such as ductility.
- Help the structural engineer on the efficient use of FEM programs, preparation of input data, modeling, and interpretation of results.
- Minimize the time spent to prepare the input data to the program DRAIN-2D, and help the structural engineer in the decision making process.
- Enable the designer to control the location and magnitude of inelasticity in structural members using inelastic dynamic methods. This allows the engineer to design the structure based on the ductility concept.

References

1. Kannan, A. E., and Powell, G. M. (1975), "DRAIN-2D, a general purpose computer program for dynamic analysis of inelastic plane structures", Rep. No. EERC 73-22, Earthquake Engineering Research Center, University of California, Berkley, USA.
2. Fintel, M., and Ghosh, S. K. (1982). Explicit inelastic dynamic design procedure for aseismic structures, ACI Journal 79, pp. 110-119.
3. ICBO 1991 UBC:91, *Uniform Building Code*, International Conference of Building Officials, Whittier, CA.
4. Quintec System Ltd. (1989). *QUINTEC-PROLOG*, System Predicates, Unix version, UK.
5. Quintec System Ltd. (1989). *QUINTEC-FLEX*, User Manual, Unix version, UK.
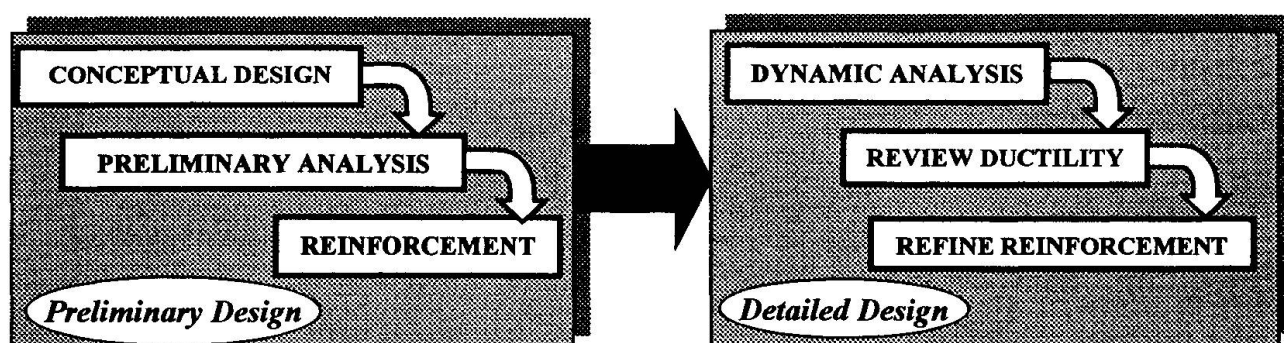
Fig. 1 Earthquake design methodology
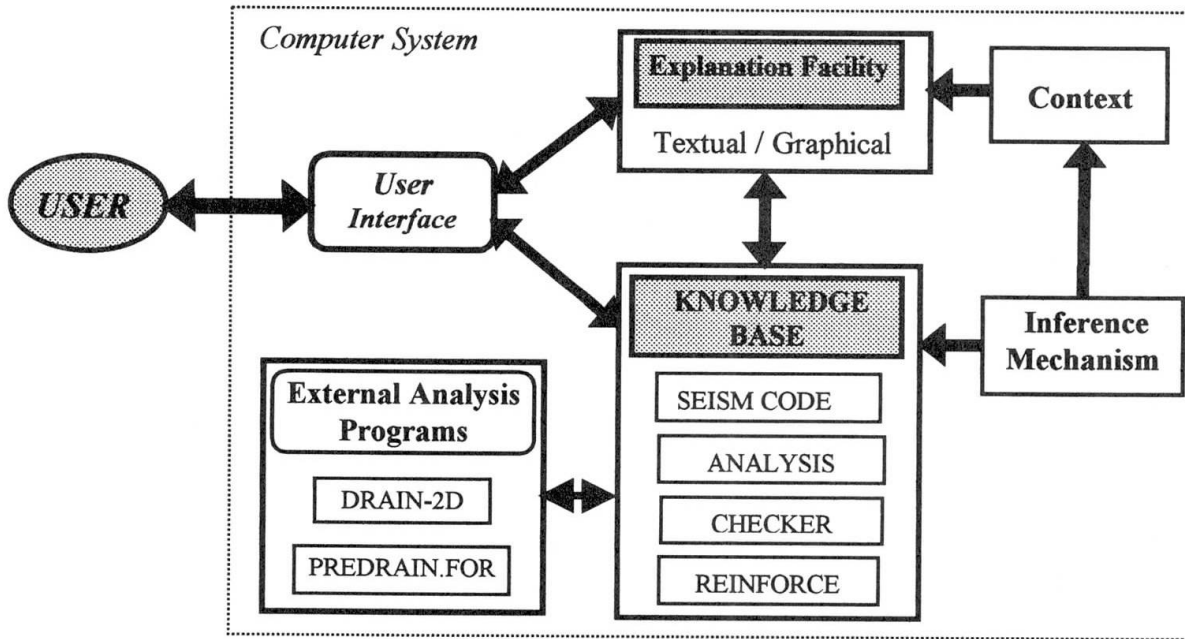
Fig. 2. Architecture of the KBDT system
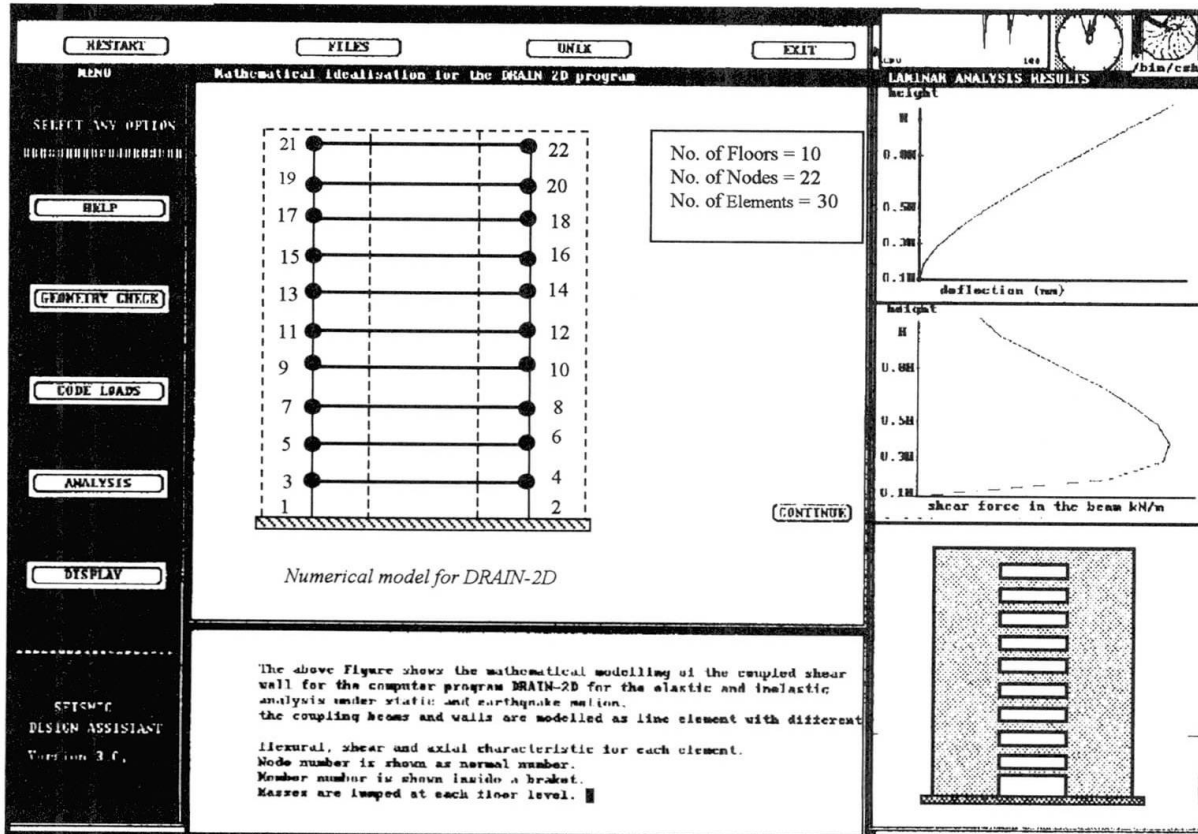
Fig. 3. User interface of the KBDT
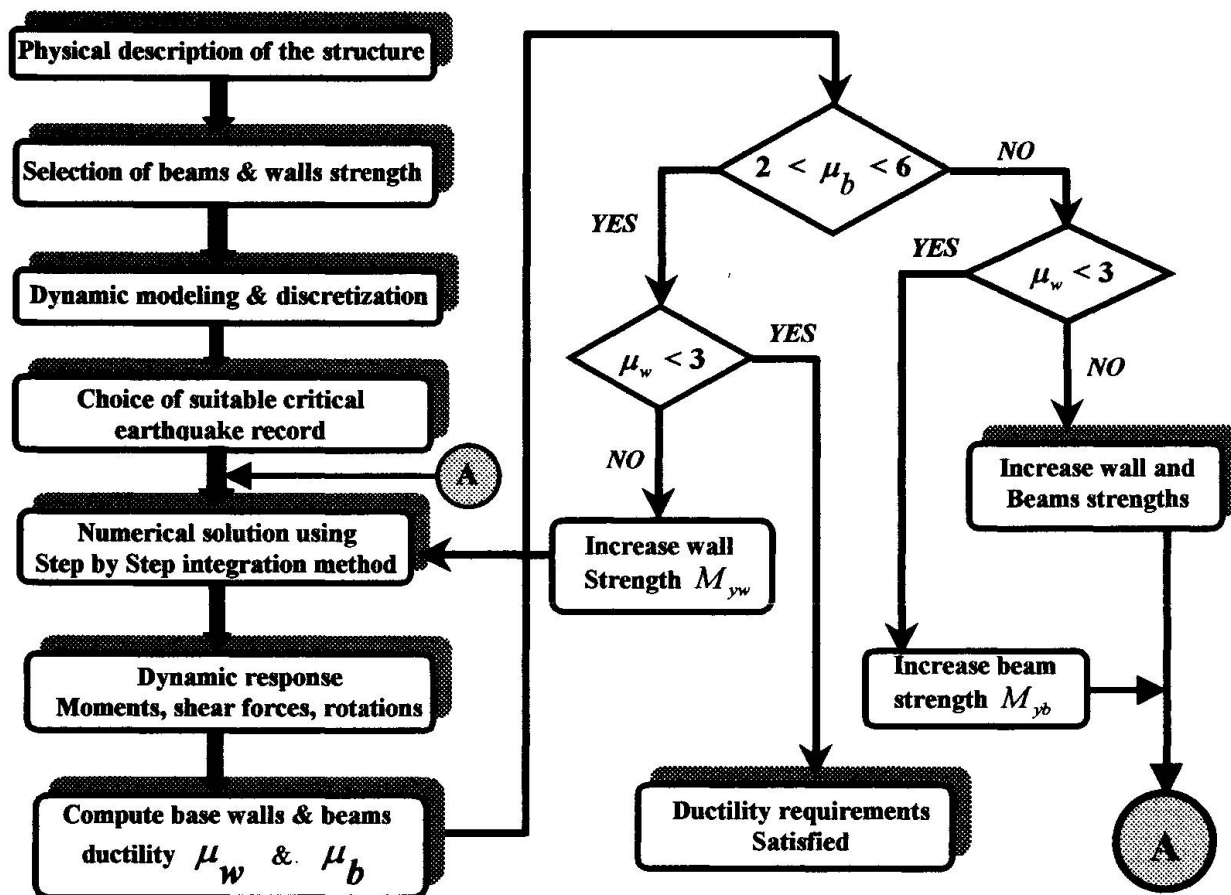
Fig. 4. Flowchart for dynamic inelastic analysis procedure
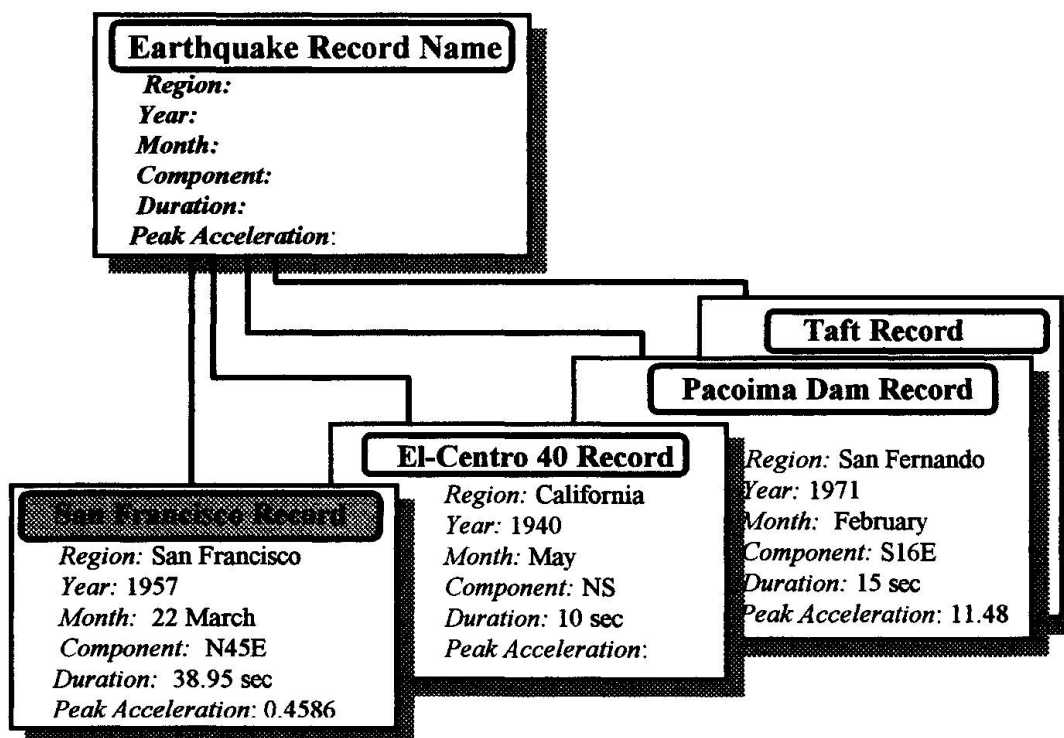
Fig. 5. Frame representation of different earthquake records

Monitoring the Big Bridges across the Danube in Austria

Helmut WENZEL
Dr Eng.
Vienna Consulting Eng.
Vienna, Austria
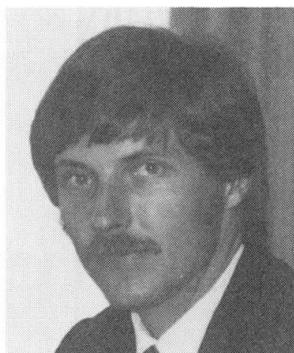
Helmut Wenzel is a member of
WC V of IABSE. He earned a
Ph.D. in Bridge Constr. from the
Univ. of Vienna in 1978 and is
the Managing Dir. of VCE, with
offices in Vienna, Taiwan and
Korea. Dr Wenzel also teaches
Bridge Design and Construction
at the Univ. of Vienna.

Summary

Since the spectacular collapse of the famous Reichsbrücke in Vienna in the year 1976, the attention of Austria Bridge Engineers is very much focused on the big bridges across the Danube. The frequency of traffic on most of the bridges has reached the limit, touching some 140.000 vehicles per day in the extreme cases. This vital lifelines have to stay open under any conditions. Therefore the assessment of the structural condition of the bridges is of upmost importance. This paper reports on the works carried out on the bridge assessment covering 9 major bridges with the use of the dynamic characteristic method BRIMOS developed by VCE. The potential of the method is demonstrated and relevant tests are provided.

1. Introduction

The main target of the works was to create a numerical tool for the assessment of the structural stability of the major bridges across the Danube. As a basis the tools of the vibration characteristic method was used. It is based on Ambient Vibration Tests carried out on the bridges frequently. They are compared to analytical calculations with Finite Element computer models, which represent the planned condition of the structure.

The Bridge Monitoring System BRIMOS has been developed over the past 2 years to carry out ambient vibration tests economically. Useful results for the assessment are provided. The major mile stones of the program are:

- Recording of the characteristic through 8 accelerometers which are moved over the bridge to cover the whole area
- Calculation of a representative spectrum, which represents the dynamic characteristic
- Calculation of structural damping by filtering out certain Eigenfrequencies and extraction of damping with the use of the Random Decrement Technology (RDT)
- Numerical assessment on structural integrity under consideration of the measured values
- Determination of the Eigenform as a confirmation for the fitting of calculation and measurement
- Search for damage indicators in the signals and location of the damages
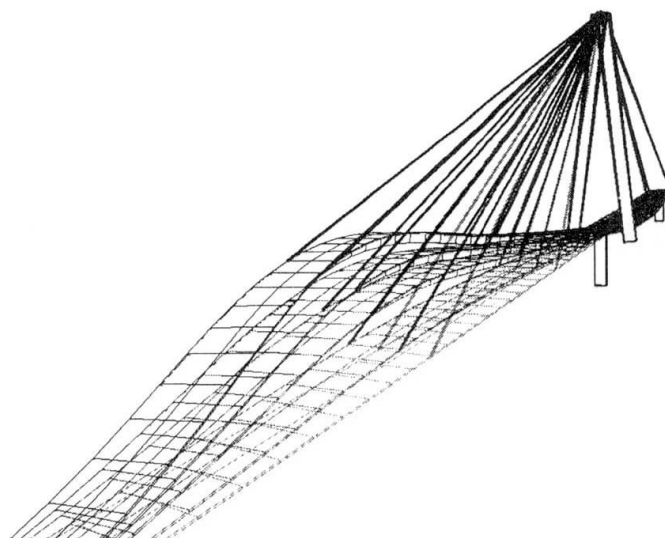
Fig. 1 Eigenmode animated from measurement   *Photo 1 Hainburg bridge*
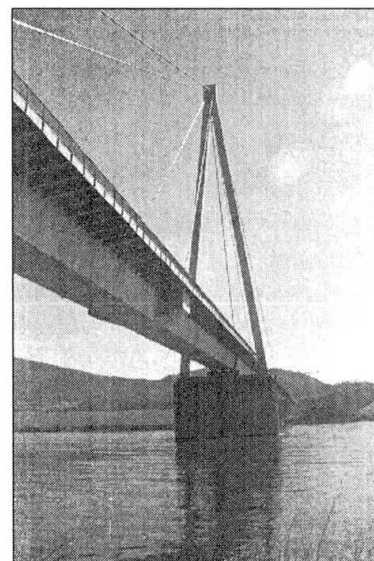
For each structure a report is prepared providing the basic dynamic characteristic, an assessment of structural safety, the values of damping for the structure and the assessment of eventual hidden damages. In the long-term it is intended to undertake measurement frequently and to calculate trends from the results.

The method has been proven by a number of tests in the laboratory and by a major number of tests on bridges on site.

2.   The Bridges across the Danube

In Fig. 6 of this paper the bridges considered in this report are described. All kind of structures are represented. There is a number of cable stayed bridges made from steel or concrete or even composite deck structures, a number of steel bridges with various spans, a major composite bridge and a long span concrete bridge. Due to the huge amount of structures and data only representative results can be provided.
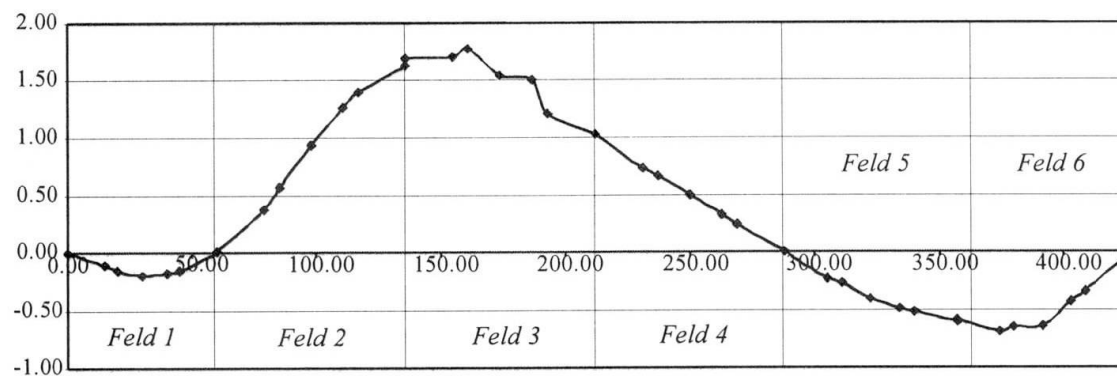
Fig. 2 1. Vertical Eigenmode of the Hainburg bridge

Traffic Load

Temperature

Vertical Eigenmodes

Longitudinale Eigenmodes

Cross Eigenmodes
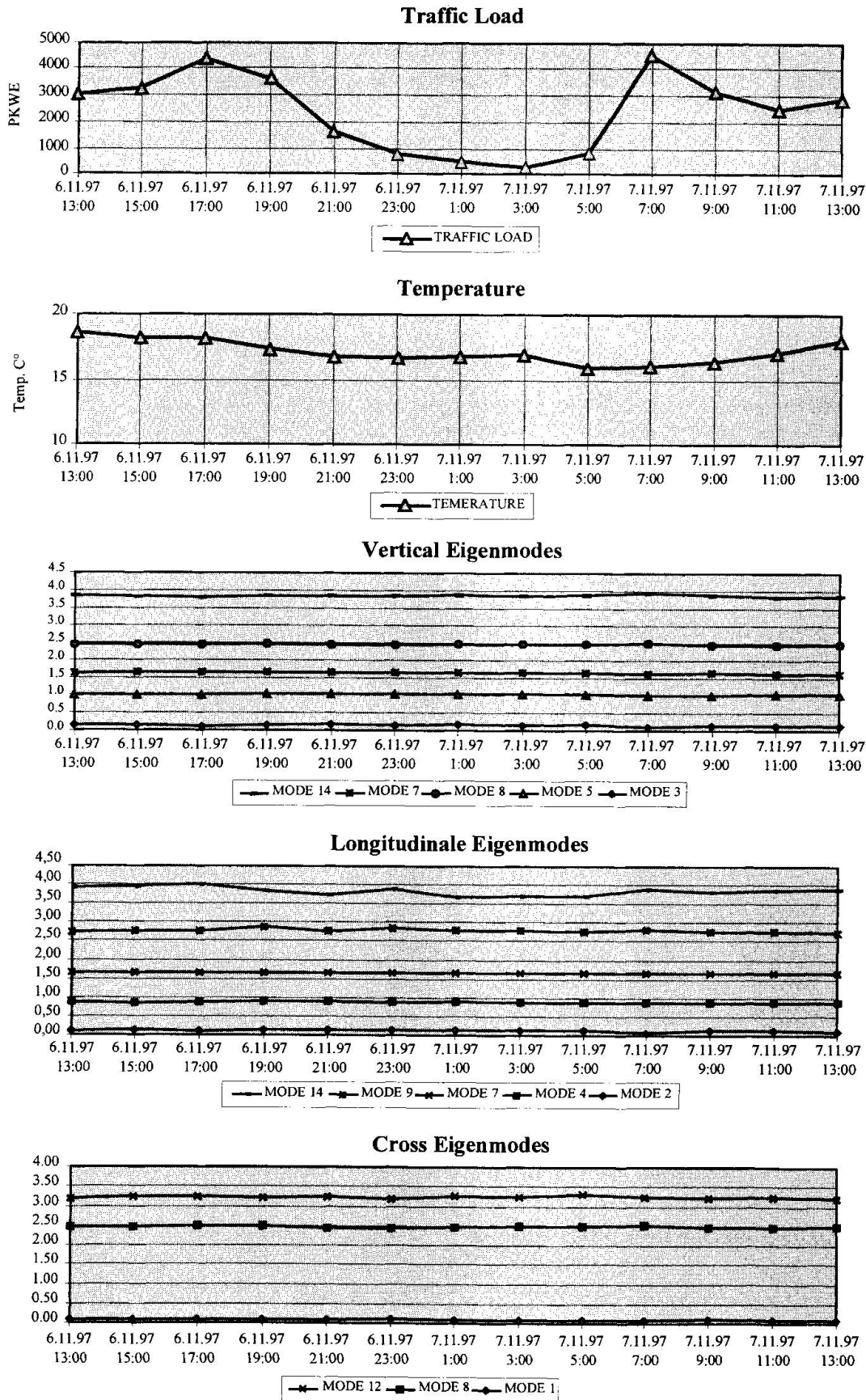
Fig. 3 24 hour test results, traffic load, temperature, frequencies

3. Tests and Calculations

For each of the structures a base measurement has been established. It consist of a minimum of 5 measurement points per span and side of each deck structure. The time requirement for a serious test of a bridge of 200 meter length is approximately 10 hours. The characteristic is recorded at a Sampling – Rate of 100 Hertz and per measurement 50.000 points are stored. Amplifiers and filters are used according to the requirement of each structure. The system is calibrated by a laser displacement device, which provides actual displacement in millimeters. For each of the bridges a dynamic Finite Element Calculation is carried out. It concentrates on the idea of the designers and follows strictly the drawings. Therefore it will be representative for the "should be" case. It serves to define the starting point of the life time performance check.

4. Major Results

The Eigenfrequency of a structure is depending on a couple of items out of which the most important are: The mass, the stiffness, super imposed dead loads, traffic loading both static and dynamic, strain from temperature difference, internal stresses from prestressing and some minor other phenomena not yet fully understood. The method had to be calibrated against those influences to focus the results on the most useful influences, which are stiffness and damping.

One of the most important items was to demonstrate, that the ambient vibration method produces reliable results independent from the traffic loads applied. This was done by means of a 24^h test on one of the representative bridges, which is the Nordbrücke. Permanent measurement has been carried out on a day, where the change in air temperature was only 2°C. The traffic on the bridge varied from 130 vehicles at 3 o'clock in the night to almost 5.000 vehicles per hour during the peak traffic at 7 o'clock in the morning. The variation in the results, considering more than ten fundamental modes is in average below 1 %. This means, that ambient vibration data can be extracted almost under any traffic conditions. The enclosed Fig. 3 show the results over 24 hours including the temperature change, the vehicle loading and some of the relevant eigenfrequencies.

Bridge	1. Vertical	Damping	max. span	Deck
Hainburg	0.53	1.12%	228.00	steel
Donaustadt	0.67	0.44%	1.86.00	composite
Reichsbrücke	0.83	0.68%	170.00	concrete
Brigittenau	0.75	1.67%	175.00	steel
Floridsdorf	0.77	1.44%	167.50	steel
Nordbrücke	0.86	2.30%	83.40	composite
Tulln	0.53	1.60%	176.00	concrete
Melk	0.70	1.64%	190.00	concrete
Steyregg	1.23	1.63%	181.00	composite

Tab. 1 Vertical frequency and corresponding damping

Another major task was to perform the identification of the Eigenmodes from the measured data. This is demonstrated at the Hainburg Cable Stayed Bridge. The Fig. 1 and 2 show the calculated Eigenmode as well as the measured one. It is obvious that the results are very good. The measured modes are carried on to an animation program, which produces real time or accelerated demonstrations of that measurement. These are compared with the calculations and the differences are identified. Very often the interpretation is simple. It gives an idea about the

function of important parts of the structure. Both, calculation and measurement, can be superimposed to demonstrate the differences.

5. Damage Identification

The identification of damages beyond the results of visual inspection are the development area of the future. It is well established, that any damage is represented in the signals. The difficulty hides in the interpretation. It was observed, that the results are varying very much depending on the qualification of the operator. Very good results have been achieved by bridge engineers, which learned to handle a monitoring system. Monitoring engineers normally failed to assess abnormal recordings, which they tended to identify as problems with the monitoring system.

Therefore the main task shall be to identify patterns of signals, which indicate a normal condition. A typical example is shown in Fig. 5, which represents a crack in a prestressed concrete structure. The so called double peak in the 1. vertical Eigenfrequency, effected are mainly the lower frequencies, indicates a variation of stiffness with a variation of amplitude, i.e. traffic loading. In this case the evaluation of periods with passenger car loading provides the lower frequencies as the case with truck loading. This indicates, that the crack is open under normal conditions and closes when trucks excite this structure. Feeding this information into the finite element model it can be calculated that a crack, reaching from the bottom of the structure 60 cm into it, is active. The location of the crack was also determined, to be a construction joint. This theory has been confirmed through measurement on other structures, with well known active cracks.
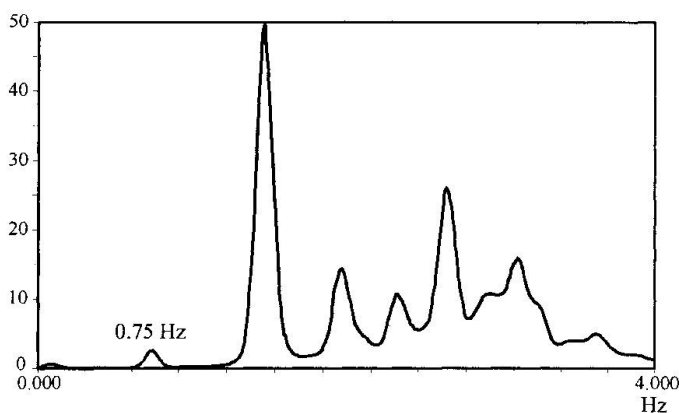

Fig. 4 ANPSD of Brigittenau
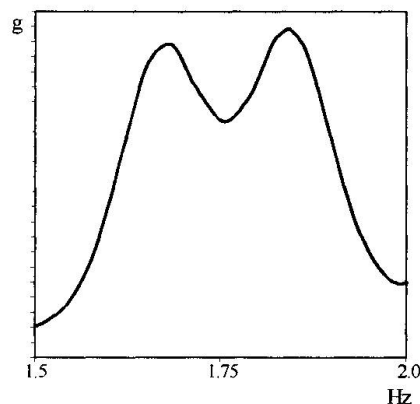
Fig. 5 Double peak

6. Conclusion

The promising results of the ambient vibration tests make it necessary to invest in further development of the damage identification tools. It will not be possible to find easy and closed solutions for most of the problems. Therefore an identification routine based on Fuzzy Logic will be necessary. It has been started already to collect relevant results of bridges as many as possible. These will be stored in a data bank, which will form the basis for comparison of cases. Although it is clear, that it will still take a long time to make these methods simple, the proof has been provided, that it works. A key issue of the subject is the education of bridge engineers in dynamics and monitoring to provide the basis for the understanding of the procedures and physics. For this purpose more major demonstration projects shall be implemented.
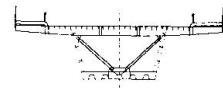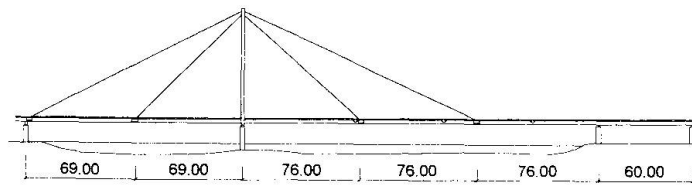
Donaubrücke Hainburg
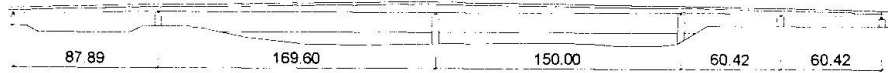
Reichsbrücke
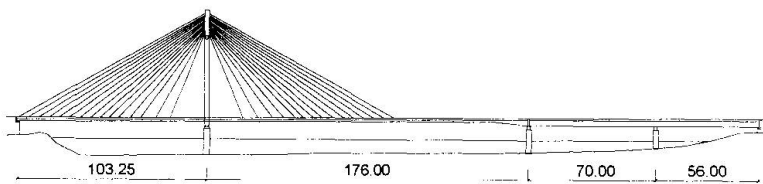
Tulln West Bridge
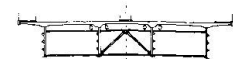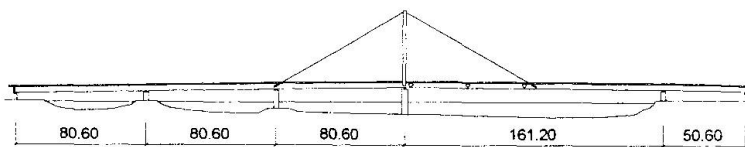
Donaubrücke Steyregg
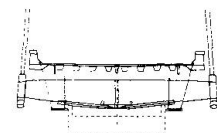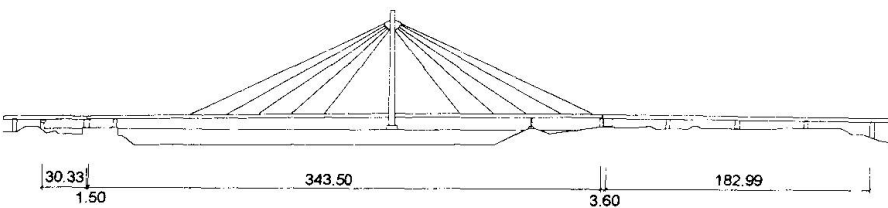
Donaustadtbrücke
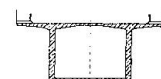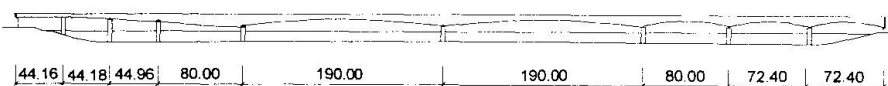
Donaubrücke Melk
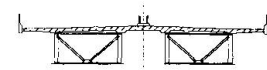
Nordbrücke
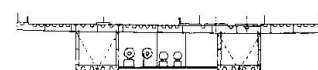
Donaubrücke Floridsdorf

Fig. 6 Bridge dimensions

Dynamic Tests and Monitoring of a Highway Bridge over the Danube

Jan BENCAT
Prof.
Univ. of Zilina
Zilina, Slovak Republic

Jan Bencat, born 1943, received his eng. degree in 1967 form TU Cracovia (Poland) and Ph.D. at UTC Zilina in 1973. He is currently Prof. of Structural Mechanics at Civil Eng. Faculty, Univ. of Zilina.

Summary

The dynamic response behaviour of a prestressed concrete seven span highway bridge (761,0 m long) was examined in September 1990 as a part of the static and dynamic loading tests (DLT)of the bridge. In this investigation, a structural measuring technique using vehicle-induced vibrations as well as forced vibrations induced by the rocket engines was developed for fullscale testing of the bridges. The data yielded the dynamic characteristics of the bridge e. g. natural frequencies f(j), mode shapes, dynamic load factor δ (DLF) and the damping of the structure (ϑ). The obtained dynamic characteristics were compared with the theoretical computed data. Monitoring of the highway bridge over the Danube (La Franconi Bridge) has been carried out in 1991-1997, to evaluate the accuracy when using a simple measurement of a well defined eigenfrequency to give a long term overall indication of deterioration or crack formation.

1. The Bridge Arrangement and Dynamic Loading Test

The main bridge structure is composed of seven span continuous beams with one frame pier (P3). Other supports are formed by seven massive piers. The total length of the bridge is 761.0 m with spans 83.0 m + 174.0 m + 172.0 m + 4 x 83.0 m. The highway bridge consists of two independent bridges (left and right bridge -LB,RB) with three traffic lanes, on each bridge for one direction only and sidewalks on both sides. The bridge box cross-section is shown in Fig. 1 and the longitudinal section, in Fig. 2. The bridge including multispan junctions is fully described in [1]. *Testing procedure and experimental analysis.*The test programme included field measurements using the instrumentation described in [3] so as to ensure coverage of entire possible range of vibration. The vibration amplitudes were investigated and recorded in 18 selected points. The time history of vertical as well as horizontal vibration has been registered by accelerometers (Brüel-Kjaer, BK-8306) in the 2nd and the 3rd span of the bridge (A1-A8) and in the other spans by inductive displacement transducers (IDT, range ±40 mm), points R1- R10, see Fig.1 and Fig.2. Output signals from the accelerometers were preamplified and recorded on two four-channel portable tape FM recorder (BK-7005) and simultaneously via DISYS software on PC/486 at the measuring station DMS-1. The signals from the IDT were recorded simultaneously at the station DSM-2 and DSM-3 by the same way as the signal from accelerometers. The experimental analysis has been carried out in the laboratory of the Department of Structural Mechanics UTC Žilina.

The dynamic load factor δ_{OBS} and frequency response spectrum (PSD) has been determined using the record obtained from passing vehicle velocities over the bridge by computer PC/486 via DISYS programme and two-channel real time analyzer BK-2032. *Testing load and experimental results.* The use of the test load has been in accordance with [3]. Two lorries TATRA-815 of mass 26 660 kg and 26 740 kg were used for the highway pavement. Rocket engines (RE) impulsive load were separately used, too. Static loading test (SLT) was perfomed before the
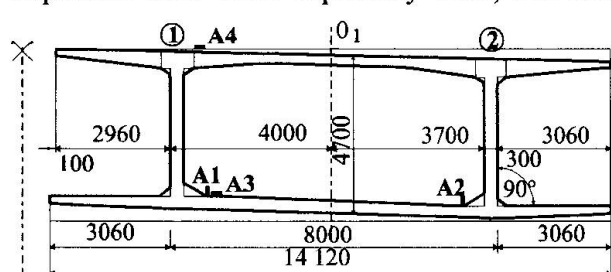
Fig.1 Bridge cross section
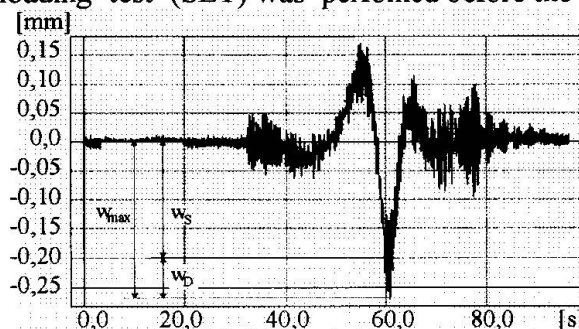
Fig.3 Time history of bridge vibration due to passing vehicle at the point 117(v −62,91km/h)
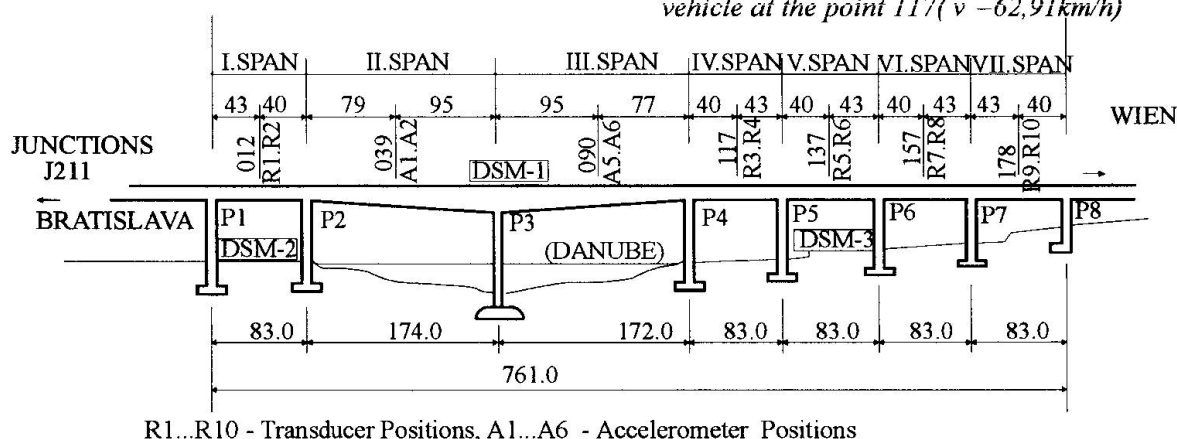
R1...R10 - Transducer Positions, A1...A6 - Accelerometer Positions

Fig.2 Longitudinal section of the bridge

dynamic loading test (DLT) with both vehicles TATRA-815. Experimental procedures have been discussed in detail by autor [3]. Formula (1) gives the criteria [2] for evaluation of moving load dynamic effects on the bridge structure

$$(\delta_{OBS} - 1)\eta_{DYN} \leq (\delta - 1)$$ (1)

where (see also Fig. 3), $\delta_{OBS} = w_{MAX} / w_S$ and $\eta_{DYN} = w_{DYN} / w$ The vertical static displacements at characteristic joint (012-178) due to standard live load (w) and due to testing load (w_{DYN}) have been computed by the bridge designer [1]. The calculated dynamic effectiveness η_{DYN} with theoretical and experimental values of the vertical displacements varied in the range η_{DYN} =0,09 ÷ 0,154, for different span of the bridge. The dynamic load factor δ (DLF) used by the designer for the bridge under investigation according to [4] is $\delta = 1.10$, see also [1]. DLF of the experimental tests [3] are obtained from formula $\delta_{EXP} = 1 + (\delta_{OBS} - 1)\eta_{DYN}$, see also Fig. 3. The DLF against vehicle velocity are plotted in Fig. 4, 5. Natural frequencies have been obtained by using the spectral analysis from recorded responses due to various types of dynamic loading, see also Table 1. Since the accelerometers recorded only the dynamic component of vibrating structures, so we can consider those signals as an ergodic and stationary. The results of the analysis are fully described in [3]. Only two PSD are shown in Fig. 6, 7 of this paper. The comparison of theoretical (FEM) and experimental results of the natural frequencies $f(j)$ of the vibration bridge according to [3] are presented in Table 1.

The spectral analysis of the vibration time histories made it possible to ascertain the dominating frequencies of bridge vibration by sharp peaks plotted in power spectra. The character of the vibration caused is heavily dependent on dynamic response excitation.
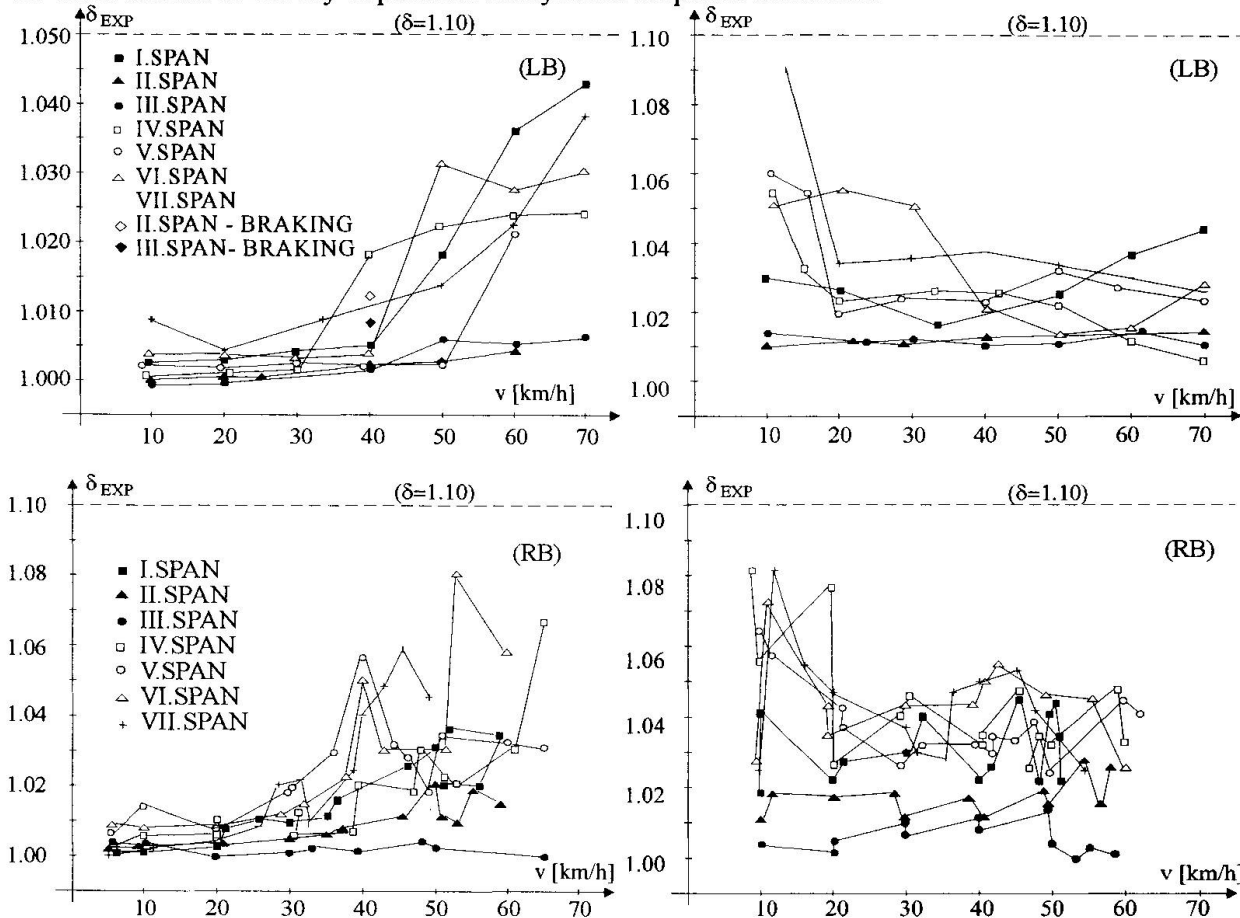

Fig. 4 DLF δ_{EXP} against vehicle velocity
        - vehicle smooth passing

Fig. 5 DLF δ_{EXP} against vehicle velocity
        - vehicle obstacle passing

The results of the correlation analysis [3] showed that the vibration of the bridge is not ambient vibration. The bridge vibration has predominate vertical components (bending vibration). In this tests it was possible to predict the damping characteristics according to [2] by using logarithmic decrement.The evaluation of the logarithmic decrement ϑ has been done from records of fre bridge vibration due to impulse rocket engines. The logarithmic decrement corresponding to the first and second modes of the bridge vibrations varies in range $\vartheta=0,024 \div 0,049$.

3.Bridge Dynamic Parameters Monitoring

Progressive deterioration of concrete structures (RC) due to alkali silica reactions and frost-thaw influence has become a serious problem. It has increased the importance of making observation on full scalle structures in order to obtain the experimental results necessary for the development of theories for predicting service life.

It has been the scope of this work to evaluate whether the relative change of a well defined natural frequencie or the change of the corresponding damping and the change of RMS value of the displacements amplitude of the bridge vibration observed by traffic loading can be used to give an overall indication of deterioration or crack formation. The monitoring technique based on

measurement of the time history of the bridge vibration due to regular traffic is not meant to give detailed information but to be a technique simple to use to deside whether more detailed methods should be used.

During the years 1991-1997 La Franconi bridge over the Danube has been investigated by 24 hours monitoring tests in the summer and the winter time . A theoretical prediction of the bridge behaviour and preliminary dynamic loading tests are reported in [3].
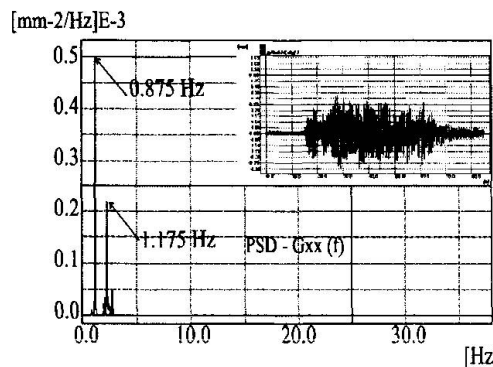
[mm-2/Hz]E-3

Fig. 6 PSD at point 039 caused by TATRA 815

[mm-2/Hz]E-4
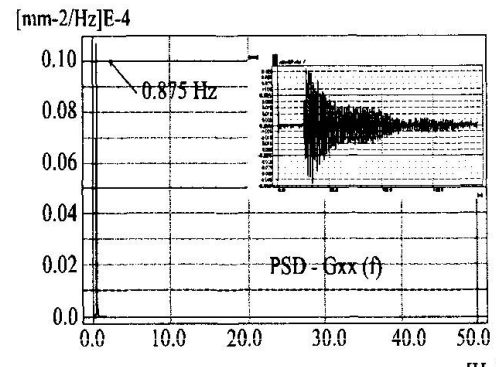
Fig. 7 PSD at point 039 caused by RE $^{[Hz]}$

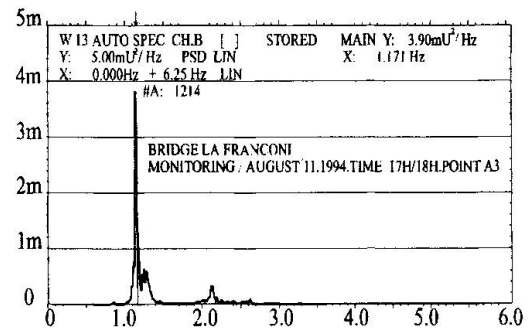| NATURAL FREQUENCIES / Hz /			EXCITATION TYPE
f(j)	CALCULATED	MEASURED	
1	0,865	0,875	RE, TATRA 815 - BR
2	1,157	1,175	TATRA 815 - OBST
3	1,919	1,9	RE
4	2,042	2,148	TATRA 815
5	2,3	2,275	RE, TATRA 815 - OBST
6	2,686	2,775	RE, TATRA 815 - BR

Table 1 The natural frequencies

Fig. 8 Monitoring PSD at point 039

Testing procedure and experimental analysis. The vibration amplitudes were investigated and recorded in selected points of the second and the third span, see Fig. 1, 2. The time history of vertical vibration has been registered by accelerometers (Brüel-Kjaer, BK-8306) at points 039 and 090 (A1, A2, A5, A6) on each independent bridge.

Output signals from accelerometers were preamplified and recorded on four-channel analogue FM recorder BK-7005 and simultaneously via A/D convertor DAS-16 on portable notebook computer (PC/486) with special software (DISYS) and hardware facilities for 24 hours continuing test. The records obtained in the bridge monitoring tests were investigated by using frequency analyser BK-2034 and mentioned PC facilities. Fig. 8 shows power spectral densities (PSD) as an example of the spectral analysis of the monitoring test performed in August, 1994. The damping parameter (D-critical damping coefficient) was found by means of the 3dB bandwith method and curve fitting techniques. The amplitude analysis has been used to obtain RMS amplitude value of the bridge vibrations during the monitoring tests.

Experimental results. Results giving frequency and damping for lovest natural frequency in bending and RMS amplitude value from the monitoring tests of the bridges during whole measuring period are shown in Fig. 9. A 2.7% change in frequency is observed during a year (summer-winter) but it is systematic from one year to the next and is partly due to changes in ambient temperature. By measuring the frequency at the same time of year the changes from year to year are small and non systematic and correspond to a coefficient of variation of about 0.01. This may be considered negligible compared with the changes in natural frequency of about 30% corresponding to advanced deterioration observed in [5].
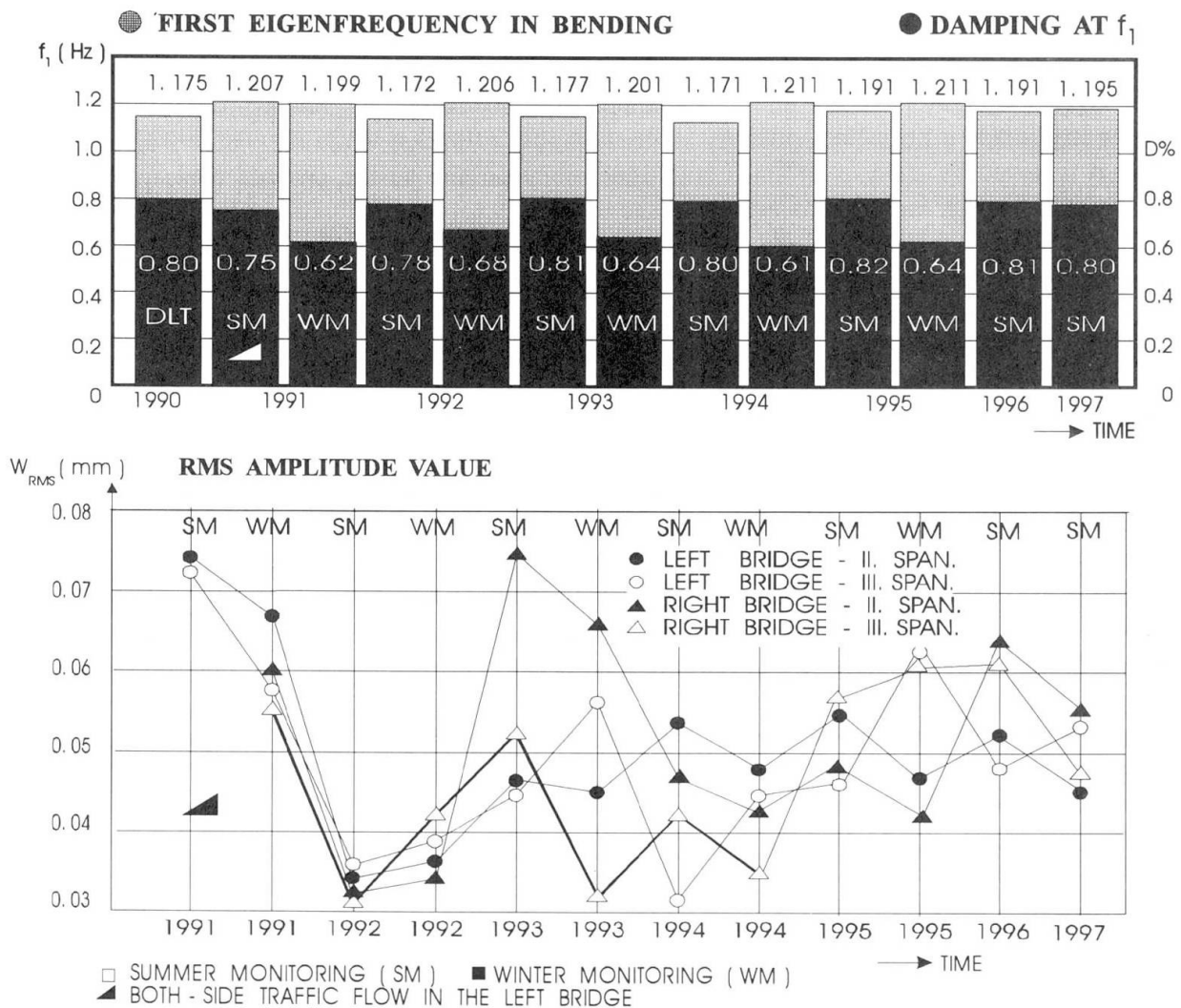
Fig.9 Changes in relative frequency, damping and displacement
RMS amplitude values, 1990 - 1997

There is not the same systematic change of damping and scattering of results is big. What causes these changes is not clarified. There are changes in the temperature during the day. This may give changes in length of bridge which can influence support conditions and damping. Windspeed, water level, ambient relative humidity and temperature gradients through the deck, transport in the bridge deck, in particular at the surface, and may there by also change damping [6],[7].

There is a difference of the discplacement amplitude RMS value measured in may 1991 in comparison with other measurements results. It was maybe caused by both-side motor traffic flows on the left bridge. All the following measurements were performed in conditions of the one side traffic flow on each of the two bridges La Franconi. The changes of the amplitude RMS value is caused mainly by changes of the intensity of the regular motor traffic.

4. Conclusion

The experimental analysis of the bridge dynamic response caused by moving load as well as impulsive load made it possible to identify six basic modes of bridge vibration. These frequencies have been received by analysis of small amplitude vibration and so the analysis corresponds to linear vibration. It was possible to evaluated the damping characteristics of the bridge structure only from limited number of measurements. They are therefore only indicative. The experimentally achieved dynamic load factor $\delta_{EXP} < 1,09$ shows that real stiffness of structure is fully comparable with the corresponding value for, $\delta = 1,10$ obtained by computation. The comparison of theoretical and experimental results of the bridge parameters shows good agreement of theoretical and experimental values of natural frequencies. The criteria of all loading states by the Slovak standard [2] are seen to have been fulfilled.

The monitoring tests results show that the relative change of a well defined natural frequency seems to be very little influenced by changes in temperature, humidity, support conditions, etc., in fully hardened not deteriorated RC structure of simple geometry, if measurements to be compared are made at the same time of the year. This indicates that the monitoring tests may prove useful by giving an idea of the overall development of long term deterioration and cracking in RC structures. The change in structural damping can so far not be used in a similar way because of its big dependance on mentioned secondary influences which are comparable with deterioration or cracking influences on change of structural damping.

The changes in deflection amplitude RMS value are heavily dependent on intensity of regular motor traffic in the bridge deck, but vary within of the 50% RMS amplitude range measured during the whole measuring period.

5. Acknowledgment

References

[1]   ŠEVČÍK, J. et. al. (1989): "The Highway Bridge D-201-HMO over the Danube in Bratislava". Static Computations Research Report, Dopravoprojekt Bratislava, (in Slovak)

[2]   The Slovak Standard No. 73 6209 - Loading Test of Bridge

[3]   BENČAT, J. (1990): "Report on Dynamic Loading Test Results of the Highway Bridge D-201-HMO over the Danube in Bratislava ".Report HZ-1-102-90/2.UTC Žilina ,Dept.of Structural Mechanics, (in Slovak)

[4]   The Slovak Standard No. 73 6203 - Bridge Loading

[5]   Askegaard, V. & Lanso, H. E. (1986): "Correlation between Changes in Dynamic Properties and Remaining Carrying Capacity", Materiaux et Constructions, Vol. 19, No. 109, 11-20

[6]   Swamy, N. & Rigby, G. (1971): "Dynamic Properties of Hardened Paste, Mortal and Concrete". Materiaux et Constructions, Vol. 4, No. 19, 13-40

[7]   Casas, J. R. & Aparicio, A. C. (1994): "Structural Damage Identification from Dynamic-test Data". Journ. of Struct. Eng., Vol. 120, No. 8, Paper No. 3439

Reconstruction Design for PC Girders Damaged by the Kobe Earthquake

Hidesada KANAJI
Civil Eng.
Hanshin Expressway Public Corp.
Osaka, Japan

Hidesada Kanaji, born 1962, received his Master Degree of Eng. in 1988 from Kobe Univ. He has been engaged mainly in designing expressway structures and supervising construction site.

Summary

The bridge discussed in this paper has simple composite PC girders supported by six RC T-beam piers and one RC rigid frame pier. It is located in Nada Ward, Kobe and was severely damaged by the Kobe Earthquake. The damage included inclination of the eccentric piers and damage to the end cross beams. To restore the bridge, a girder connection with isolators was used to distribute and reduce inertia force. Specifically, the slab-rubber-hinge girder connection method was developed. Isolators with both lead-rubber bearings (LRB) and sliding rubber bearings (SRB) and restrainers having rubber-sheathed chains were also used. Foundations, piers and girders except the damaged end cross beams were reused with some repair.

1. Basic of Structural Framework Design

In the design, focus was placed on developing a girder connection structure and employing omnidirectional seismic isolation to decrease both longtudinal and lateral inertia forces acting on eccentric piers whose reinforcement possibilities were limited (see **Fig. 1**). The preliminary design was first drawn up by applying the seismic coefficient method and the final, comprehensive design was based on the nonlinear dynamic analysis of the seismic record of the Kobe Earthquake at the Japan Meteorological Agency Kobe station. In addition, to verify the validity of the adopted isolated structures, the cumulative strain energy was calculated by analysis of the entire bridge, obtaining the proportions of seismic energy shared by the foundations, piers and isolation bearings (see **Fig. 2**).

2. Characteristic Structure Components

2.1 LRB-SRB Combined Isolation System

Two kinds of bearings, shown in **Fig. 3**, were applied to the bridge. SRBs were placed under the main girders to support the vertical load, and LRBs were placed in the gaps left under the end cross beams by removing part of their underside to absorb inertia force during an earthquake. This system was applied to the bridge in this paper which made use of thin rubber pad bearings
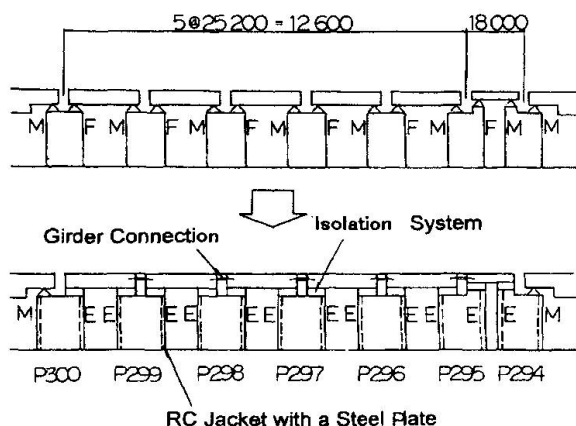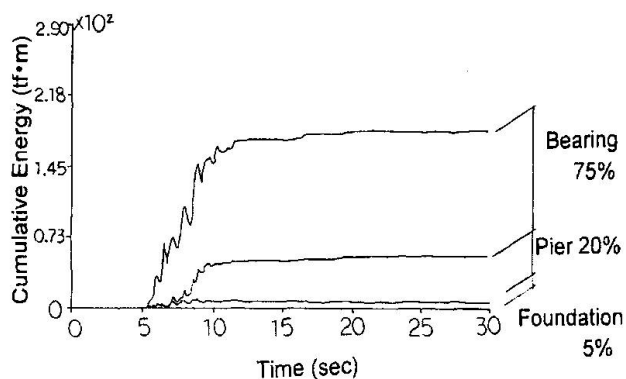
Fig.1 Structural Framework

Fig.2 Cumulative Strain Energy

under girders so as to limit the vertical change in that part of the bridge. The following are the main results verified by the performance tests: (1) the horizontal stiffness and damping capacity of LRB depended on the vertical load, but were within the design limit regardless of the small vertical load; (2) there were no significant changes in horizontal stiffness or damping capacity, regardless of the direction of vibration; and (3) the friction coefficient of SRB was approximately 0.1.

Fig.3 LRB-SRB Isolation System

2.2 Connected Girder Structure

The girder connecting sections were designed to satisfy the following conditions: (1) the rotation of the joint section due to live load deflection would not be restricted; and (2) inertia force in the longitudinal direction would be transmitted through the joints. Accordingly, new slab-rubber-hinge designs as shown in **Fig. 4** were adopted. In this method, a rubber functioning like a hinge was placed on the slab and the upper parts of the cross beams were connected by PC wires.
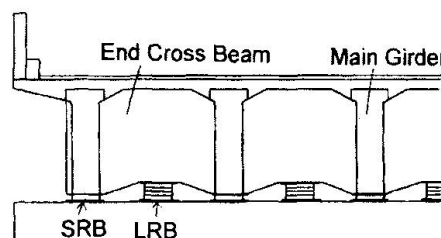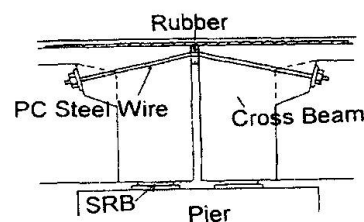

Fig.4 Girder Connection

2.3 Restrainers

A restrainer which could work in directions both longitudinal and lateral was required for an omnidirectional isolation system. Rubber-sheathed chains as shown in **Fig. 5** were adopted. Their impact-absorbing properties can also minimize the probability of destruction due to impact. An impact-tension test was conducted to check the impact-absorbing capability with a high-speed tension tester.
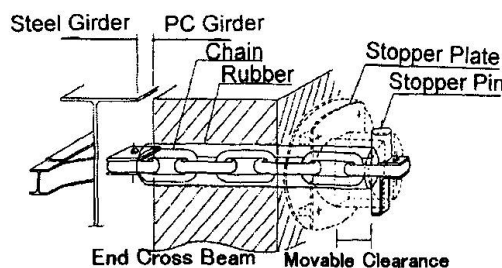

Fig.5 Restrainer with Rubber-sheathed Chain